# EXPERIMENTAL INVESTIGATION AND FEM MODELING OF THE MECHANICAL BEHAVIOR OF METALLIC CELLULAR STRUCTURES PRODUCED VIA WLAM

**IGOR GAVIANO TAVARES**

**DISSERTAÇÃO DE MESTRADO EM ENGENHARIA MECÂNICA**
**DEPARTAMENTO DE ENGENHARIA MECÂNICA**

**FACULDADE DE TECNOLOGIA**

**UNIVERSIDADE DE BRASÍLIA**

**UNIVERSIDADE DE BRASÍLIA**
**FACULDADE DE TECNOLOGIA**
**DEPARTAMENTO DE ENGENHARIA MECÂNICA**

# EXPERIMENTAL INVESTIGATION AND FEM MODELING OF THE MECHANICAL BEHAVIOR OF METALLIC CELLULAR STRUCTURES PRODUCED VIA WLAM

**IGOR GAVIANO TAVARES**

**Orientador: PROF. DR. LUCIVAL MALCHER, ENM/UNB**

**DISSERTAÇÃO DE MESTRADO EM ENGENHARIA MECÂNICA**

**PUBLICAÇÃO PCMEC.DM - XXX/AAAA**
**BRASÍLIA-DF, 15 DE DEZEMBRO DE 2025.**

**UNIVERSIDADE DE BRASÍLIA**
**FACULDADE DE TECNOLOGIA**
**DEPARTAMENTO DE ENGENHARIA MECÂNICA**

# EXPERIMENTAL INVESTIGATION AND FEM MODELING OF THE MECHANICAL BEHAVIOR OF METALLIC CELLULAR STRUCTURES PRODUCED VIA WLAM

**IGOR GAVIANO TAVARES**

DISSERTAÇÃO DE MESTRADO SUBMETIDO AO DEPARTAMENTO DE ENGENHARIA MECÂNICA DA FACULDADE DE TECNOLOGIA DA UNIVERSIDADE DE BRASÍLIA, COMO PARTE DOS REQUISITOS NECESSÁRIOS PARA A OBTENÇÃO DO GRAU DE MESTRE.

APROVADA POR:

Prof. Dr. Lucival Malcher, ENM/UnB
Orientador

Prof.ª Dr.ª Déborah de Oliveira, ENM/UnB
Examinador interno

Prof. Dr. Omid Emadinia, INEGI/PT
Examinador externo

**BRASÍLIA, 15 DE DEZEMBRO DE 2025.**

**FICHA CATALOGRÁFICA**
IGOR GAVIANO TAVARES
**EXPERIMENTAL INVESTIGATION AND FEM MODELING OF THE MECHANICAL BEHAVIOR OF METALIC CELLULAR STRUCTURES PRODUCED VIA WLAM**
**2025xv, 92p., 201x297 mm**
(ENM/FT/UnB, Mestre, Engenharia Mecânica, 2025)
Dissertação de Mestrado - Universidade de Brasília
Faculdade de Tecnologia - Departamento de Engenharia Mecânica

## REFERÊNCIA BIBLIOGRÁFICA

IGOR GAVIANO TAVARES (2025) EXPERIMENTAL INVESTIGATION AND FEM MODELING OF THE MECHANICAL BEHAVIOR OF METALIC CELLULAR STRUCTURES PRODUCED VIA WLAM. Dissertação de Mestrado em Engenharia Mecânica, Publicação xxx/AAAA, Departamento de Engenharia Mecânica, Universidade de Brasília, Brasília, DF, 92p.

## CESSÃO DE DIREITOS

AUTOR: IGOR GAVIANO TAVARES
TÍTULO: EXPERIMENTAL INVESTIGATION AND FEM MODELING OF THE MECHANICAL BEHAVIOR OF METALIC CELLULAR STRUCTURES PRODUCED VIA WLAM.
GRAU: Mestre ANO: 2025

IGOR GAVIANO TAVARES
igor.gavi.t@gmail.com

*“Poetry is sane because it floats easily in an infinite sea; reason seeks to cross the infinite sea, and so make it finite. The result is mental exhaustion [...] The poet only desires exaltation and expansion, a world to stretch himself in. The poet only asks to get his head into the heavens. It is the logician who seeks to get the heavens into his head. And it is his head that splits.”*

G. K. Chesterton

# Agradecimentos

*Faz-se necessário agradecer a DEUS e à intercessão da Bem-Aventurada e Sempre VIRGEM MARIA pelo auxílio em graças, sem as quais se tornaria impossível o transcorrer de um único instante no tempo. Agradeço a Santo Tomás de Aquino, o santo padroeiro dos meus estudos e que mais de uma vez ajudou a iluminar a minha inteligência com aquela mesma Luz que o concedeu tamanho conhecimento.*

*Ademais, faz-se necessário agradecer à minha bela família: primeiramente à minha esposa Maria, que nunca deixou de me apoiar mesmo nos momentos em que eu não merecia – e que foi especialmente generosa em emprestar seu marido para o laboroso empreendimento de redigir uma dissertação de mestrado; ao meu muito amado filho, Afonso Maria, por alegrar minhas pausas de estudo com seus sorrisos, além de me conceder a maior gratificação da minha vida e fruto da minha identidade: ser pai; à minha mãe – Rosana –, pai – Marcos – e irmãos – Gabriella, Ana Cecília e Miguel –, que sempre me amaram e apoiaram.*

*Agradeço ao meu orientador, Prof. Dr. Lucival Malcher pela paciência costumeira com um aluno teimoso e ao INEGI pelo apoio em fornecer os dados experimentais para o estudo, particularmente aos caros Luís Regueiras e Omid Emadinia, que executaram os procedimentos experimentais como parte do PRR New Space program–Portugal (PR192303).*

*Agradeço à empresa em que trabalho, SimScale, pela oportunidade que me deu de trabalhar com algo que amo – e ao lado um time de pessoas igualmente apaixonadas por simulação de engenharia. Por fim, presto gratidão à Universidade de Brasília e ao PCMEC, ambos geradores e fomentadores de meu conhecimento científico. Que DEUS lhes pague.*

# ABSTRACT

Cellular Structures (CS) have been gaining traction both in industry and literature because of their novel approach to part design, where the focus shifts from base material properties and turns towards unit cell geometry. Within this broader CS spectrum stand Lattice Structures (LS): non-stochastic components made of repeatable unit-cells placed on a grid designed using common CS principles to achieve optimal structural properties (especially a high strength-to-weight ratio). In that context, this dissertation provides an experimental investigation of the mechanical behavior, as well as a FEM modeling approach of ER70S-6 Wire Laser Additive Manufacturing (WLAM) manufactured Lattice Structures (LS) under compression, using six different unit cell patterns: Circle, Diamond, Hexagon, Square, Triangle and Wavy. To achieve the study's goal, an initial calibration tensile test using was performed, where optimal Kleinnerman-Ponthot parameters were calculated for the material and a multilinear elastoplastic curve was obtained. Three specimens were then fabricated for each pattern using the WLAM process, and each was submitted to a compression test up to 25mm, while the mean force–displacement results per pattern were computed. The material properties obtained from the tensile test were then added to a 3D Nonlinear Static, elastoplastic simulation where each LS was submitted to a compression test up to 17mm displacement, while retrieving the force–displacement from a control point. A total and specific energy absorption evaluation was made by integrating the force–displacement curves, making it possible to perform a comparative performance analysis of the specimens, as well as of the Simulation–Experiment (S–E) matching. Finally, a qualitative comparison of the S–E deformation modes and mechanisms was also possible by comparing the in-test deformed shapes with the simulated ones. A good agreement between S–E was achieved for the Circle, Diamond, Hexagon and Wavy patterns, with the force–displacement curves showing similar trends, energy values staying below 8% error and deformation mechanisms being accurately represented, especially at the local level. For the Square and Triangle lattices, the S–E discrepancy was greater, but the overall trends were still captured, with the differences possibly attributable to model idealizations and the non-capturing of the global buckling tendency of the specimens by the simulation. Consistency was found in the performance ranking for both simulations and experiments within the truncated domain (13.25 mm). For the simulated data, the Square topology led the group, outperforming the baseline pattern (Circle) by 57.3% in Specific Energy Absorption (SEA), followed by the Triangle with an 18.3% increase. While the Hexagon showed a modest gain of 9.0%, the Diamond and Wavy topologies underperformed the baseline by 2.9% and 11.8%, respectively.

**Keywords:** Cellular Structures, Wire Laser Additive Manufacturing (WLAM), Finite Element Method (FEM), Force–Displacement Curve, Energy Absorption, Volume Fraction.

# RESUMO

**Título em português:** Investigação experimental e modelagem MEF do comportamento mecânico de estruturas celulares produzidas por WLAM

As Estruturas Celulares (EC) vêm ganhando destaque tanto na indústria quanto na literatura devido à sua abordagem inovadora de projeto, em que o foco deixa de ser apenas as propriedades do material base e passa a se concentrar na geometria das células unitárias. Dentro desse amplo espectro das CS encontram-se as Lattice Structures (LS): componentes não estocásticos formados por células unitárias repetidas em uma malha, concebidos de acordo com princípios comuns das EC para alcançar propriedades estruturais otimizadas (especialmente uma alta relação resistência-peso). Nesse contexto, esta dissertação apresenta uma investigação experimental do comportamento mecânico, bem como uma modelagem via FEM, de LS fabricadas por Wire Laser Additive Manufacturing (WLAM) em aço ER70S-6 sob compressão, utilizando seis diferentes padrões de células unitárias: Circle, Diamond, Hexagon, Square, Triangle e Wavy. Para atingir o objetivo do estudo,um ensaio de tração de calibração foi realizado usando um corpo de prova de ER70S-6, a partir do qual foram calculados parâmetros ótimos de Kleinnerman-Ponthot e obtida uma curva elastoplástica multilinear. Em seguida, três amostras de cada padrão foram fabricadas pelo processo WLAM e submetidas a ensaios de compressão até 25 mm, sendo então calculadas as curvas médias forçadeslocamento de cada geometria. As propriedades de material obtidas no ensaio de tração foram incorporadas a uma simulação 3D Não Linear Estática, elastoplástica, na qual cada LS foi submetida a um carregamento de compressão até 17 mm de deslocamento, registrando-se a curva força–deslocamento por um ponto de controle. Uma avaliação da energia total e específica absorvida foi realizada por meio da integração das curvas forçadeslocamento, permitindo uma análise comparativa do desempenho dos espécimes, bem como da concordância entre Simulação e Experimento (S–E). Por fim, também foi possível uma comparação qualitativa dos modos e mecanismos de deformação S–E, confrontando as formas deformadas observadas nos ensaios com aquelas previstas numericamente. Obteve-se uma boa correspondência S–E para os padrões Circle, Diamond, Hexagon e Wavy, cujas curvas forçadeslocamento apresentaram tendências similares, valores de energia com erro inferior a 8% e mecanismos de deformação representados com precisão, sobretudo em nível local. Para as geometrias Square e Triangle, a discrepância S–E foi maior, embora as tendências gerais ainda tenham sido capturadas – diferenças possivelmente atribuídas a idealizações do modelo e à incapacidade da simulação de reproduzir adequadamente a tendência de flambagem global observada nos ensaios. Observou-se consistência na classificação de desempenho, tanto nas simulações quanto nos experimentos, considerando-se o domínio truncado (13,25 mm). Tratando dos dados simulados, o padrão Square liderou o grupo, superando o padrão de referência (Circle) em 57,3% na Absorção Específica de Energia (SEA), seguido pelo Triangle com um aumento de 18,3%. Enquanto o Hexagon apresentou um ganho modesto de 9,0%, os padrões Diamond e Wavy ficaram abaixo da referência em 2,9% e 11,8%, respetivamente.

**Palavras-chave:** Estruturas Celulares, Wire Laser Additive Manufacturing (WLAM), Método dos Elementos Finitos (FEM), Curva Força–Deslocamento, Absorção de Energia, Fração Volumétrica.

# SUMMARY

# LIST OF FIGURES

# LIST OF TABLES

# LIST OF SYMBOLS

## Latin Symbols

| | | |
|---|---|---|
| L | Specimen length | [mm] |
| W | Specimen width | [mm] |
| $t$ | Specimen thickness | [mm] |
| $d$ | Displacement | [mm] |
| $u$ | Vertical displacement at the control point (numerical model) | [mm] |
| F | Force | [N] |
| $\mathrm{V}_{\mathrm{block}}$ | Bounding block volume | [$\mathrm{m}^3$] |
| V | Solid material volume | [$\mathrm{m}^3$] |
| E | Young's modulus (elastic modulus) | [GPa] |
| $\mathrm{E}_s$ | Young's modulus of the solid base material | [GPa] |
| M | Maxwell stability index | [-] |
| $b$ | Number of struts in a lattice unit cell | [-] |
| $j$ | Number of frictionless joints in a lattice unit cell | [-] |
| C | Gibson–Ashby coefficient | [-] |
| $n$ | Gibson–Ashby exponent | [-] |
| P | Generic parameter | [-] |
| $\mathrm{P}_{\mathrm{ref}}$ | Reference value of a generic parameter | [-] |
| PEEQ | Equivalent plastic strain | [-] |

## Greek Symbols

| | | |
|---|---|---|
| $\sigma$ | Stress | [MPa] |
| $\sigma_y$ | Yield stress | [MPa] |
| $\sigma_{y0}$ | Initial yield limit | [MPa] |
| $\sigma_\infty$ | Maximum stress | [MPa] |
| $\varepsilon$ | Strain | [-] |
| $\bar{\varepsilon}^p$ | Equivalent plastic strain | [-] |
| $\rho$ | Equivalent density of the lattice structure | [kg/m$^3$] |
| $\rho_s$ | Density of the solid base material | [kg/m$^3$] |
| $\nu$ | Poisson's ratio | [-] |
| $\xi$ | Isotropic hardening modulus | [MPa] |
| $\delta$ | Hardening exponent | [-] |

## Subscripts

| | |
|---|---|
| $(\star)_s$ | Quantity related to the solid base material |
| $(\star)_y$ | Quantity evaluated at yield |
| $(\star)_{\mathrm{exp}}$ | Experimental quantity |
| $(\star)_{\mathrm{sim}}$ | Simulated (FEM) quantity |
| $(\star)_{\mathrm{ref}}$ | Reference value |
| $(\star)_{\mathrm{block}}$ | Quantity associated with the bounding block |

# Acronyms

| | |
|---|---|
| AM | Additive Manufacturing |
| ASTM | American Society for Testing and Materials |
| BCC | Body-Centered Cubic |
| CAD | Computer-Aided Design |
| CFE | Crushing Force Efficiency |
| CS | Cellular Structure |
| DED | Directed Energy Deposition |
| EA | Energy Absorption |
| FCC | Face-Centered Cubic |
| FDM | Fused Deposition Modeling |
| FEA | Finite Element Analysis |
| FEM | Finite Element Method |
| IPF | Initial Peak Force |
| L-DED | Laser Directed Energy Deposition |
| L-PBF | Laser Powder Bed Fusion |
| LP | Laser Power |
| LS | Lattice Structure |
| PBF | Powder Bed Fusion |
| S–E | Simulation–Experimental |
| SEA | Specific Energy Absorption |
| STL | Standard Tessellation Language |
| TPMS | Triply Periodic Minimal Surface |
| TS | Travel Speed |
| WAAM | Wire Arc Additive Manufacturing |
| WFS | Wire Feeding Speed |
| WLAM | Wire Laser Additive Manufacturing |

# Chapter 1

# INTRODUCTION

## 1.1 Motivation & Background

Conventionally, mechanical design of components has been heavily reliant upon the mechanical properties of the baseline material from which they are made, with some degree of topology optimization to achieve improved overall performance. Recently, however, a new class of materials has gained traction – those whose mechanical response depends primarily on topological characteristics rather than the microstructure of the base material (Reda et al., 2018).

The advantage of not relying solely on the base material comes from the ability to adjust geometry to achieve properties that are naturally unattainable through traditional means – which is why these structures are called “meta” materials. The word “meta” comes from the Greek word and means “beyond” or “after” (as in Aristotle’s *meta*–physics), and metamaterials are materials whose properties can go beyond natural materials. Common examples are achieving a negative Poisson’s ratio (commonly known as auxetic metamaterials) or negative thermal expansion (contraction upon heating), characteristics impossible to find in conventional materials.

The key concept behind metamaterial design is to think in terms of the building blocks that define engineering structures. In most components, material properties are governed by atomic-scale interactions within a crystalline lattice, whereas in metamaterials, the essential “building block” is a repetitive unit cell with a specific topology. These cells are arranged in a grid-like pattern to form the final structure. Such configurations are referred to as cellular structures, defined by Bedoya et al. (2025) as “periodic or aperiodic arrangements of interconnected elements – such as struts, walls, or surfaces – designed to achieve tailored mechanical or functional properties.”

The first disruptive work to demonstrate a cellular structure with unconventional mechanical behavior was that of Lakes (1987), who presented a foam with auxetic properties – expanding laterally when stretched and contracting when compressed. The early exploration of foam-based cellular materials marked the beginning of the metamaterial era, highlighting their lightweight nature and energy-absorbing capability (Figure 1.1). As noted by Gibson (2003), foams are especially valuable in applications such as impact protection – for instance, in helmets or automotive bumpers – due to their ability to maintain nearly constant stress under compression. Gibson (2003) also observed that similar cellular architectures are abundant in nature, including wood, bone, and sponge, reinforcing the idea that such geometries offer efficient structural solutions across different scales. Figure 1.2 presents an example CS found in the *Euplectella aspergillum* sponge (Sharma and Hiremath, 2023).

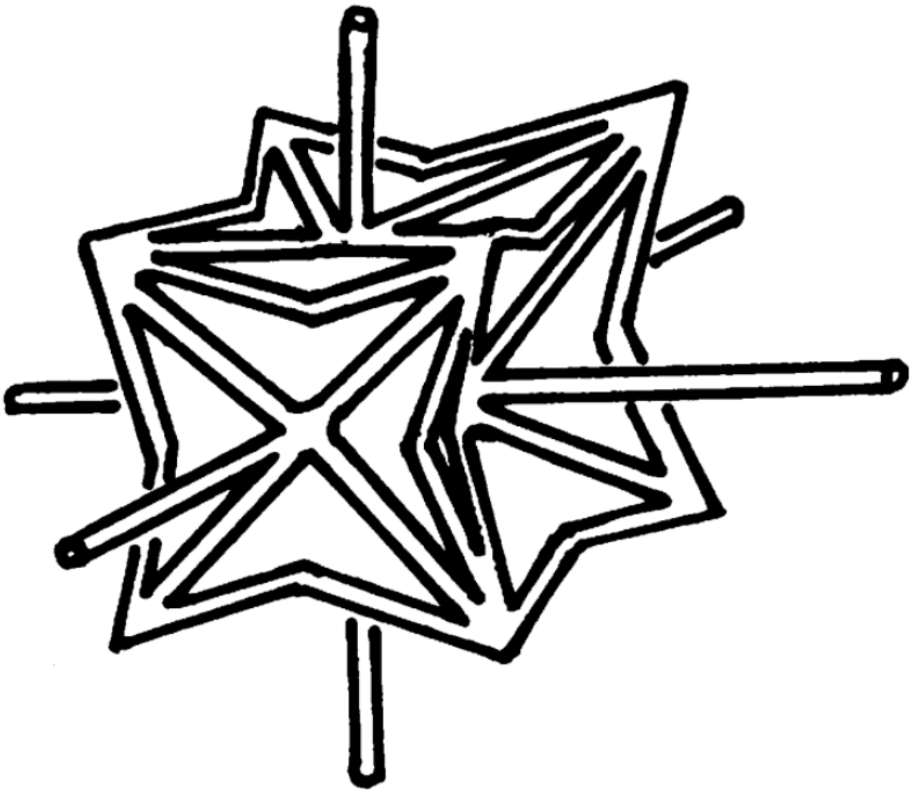

Figure 1.1: Auxetic foam sample presented by Lakes (1987), marking the first experimental observation of a cellular structure exhibiting negative Poissons ratio behavior.

Branching from the initial foam structures – which are particularly useful for energy absorption, filtration, and even heat exchange – two other types of cellular architectures have become highly relevant in structural design: honeycombs and lattices. Although many authors refer to all of them collectively as cellular structures, given their shared principle of achieving mechanical performance through geometry rather than material composition, important distinctions exist. In contrast to the stochastic nature of foams, honeycombs and lattices exhibit highly regular and periodic patterns, allowing for greater predictability and tunability of mechanical behavior (Pan et al., 2020).

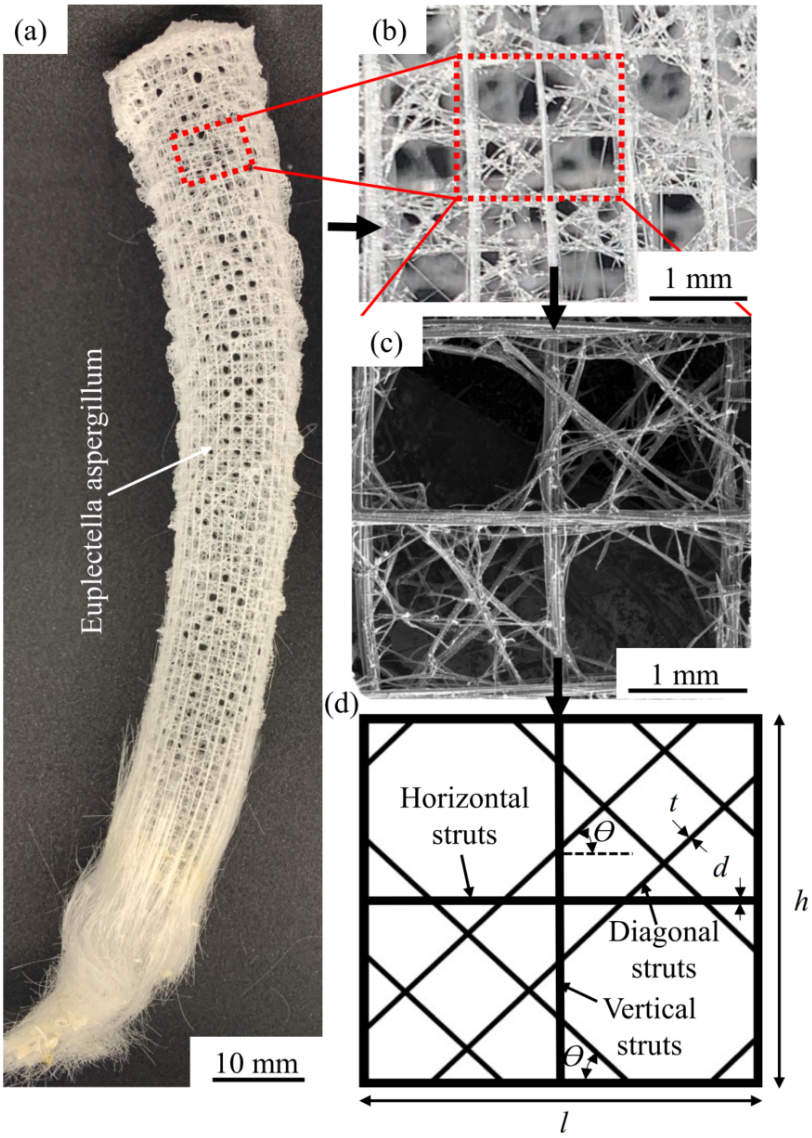

Figure 1.2: Structural hierarchy of the glass sponge *Euplectella aspergillum*, illustrating its naturally occurring lattice-like organization from the macroscale body (a) to the microscale strut network (b–d). Adapted from Sharma and Hiremath (2023).

Building on this distinction, Bhate (2019) emphasized the usefulness of differentiating between lattice patterns and the honeycomb architecture. The honeycomb can be viewed as a two-dimensional structure – typically formed by extruding a regular pattern into a prismatic shape – and can often be manufactured using conventional methods. The emergence of Additive Manufacturing (AM), however, expanded design possibilities far beyond those achievable by traditional techniques. This advancement made it feasible to realize complex three-dimensional lattice geometries composed of interconnected struts or rods, similar to truss systems. These lattices combine low weight with high stiffness and strength, offering an exceptionally favorable strength-to-weight ratio (Pan et al., 2020).

Tao and Leu (2016) proposed a general classification of cellular materials into stochastic (open- and closed-cell foams) and non-stochastic structures. Within the non-stochastic category, they introduced the terms “2D lattice” – corresponding to what Bhate (2019) referred to as “honeycomb” – and “3D lattice,” which aligns with Bhate’s definition of “lattice.” The terminology established by Tao and Leu (2016) will be adopted throughout this dissertation. For strictly structural applications – where stiffness, stability, and load-bearing capacity are critical – non-stochastic designs are favored due to their consistent and reproducible mechanical response under loading. As a result, lattice structures have been widely implemented in biomedical, aerospace, and automotive applications, where achieving high mechanical performance with minimal weight is of primary importance.

Practical examples of these applications illustrate the diversity of lattice metamaterials. Sychov et al. (2018) demonstrated the use of triply periodic minimal surface (TPMS) lattices for shock-absorbing panels in orbital stations, reporting a 23% increase in tensile strength compared to conventional honeycomb cores. In biomedical engineering, Zhang et al. (2018) employed Ti-6Al-4V lattice implants, including ankle and vertebral fusion devices, fabricated via additive manufacturing (Figure 1.3). The patients in these case studies achieved successful recoveries, although the authors noted that further optimization is needed to balance strength and ductility. These examples underscore how geometry, rather than base material, governs mechanical performance in architected materials.

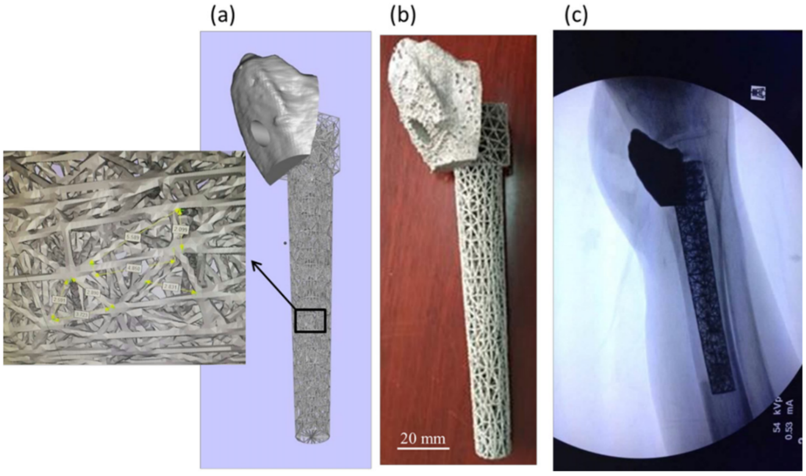

Figure 1.3: Additively manufactured Ti6Al4V lattice implant used for bone reconstruction, showing (a) the CAD model, (b) the printed component, and (c) its *in vivo* radiographic placement. Adapted from Zhang et al. (2018).

The evolution of lattice design is inseparable from the progress of additive manufacturing. Technologies such as Powder Bed Fusion (PBF) and Directed Energy Deposition (DED) have revolutionized the production of complex metallic geometries, allowing engineers to fabricate designs that were previously unachievable through conventional means. Their layer-by-layer approach eliminates geometric constraints, enabling precise control over internal architecture and material distribution. As highlighted by Ghidini et al. (2023), the space industry has been an early adopter of AM, driven primarily by the pursuit of mass reduction and improved stiffness-to-mass ratios, which also lead to significant cost and time savings. Moreover, lattice-based metamaterials produced via AM have shown enhanced impact resistance and thermal management capabilities, confirming that their unique properties arise from structural geometry rather than material composition itself, as “they gain their functional properties from their structure rather than inheriting them directly from the material they are composed of.” (Ghidini et al., 2023)

In summary, in several notable engineering applications, the focus of mechanical design has been gradually shifting from optimizing intrinsic material properties to engineering the internal geometry of components. This transition reflects a move from an atomistic to a cellular design approach, where structural behavior is governed by topology rather than composition. At the core of such cellular architectures are metallic lattice structures, which enable mechanical characteristics otherwise unattainable in conventional materials – such as auxetic behavior – while also achieving significant reductions in material usage and weight. These advantages are most effectively realized through additive manufacturing (AM) technologies, particularly Laser Directed Energy Deposition (L-DED) and more specifically it’s wire feedstock branch, Wire Laser Additive Manufacturing (WLAM), which allow the fabrication of highly complex lattice geometries with precise control over structure and density.

In the context of these advancements, the ability to predict and optimize the mechanical performance of lattice components has become increasingly important. Accurately estimating their stiffness and deformation response under applied loading remains challenging due to the complex interaction between geometry and material behavior. In this regard, the Finite Element Method (FEM) serves as a robust and versatile tool for analyzing and guiding the design of such architected materials, providing a framework for performance prediction, optimization, and further development of the field.

## 1.2 Problem Statement

In spite of the potential Wire Laser Additive Manufacturing (WLAM) presents in terms of industrial applications for fabricating metallic lattice structures, little to no research has been performed on the bottlenecks of the specific process. While there has been a wide focus in the similar Wire and Arc Additive Manufacturing (WAAM) process – a Directed Energy Deposition (DED) method that uses wire as feedstock material and an electric arc as the power source – Gomez-Lendinez et al. (2025) identifies a research gap in the direction of investigating the material properties of components produced by WLAM, especially when it comes to low-carbon steels.

If that is the case for material properties more generally, a similar pattern is observed when narrowing down to the specific topic of Lattice Structures (LS). While many studies were found where the authors studied the mechanical response of lattice structures, including FEM modeling (Sun et al., 2022; Zhang et al., 2022; Leary et al., 2018), they are solely focused on parts fabricated using the Powder Bed Fusion (PBF) process (even if using different power sources), which is fundamentally different from DED. DED made parts suffer a higher thermic load because of the amount of power used in the process, which can be significantly higher than the one used in the PBF process (DebRoy et al., 2018). This is related to the higher energy requirement for creating the melt pool for DED applications, non-existent in the PBF process.

Given the lack of experimentally validated numerical studies of mechanical components within this context, it is the goal of this dissertation to create a framework for accurately predicting the force-displacement response of metallic Lattice Structures (LS) under compression, manufactured via the L-DED process and the WLAM method. This will be achieved by modeling the problem using the Finite Element Method (FEM): first by calibrating the model with experimental data from a simple tensile test, then by simulating the elastoplastic response of the actual LS under compression and comparing against test data. The following section covers the objectives of the study.

## 1.3 Objectives

Building on the problems outlined in the previous sections, this section presents the general and specific objectives of the dissertation. They are designed to help overcome some of the challenges currently associated with the current state of the art research on predicting the mechanical behavior of WLAM manufactured components by using the FEM.

### 1.3.1 General Objective

The general objective of this dissertation is to develop and validate a FEM model that accurately predicts the mechanical response of Lattice Structures (LS) manufactured by WLAM  bridging the gap between numerical prediction models and experimental data in the field. Additionally, this study aims to understand the force–displacement behavior of LS under compression, and to evaluate how their geometric shape is affected by compressive loading.

The specific objectives are outlined next.

### 1.3.2 Specific Objectives

The specific objectives of this dissertation are as follows: to characterize the mechanical behavior of the base material; then, generate a multilinear elastoplastic stress–strain curve through a curve-fitting algorithm and apply it in Abaqus to simulate the same tensile test using the finite element method (FEM); to calibrate the material model by comparing numerical and experimental force–displacement results. With the calibrated curve, numerical simulations are performed for various lattice structure (LS) configurations featuring distinct geometric patterns, namely Circle, Diamond, Hexagon, Square, Triangle, and Wavy. The simulated force–displacement responses are then compared with the corresponding experimental results from the compression tests. Additionally, the energy absorption (EA) and specific energy absorption (SEA) values are computed for both experimental and simulated cases and analyzed comparatively across all LS geometries. The deformation shapes observed in the simulations are also compared to the experimentally compressed specimens to assess geometric accuracy. Finally, the predictive performance of the FEM model is evaluated, its limitations identified, and recommendations proposed for further refinement.

## 1.4 Outline of the Dissertation

**Chapter 1 – Introduction:** Presents the motivation and background of the study, defines the research problem, and outlines the general and specific objectives. It also establishes the scientific context for studying WLAM-manufactured lattice structures and the need for validated numerical models.

**Chapter 2 – Literature Overview:** Reviews the state of the art on lattice metamaterials, their mechanical behavior under compression, additive manufacturing of metallic lattices via Directed Energy Deposition (with emphasis on WLAM), and the main modeling strategies used in FEM analyses of lattice structures.

**Chapter 3 – Methodology:** Describes the overall methodological framework, including the calibration of the material model from tensile tests, the numerical setup for the FEM simulations, and the procedures for validating the model using experimental compression data for the six lattice geometries.

**Chapter 4 – Results and Discussion:** Presents and interprets the experimental and numerical results, compares force–displacement curves, energy absorption metrics, and deformation modes, and discusses the agreements and discrepancies observed between simulations and experiments.

**Chapter 5 – Conclusion:** Summarizes the main findings, discusses the limitations of the study an provides suggestions for future research developments.

# Chapter 2

# LITERATURE OVERVIEW

Following the problem and objectives covered in the previous section, the goal of this chapter is to present the state of the art concerning the research topics by reviewing the most recent and relevant literature. The review is divided into three main subsections, namely: Lattice metamaterials, focusing on their classification and properties and mechanical response under compression; Additive Manufacturing of steel lattices via DED, providing a detailed description of the DED process and its characteristics with emphasis on WLAM and the process effects on mechanical properties; Review of FEM simulations of lattices, focusing on how numerical results match against experimental data and common methods for problem modeling. The examination of these topics is essential to the research at hand, as it establishes a strong scientific foundation to develop the FEA framework for simulating LS.

## 2.1 Lattice Metamaterials

Lattice structures (LS) are the foundation of this dissertation work and, as covered in Section 1.1, they represent a special kind of metamaterial composed of a non-stochastic structure made of a repeatable pattern. There are many possible configurations for LS, and their mechanical response under compression varies depending on the specific geometry. The goal of this section is to summarize the different arrangement possibilities and examine how the mechanical response changes depending on the design approach.

### 2.1.1 Classification and Properties

As mentioned extensively in the previous sections, LS are a special kind of cellular structure that consists of a repeatable pattern put together in a lattice-like fashion. As highlighted by Nazir et al. (2019), the key benefit of such structures is their high strength-to-weight ratio, as well as their good energy absorption – while at the same time minimizing the amount of utilized material. These structures are already tailored by nature and show how a cellular approach can be advantageous over an atomistic one. Bones, for instance, can have strength comparable to cast iron while at the same time being as light as a block of wood of similar volume.

Although some authors identify LS with a stochastic – or pseudo-stochastic nature – (Pan et al., 2020), for the purpose of the present dissertation LS will refer only to non-stochastic cellular structures. Original studies in cellular structures – e.g. Lakes (1987) foundational study – focused on foams, which are characterized by their stochastic composition. However, there has been a paradigm shift and turn towards organized patterns ever since Additive Manufacturing (AM) was inserted in the industrial environment. AM allows for more control over cell size, thickness and part connectivity, as well as the possibility of reliably reproducing complex shapes and placing them on a repeatable structure (Bhate, 2019).

LS can be further divided in terms of the unit-cell geometry, which can be either tridimensional – where the cells are repeated in a 3D grid – or two-dimensional – where the cells are repeated in a 2D grid, then extruded in the thickness direction. Some authors – e.g. Bhate (2019) – have called the 3D kind simply “Lattices” and the 2D kind “Honeycombs”, but this terminology can be confusing since “Honeycomb” can also refer to a specific geometric configuration (hexagon pattern). Tao and Leu (2016) prefer to distinguish between the two kinds by calling them 3D and 2D Lattices, respectively (Figure 2.1).

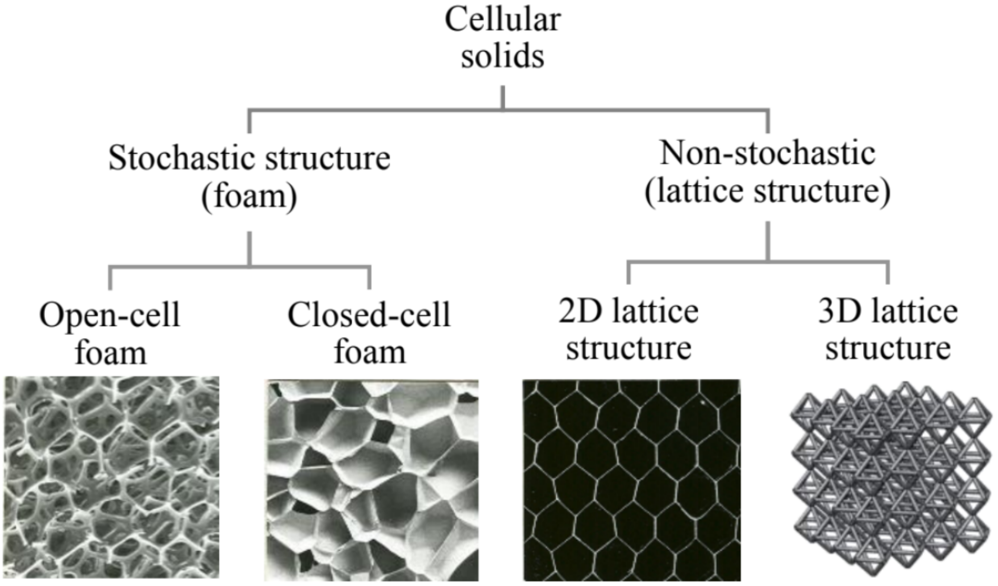

Figure 2.1: Classification of cellular solids according to structural order, showing the distinction between stochastic foams (open- and closed-cell) and non-stochastic lattice structures (2D and 3D). Adapted from Tao and Leu (2016).

3D Lattices have undoubtedly been the most thoroughly studied, perhaps because of the flexibility in changing their mechanical behavior. They can also be used in a wider range of applications in comparison to both foams and 2D Lattices (Pan et al., 2020). 3D Lattices are typically composed of interconnected surfaces or links – also called “struts” – which can be repeated in all spatial directions. The design of unit cell geometry is usually the focus of designing such Lattices and there is a broad range of options, with the most common being Body-Centered Cubic (BCC) and Face-Centered Cubic (FCC) – or variations of these – named after the analogous crystalline structures (Maconachie et al., 2019). Other common unit-cell configurations are Cubic, Octet-truss and Diamond (Figure 2.2).

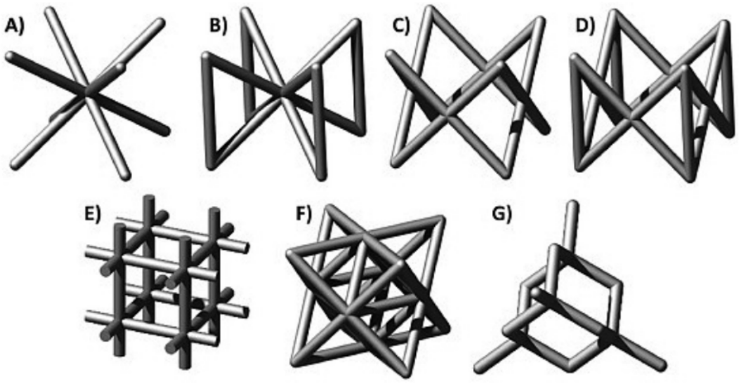

Figure 2.2: Common strut-based lattice unit cells, including (A) BCC, (B) BCCZ, (C) FCC, (D) FCCZ, (E) Cubic, (F) Octet-truss, and (G) Diamond configurations. Adapted from Maconachie et al. (2019). (2019).

These truss-like 3D Lattices dominate the literature because of their ease of parametrization, since researchers can simply change parameters like cell size and strut diameter to perform optimization studies. Maskery et al. (2016), for instance, developed a 6x6x6 array of BCC cells with 3mm edge length, then compared two possible configurations: one where density was uniform across the grid, and one where it varied vertically (by increasing the strut diameter in the downwards direction), and showed that a preferential load path appeared in the diagonal direction – a shear band – for the uniform density LS. The shear band behavior was not present at the graded density configuration, where the structure collapsed layer by layer. Similarly, Al-Saedi et al. (2018) investigated how density impacts the mechanical response of a 3D Lattice made of F2BCC cells – which consist of a combination of 2 FCC cells and a BCC one in a single unit – and achieved comparable results, also identifying that the shear bending disappeared.

Another increasingly popular branch of 3D Lattices is what is referred to as Triply Periodic Minimal Surfaces (TPMS), which consists of non-conventional geometric surfaces – e.g. Gyroid, Schwartz Diamond, Neovious, D-prime (Figure 2.3) – generated by equations that try to minimize the area (Sychov et al., 2018). Sychov et al. (2018) compare their tensile strength with the same parameter for 2D Lattices and conclude that “for cellular elements with $\rho_1 = 0.38$ g/cm$^3$ comparable to the density of the primary D-surface, the value of the specific tensile strength is 23% less than the value of the same parameter of TPMS”. Wang et al. (2020) studied a different kind of LS, “Lattice Cylindrical Shell”, by comparing conventional topological approaches – such as Honeycomb and Triangular shaped cells – with a Gyroid pattern, and found that the latter presented “considerably superior load capacity and energy absorption under compression.” (Figure on multiple kinds of TPMS)

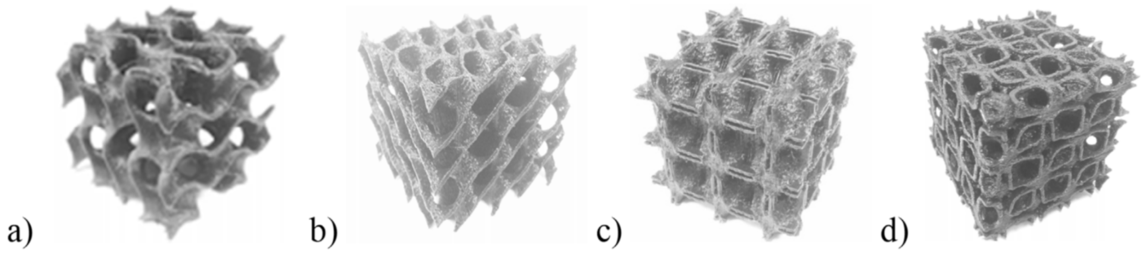

Figure 2.3: Additively manufactured samples of triply periodic minimal surface (TPMS) lattices: (a) Gyroid, (b) Schwartz Diamond, (c) Neovius surface, and (d) D-prime surface. Adapted from Sychov et al. (2018).

Beyond theoretical appeal, 3D Lattices have also gained popularity because of the ease of manufacturing by employing PBF processes. PBF can achieve a high part accuracy and does not require support material – since the support function is performed by the powder bed. Engineering design can then flourish since there are few limitations when it comes to part geometry, which allows for the manufacturing of LS such as TPMS and highly customized 3D Lattices (by, for instance, varying strut thickness accurately to achieve a graded density structure). Chen et al. (2021) stated it clearly: “PBF technologies have great advantages in fabricating lattice structures with significantly complex geometries”.

However, even if 3D Lattices dominate current research, 2D Lattices are foundational to the study of LS and represent an equally significant branch of cellular structure architecture. They are both easier to manufacture using conventional methods and found in nature, they have been explored for centuries and more widely so from the beginning of the 20th Century (Qi et al., 2021) – and gained popularity in the last two decades because of the advancements in measurement techniques, which facilitated the study of their mechanical properties.

2D Lattices are designed by distributing the repeatable pattern across a bi-dimensional grid instead of a tri-dimensional one, then extruding the obtained structure across a specific thickness. This is the reason why they are also commonly called “Honeycombs” (Qi et al., 2021), i.e., they resemble the way a natural beehive is built (Figure 2.4). Qi et al. (2021) also highlight that these structures present many of the advantages of 3D Lattices: “Owing to their excellent performances in such properties as fracture toughness, impact resistance, heat dissipation, vibration and noise reduction [...] honeycomb materials have been well developed and extensively used in a broad range of applications covering architecture, automotive, railway vehicle, marine, aerospace, satellites, packaging, electronic communications, electrochemistry, nanofabrication, and medical implants.”

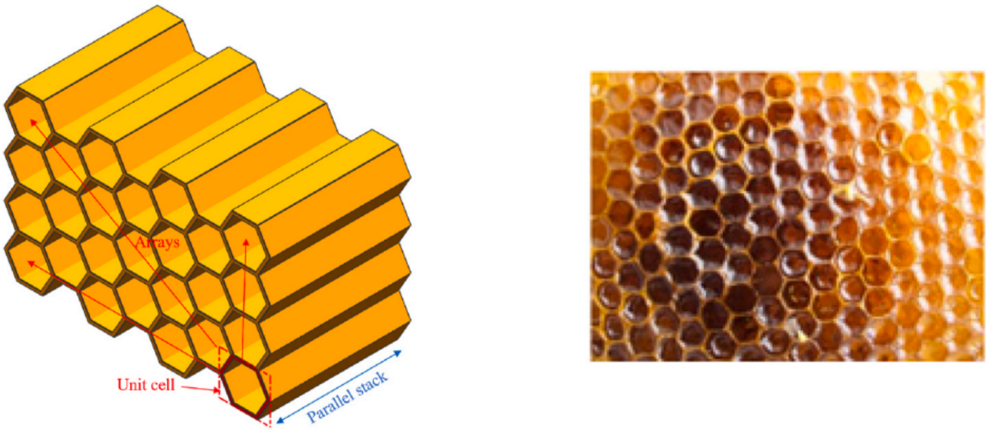

(a) (b)

Figure 2.4: Basic concept of a 2D LS with hexagonal configuration (a) and its natural counterpart observed in a beehive (b). Adapted from Qi et al. (2021).

Therefore, the appeal of 2D Lattices lies in their simplicity, predictability and manufacturability while maintaining the advantages in terms of mechanical properties that LS provide. As previously stated, 3D Lattices often require high accuracy, support-free methods to manufacture due to their highly intricate nature, whereas 2D Lattices can be more easily reproduced since they consist of patterns in a plane.

At the same time, 2D Lattices also benefit from the advantages of AM, which has sparked a new interest in their research in recent years. As an example, Qi et al. (2021) mentions a more intricate kind of 2D Lattices (also inspired by natural systems), where a repeatable pattern is added to individual unit cells – making them “hierarchical” of either a self-similar (smaller patterns have the same shape as the larger ones) or non-self-similar (smaller patterns have a different shape from the larger ones). They provide an improvement in mechanical properties in comparison to conventional 2D Lattice configurations and were also inspired by hierarchical structures in nature. Furthermore, non-conventional configurations can also be explored with the aid of AM.

The most common way of categorizing 2D Lattices, however, is by the design principle behind their unit cells. Yin et al. (2023) provide comprehensive summaries of possible unit cell kinds commonly used in 2D lattices, by dividing them into three main categories: general, auxetic and hierarchical. The general kind comprises non-auxetic, non-hierarchical cells, and they are the most common kind. Mohammadi et al. (2023) note that the original inspiration for 2D lattices were honeycombs (Hexagon pattern), but researchers have built on top of them to come up with different patterns, most commonly Square, Circle and Triangle, which Qi et al. (2021) call “classical”, since they “have been comprehensively studied because of their ultra-light and high stiffness/strength characteristics” (Figure 2.5).

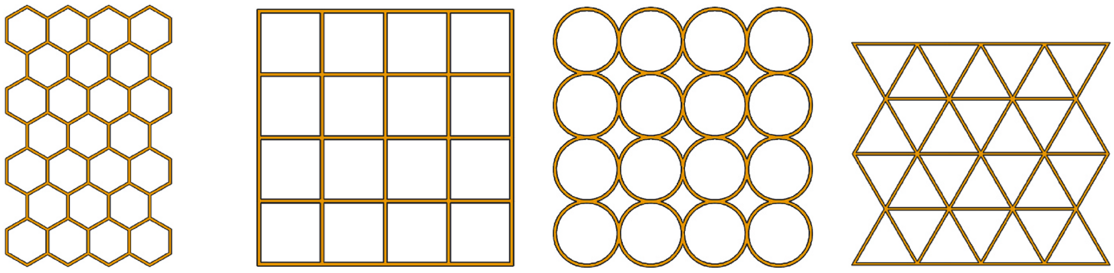

(**a**) Hexagonal (**b**) Square (**c**) Circular (**d**) Triangular

Figure 2.5: Classical 2D lattice patterns used in non-auxetic, non-hierarchical designs: (a) Hexagonal (honeycomb), (b) Square, (c) Circular, and (d) Triangular unit-cell arrays. Adapted from Qi et al. (2021)

Slight variations of the four “canonical” patterns can also be obtained – e.g. by rotating the Square in 45° gives a rhombic pattern – and lowering the top and bottom angles forms a diamond-shaped unit-cell. Zeng et al. (2021) also provide an interesting way of obtaining different patterns, by parametrizing an angle $\phi$ on a Square unit cell. The topology is certainly one of the key factors that impact mechanical behavior, but parametrization can be performed within the same structure by varying cell side length (l) and strut thickness (t), as Figure 2.6 illustrates.

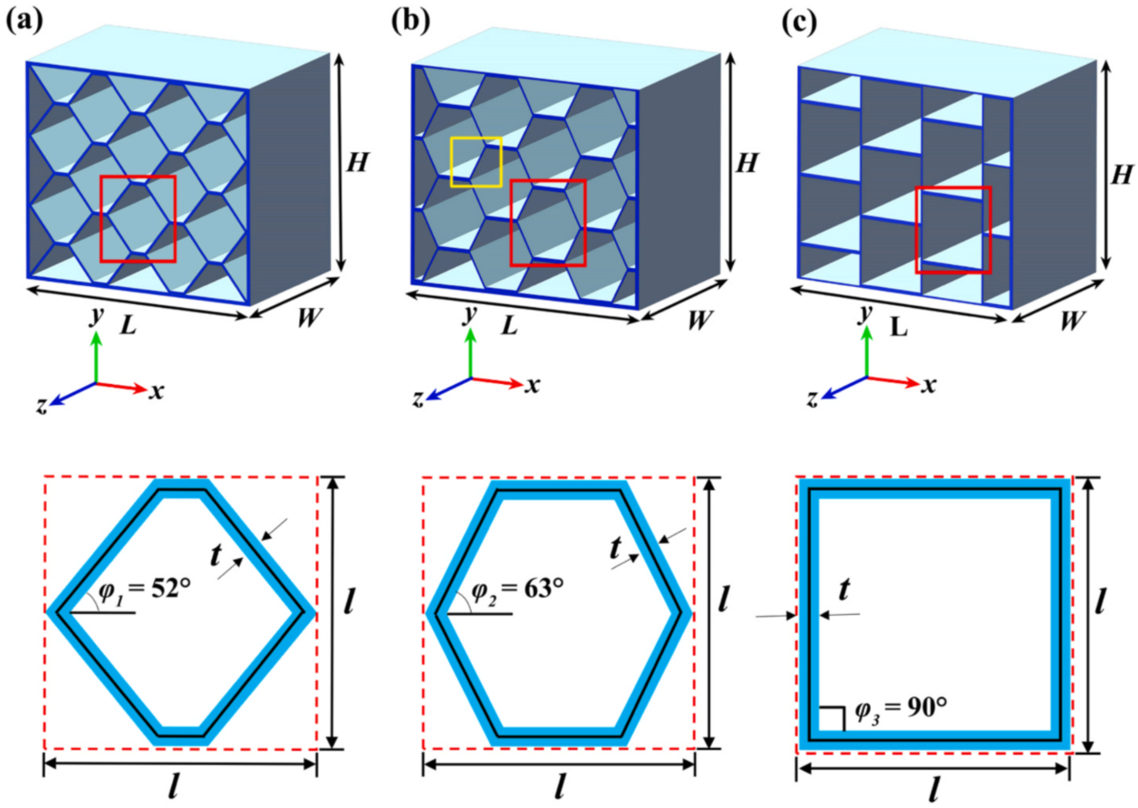

Figure 2.6: Honeycomb structures with variable strut thickness ($t$) and inclination angle ($\varphi$), showing (a) $\varphi_1 = 52°$, (b) $\varphi_2 = 63°$, and (c) $\varphi_3 = 90°$. Adapted from Zeng et al. (2021).

### 2.1.2 Mechanical Response Under Compression

Under compressive loading, LS present a well-known three-stage behavior: elastic deformation, plateau stress, and densification – as Li et al. (2023) put it “A typical energy absorbing cellular structure experiences the elastic stage, plateau stress region, and densification stage under compressive loading.” In the elastic phase, deformation is bending-dominated and reversible; the plateau-stress portion presents a constant stress while cells collapse; and the densification region is marked by a rapid stress increase as the cells come in contact with one another and “densify” the structure. Zeng et al. (2021) documented corresponding force–displacement curves for composite honeycomb panels, clearly distinguishing these regimes and noting that they also apply to the force–displacement case (as opposed to only applying in the stress–strain scenario). Figure 2.7 shows a typical stress–strain curve for a LS.

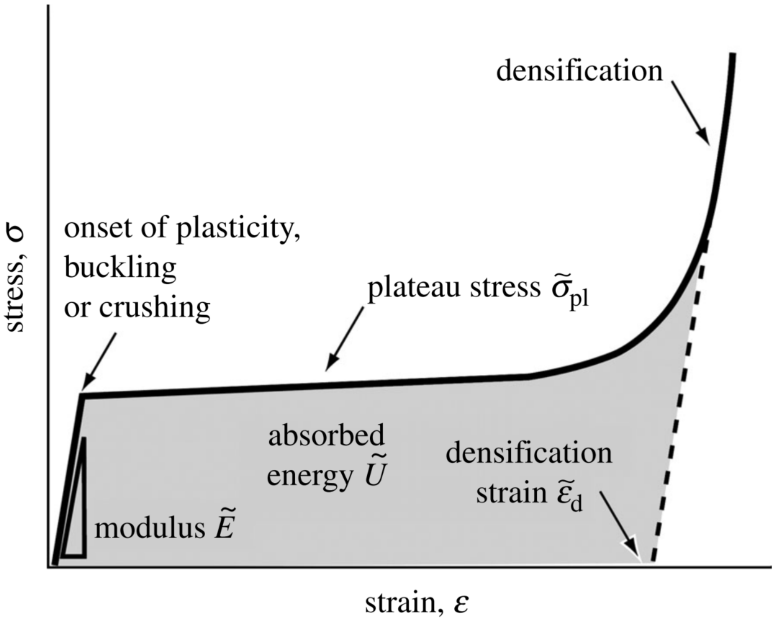

Figure 2.7: Typical stressstrain response of a cellular material under compression. Adapted from Ashby (2006).

Although the general outline of the mechanical response is similar across most kinds of LS, there is a binary variation depending on whether the structure is bending-dominated or stretch-dominated. The difference between bending-dominated and stretch-dominated LS comes from their mechanical response under loading, where bending-dominated ones will experience bending of their rods – almost “folding on themselves” – and stretch-dominated ones will make the rods mostly stretch (Ashby, 2006). Although there are differences, for instance, in the material curve that allow researchers to distinguish between one kind and the other, a simple way of telling is thinking in terms of mechanisms and the Maxwell’s stability criterion, which establishes:

$$\mathrm{M} = \mathrm{b} - 2\mathrm{j} + 3 \quad \text{(2D)}$$

$$\mathrm{M} = \mathrm{b} - 3\mathrm{j} + 6 \quad \text{(3D)}$$

where b is the number of struts and j is the number of frictionless joints (hence why thinking in terms of mechanisms is relevant). The idea is that if M < 0, the structure becomes unstable and will behave like a mechanism, folding onto itself (which in the case of welded joints, means that the struts will bend). If M > 0, the structure is stable and stiff, which means that the equivalent behavior will be stretch-dominated (see Figure 2.8).

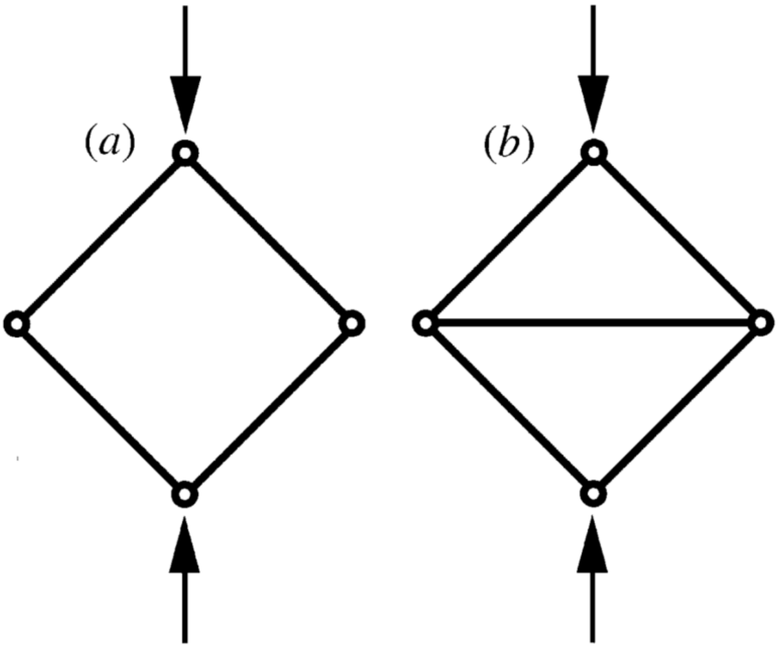

Figure 2.8: Illustration of Maxwells stability criterion using pin-jointed frames: (a) a mechanism that collapses under load (bending-dominated when joints are fixed), and (b) a triangulated structure that resists deformation by axial forces (stretch-dominated). Adapted from Ashby (2006).

Sun et al. (2022) notes that “compressive strength and stiffness are highly dependent on whether the unit cell exhibits stretching-dominated or bending-dominated behavior,” with the former yielding greater stiffness and the latter more stable deformation. Ashby (2006) notes that, while stretch-dominated LS present a higher strength in comparison to the bending ones, they are worse for energy absorption applications. By comparing a generic bending-dominated and a stretch-dominated curve, the main difference comes in the transition from the elastic region to the plateau stress – since the stretch-dominated curve will present an initial softening stage before plateauing and densifying (Figure 2.9).

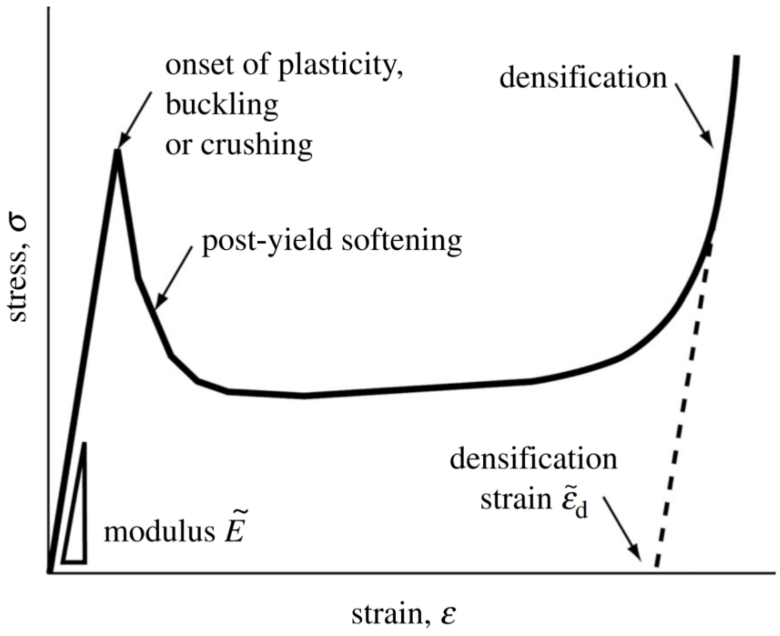

Figure 2.9: Typical stressstrain curve for a stretch-dominated lattice structure, highlighting the post-yield softening. Adapted from Ashby (2006).

In terms of mechanical properties, there is a widely known relationship that describes the connection between the equivalent LS Elastic Modulus and Density and the base material's. The correlation is given by the Gibson–Ashby equations (Ashby, 2006), and they predict that there is a quadratic proportionality between the Elastic Modulus ratio and density ratio for bending-dominated LS and a linear correlation for stretch-dominated LS. Maconachie et al. (2019) note that the relationship can also be formulated more generally as a power-law dependency where the coefficient and exponent can be obtained via experimental results, with the resulting equations being presented below.

$$\frac{\mathrm{E}}{\mathrm{E}_s} = \mathrm{C}\left(\frac{\rho}{\rho_s}\right)^2 \qquad \text{(bending-dominated)} \tag{2.1}$$

$$\frac{\mathrm{E}}{\mathrm{E}_s} = \mathrm{C}\left(\frac{\rho}{\rho_s}\right) \qquad \text{(stretch-dominated)} \tag{2.2}$$

$$\frac{\mathrm{E}}{\mathrm{E}_s} = \mathrm{C}\left(\frac{\rho}{\rho_s}\right)^n \qquad \text{(general formulation)} \tag{2.3}$$

where $\mathrm{E}_s$ is the Elastic Modulus of the base solid material, E is the Elastic Modulus of the LS, $\rho_s$ is the density of the base solid material and $\rho$ is the equivalent density of the LS (considering its porosity). Maconachie et al. (2019) studied multiple possible unit-cell configurations and concluded that "regression analysis of the reported data demonstrated positive power relationships with high correlations could be drawn between the relative density and strength of modulus for most topologies, consistent with the insights of the Gibson–Ashby model."

Ashby (2006) additionally develops equations that pertain to the yield stress relationship between LS and the base material.

$$\frac{\sigma_y}{\sigma_{y,s}} = C\left(\frac{\rho}{\rho_s}\right)^{\frac{3}{2}} \qquad \text{(bending-dominated)} \tag{2.4}$$

$$\frac{\sigma}{\sigma_{y,s}} = C\left(\frac{\rho}{\rho_s}\right) \qquad \text{(stretch-dominated)} \tag{2.5}$$

where $\sigma_{y,s}$ is the yield limit of the base solid material and $\sigma_y$ is the yield limit of the LS, $\rho_s$ is the density of the base solid material and $\rho$ is the equivalent density of the LS. Note, however, that not always the failure will be governed by plasticity in the case of LS, since buckling (in the case of highly flexible or slender struts) or fracture (in the case of brittle materials) can be more critical depending on the case.

Parameters like Specific Energy Absorption (SEA), Initial Peak Force (IPF) and Crushing Force Efficiency (CFE) also vary depending on topological parameters, especially when comparing stretch- and bending-dominated structures. Specific cell units will enhance a particular parameter while lacking elsewhere. Zeng et al. (2021), for instance, investigated the effect of changing cell size length ($l$) and the pattern's inclination angle ($\phi$) on multiple mechanical characteristics of 3D printed honeycombs, and found that both parameters significantly influence the compression behavior and energy absorption capabilities. The comparative analysis presented in Figure 2.10 shows that, as they increased $l$, initial peak force presented a monotonic increase and specific energy absorption showed a monotonic decrease. Increasing the inclination angle demonstrated to increase the energy absorption capacity, whereas a 52° inclination angle exhibited the lowest crushing force efficiency.

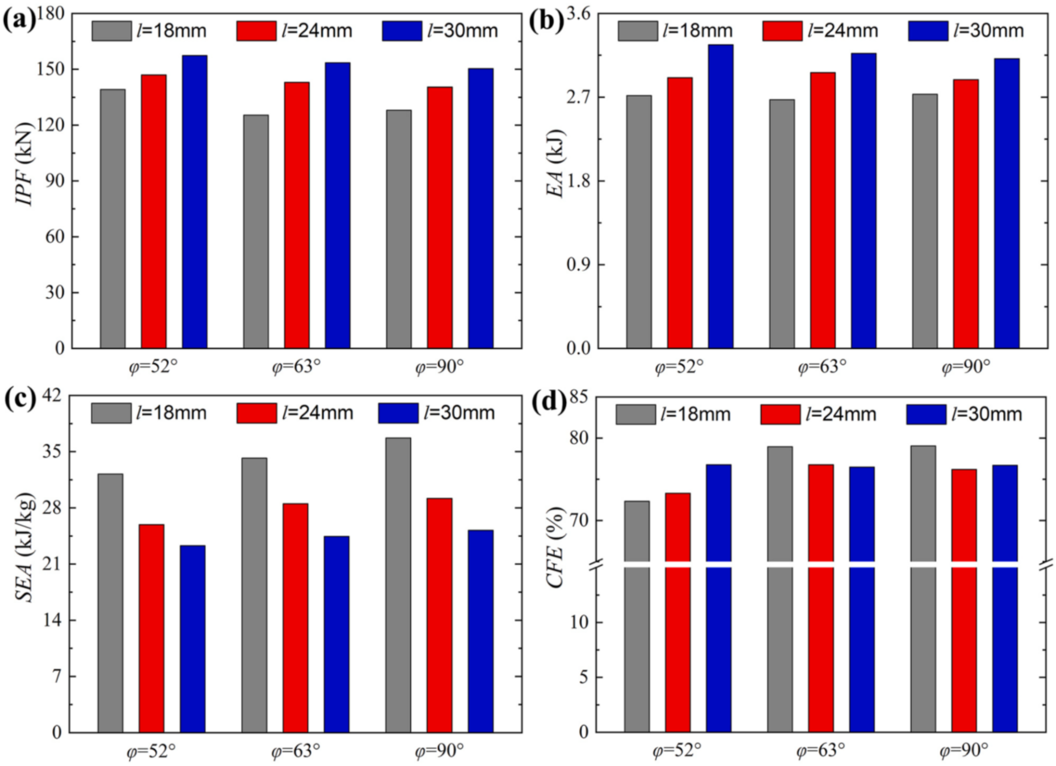

Figure 2.10: Comparison of parameters for 3D-printed 2D Lattices under out-of-plane compression, with variable cell inclination angles (φ = 52°, 63°, 90°) and cell lengths ($l$ = 18, 24, 30 mm): (a) Initial Peak Force (IPF), (b) Total Energy Absorption (EA), (c) Specific Energy Absorption (SEA), and (d) Crushing Force Efficiency (CFE). Adapted from Zeng et al. (2021).

The mechanical response can also be largely influenced by geometric changes, when it comes to deformation modes. Many authors – e.g. Maskery et al. (2016); Zeng et al. (2021); Al-Saedi et al. (2018); Ghaemi Khiavi et al. (2022); Wu et al. (2023); Sharma and Hiremath (2023); Zhou et al. (2023) – report shear bands which lead to failure instead of the more uniform layer-by-layer collapse. Al-Saedi et al. (2018) particularly note that employing a graded density structure, i.e., a structure with a density gradient from top to bottom does away with the shear bands and presents a layer-by-layer collapse (Figure 2.11). Similarly, while studying honeycomb 2D LS, Li et al. (2023) found that the conventional honeycomb structure presented a non-uniform collapse due to buckling and cell rotation. To fix this behavior, they changed the unit cell's side wall angle and noticed that changing the angles by only 15° made the structure collapse layer by layer as expected.

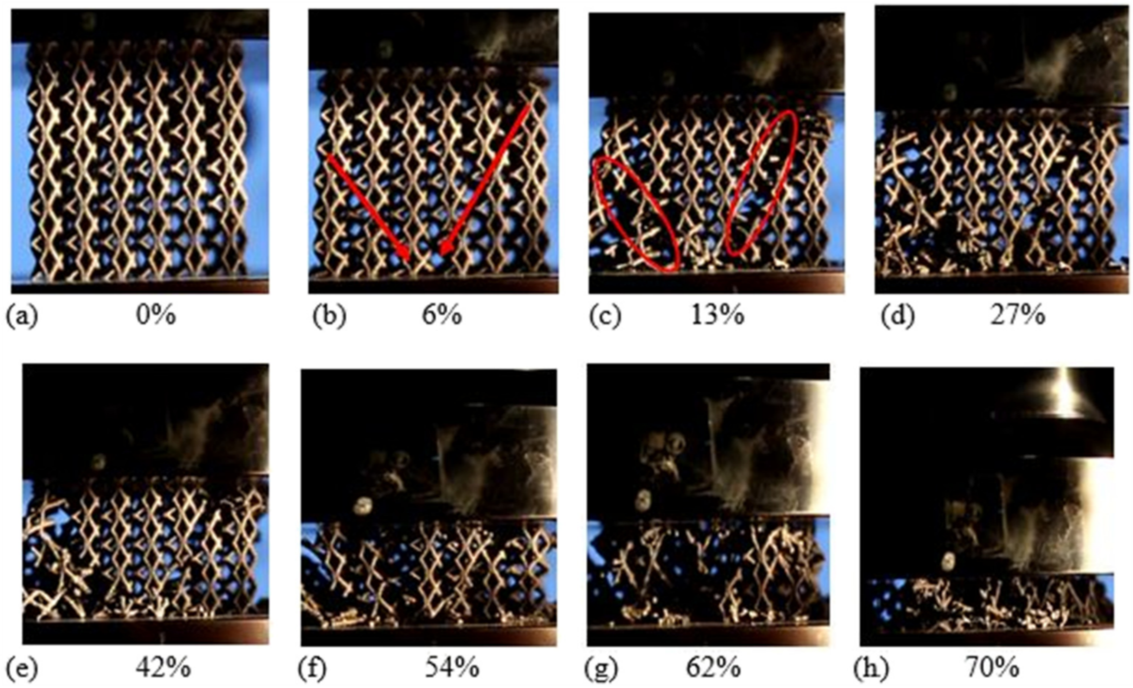

Figure 2.11: Deformation stages of a uniform lattice structure under compression at different strain levels, showing the progressive development of shear bands. Adapted from Al-Saedi et al. (2018).

Besides the deformation modes which eventually lead to failure, one can also speak of deformation "mechanisms" within the context of LS. This is highlighted by the fact that some LS, as previously mentioned, operate in a mechanism-like fashion in the sense that they are meant to deform in a particular way, not to resist loading application. The most common example is the one of auxetic LS – i.e., structures that present a negative Poisson's ratio – where many geometry kinds were proposed to achieve the same goal, each one with its particular deformation mode, as highlighted by Montgomery-Liljeroth et al. (2023) and presented in Figure 2.12.

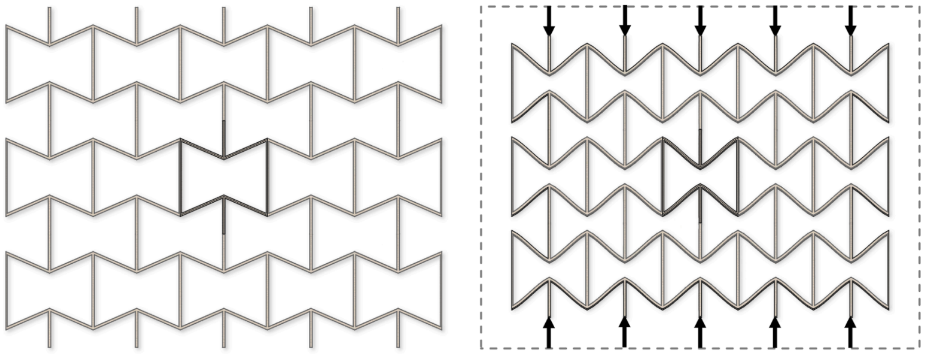

(**a**) Re-entrant hexagonal

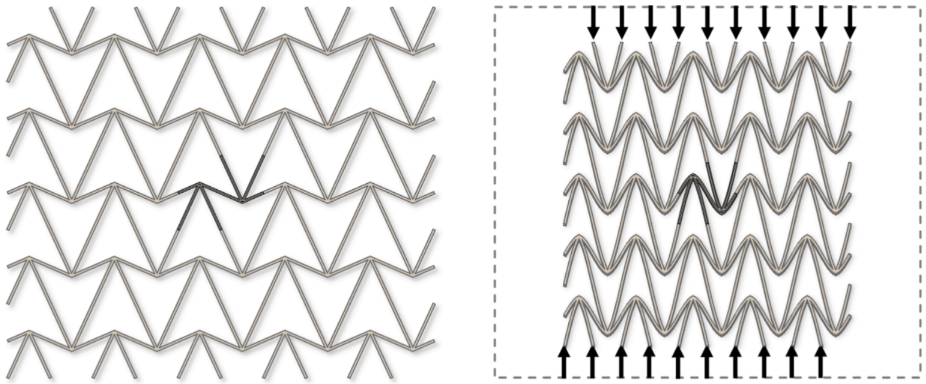

(**b**) Double arrowhead

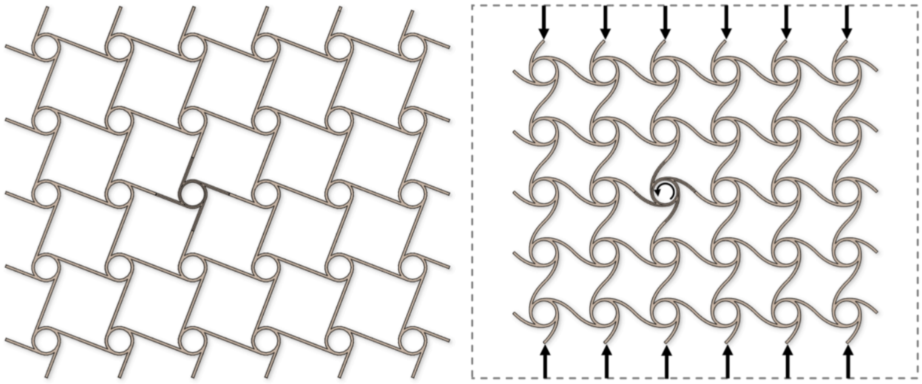

(**c**) Tetrachiral

Figure 2.12: Representative auxetic lattice structures illustrating their deformation mechanisms under compression: (a) re-entrant hexagonal, (b) double arrowhead, and (c) tetrachiral patterns. Adapted from Montgomery-Liljeroth et al. (2023).

Another way in which unit cell design might affect the mechanical response is in terms of structure isotropy/anisotropy. Clarke et al. (2023) studied the anisotropy of different 2D LS patterns – including Hexagon, Square and Triangle – and found that the Square lattice is highly anisotropic, while the hexagon and Triangle honeycombs exhibit near isotropy, especially at higher relative densities (0.35 and 0.45).

Finally, while the geometric configuration dictates the theoretical mechanical performance and deformation modes, the physical realization of these complex designs is fundamentally constrained by manufacturing capabilities. The transition from a digital CAD model to a physical component introduces process-specific variables – such as thermal history, layer adhesion, and surface quality – that directly influence the final properties. Consequently, understanding the specific fabrication method is as crucial as the geometric design itself. In this context, Wire Laser Additive Manufacturing (WLAM) emerges as a pivotal technology for fabricating these metallic structures, as explored in the following section.

## 2.2 Additive Manufacturing of Steel Lattices via DED

According to the ASTM F2792–12a Standard Terminology for Additive Manufacturing Technologies, Additive Manufacturing (AM) is defined as "a process of joining materials to make objects from 3D model data, usually layer upon layer, as opposed to subtractive manufacturing methodologies" (ASTM, 2012). As discussed in section 1.1, AM has become a cornerstone of modern manufacturing because it enables the production of complex geometries with minimal material waste while accommodating a wide range of materials (Pan et al., 2020). It is within this context that lattice structures have emerged as a viable alternative to conventional solid designs – and the AM of metallic components is what will be discussed next.

### 2.2.1 Process Characteristics and Influence on Mechanical Properties

As mentioned in section 2.2, Additive Manufacturing (AM) of metals can be divided into two main processes, according to the ASTM (2012) standard, namely: Powder Bed Fusion (PBF) and Directed Energy Deposition (DED). PBF is defined by the standard as "an additive manufacturing process in which thermal energy selectively fuses regions of a powder bed," i.e., using a powder bed within a sealed chamber and locally either melting or sintering the powder using a power source, building the part layer upon layer.

DED, on the other hand, is defined as "an additive manufacturing process in which focused thermal energy is used to fuse materials by melting as they are being deposited," and works by generating a melt pool using a power source to which a continuous rate of feedstock material is supplied in a non-enclosed environment. Figure 2.13 displays a comparison between the working principles behind the two processes.

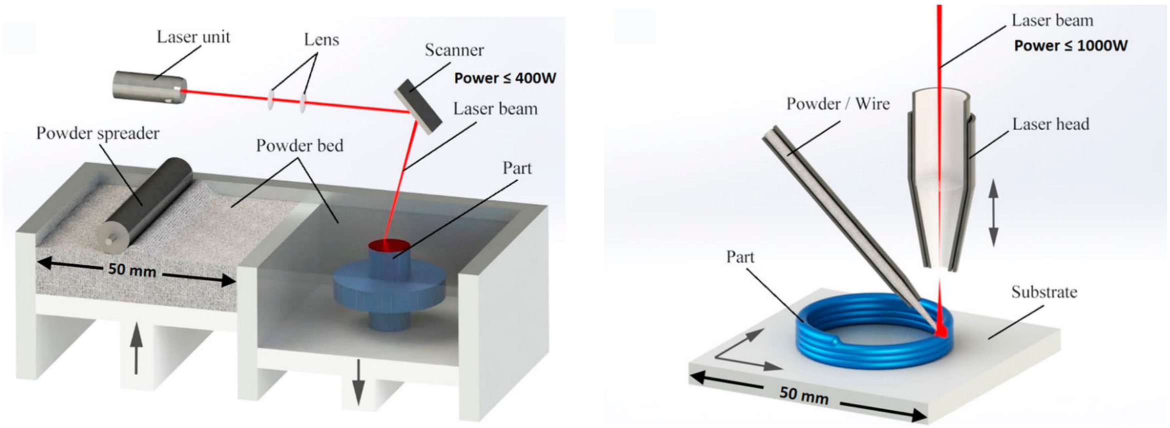

(**a**) Powder Bed Fusion (PBF)

(**b**) Directed Energy Deposition (DED)

Figure 2.13: Comparison between the two main Additive Manufacturing processes for metals: (a) Powder Bed Fusion (PBF), which melts selected regions of a powder bed inside a sealed chamber, and (b) Directed Energy Deposition (DED), which feeds material directly into the melt pool in an open environment. Adapted from Yin et al. (2022).

This basic understanding of the distinction between the two processes provides the basis for choosing between them, since it already highlights some of the advantages and limitations of each. Since PBF requires a sealed chamber, for instance, the part size will be intrinsically limited by the chamber size – whereas DED has no such limitation (Yin et al., 2022). DED will also deploy a higher production rate (Shaikh et al., 2020), but will be lacking in terms of part accuracy (Ghidini et al., 2023). For applications where the structures are massive and there is no need for micron-level accuracy – such as large aerospace parts – DED thrives. To highlight this advantage, Ghidini et al. (2023) report DED being employed to build an entire rocket.

Beyond the operational distinctions, PBF and DED processes can be further divided into different categories based on the power source used, which includes lasers, electron beams, plasma arcs, or gas-metal arcs (DebRoy et al., 2018). One power source which has been gaining traction in recent years, being used both for PBF and for DED, is laser, where L-DED refers to Laser Directed Energy Deposition. Within the L-DED category, either powder or wire can be used as feedstock material, which highlights the versatility of DED.

While PBF generally offers superior results in terms of microstructure and part accuracy, DED's efficiency makes it the ideal solution for large-scale applications. Using wire as feedstock for L-DED results in a process called Wire Laser Additive Manufacturing (WLAM) – also referred to as Wire Laser Metal Deposition (WLMD), Laser Wire-Feed Metal Additive Manufacturing (LWAM), and similar terms. WLAM has been gaining traction in the literature and Abuabiah et al. (2023) reported the growing number of citations concerning the subject matter. It has notable advantages over the powder alternative, since it minimizes the risk of explosions by simplifying industrial operations, makes switching between feedstock materials easier, provides a cleaner work environment, and comes at a lower financial cost, both upfront and for maintenance (Gomez-Lendinez et al., 2025; Ghanadi and Pasebani, 2024). For the manufacturing of metallic cellular structures, WLAM then becomes a strong candidate, especially for industries such as Aerospace which require large components and low material waste. Table 2.1 offers a comprehensive comparison between L-PBF and WLAM.

| **Laser Powder Bed Fusion (L-PBF)** | **Wire Laser Additive Manufacturing (WLAM)** |
|---|---|
| ✓ High dimensional accuracy and excellent surface finish | ✓ No chamber-size limitation; suitable for large-scale components |
| ✓ Superior microstructural uniformity | ✓ Higher production rate compared to PBF |
| ✓ High geometric resolution due to selective fusion of powder regions | ✓ Lower operational and maintenance cost |
| ✓ Suitable for applications requiring micron-level tolerances | ✓ Safer and cleaner industrial environment |
| ✘ Build volume limited by chamber size | ✓ Easier switching between feedstock materials |
| ✘ Lower deposition/production rates | ✓ Compatible with robotic arms for flexible, omnidirectional deposition |
| ✘ Requires sealed and controlled processing environment | ✓ Strong candidate for manufacturing large metallic lattice structures |
| ✘ Higher operational risks and costs associated with metal powders | ✘ Lower dimensional accuracy compared to L-PBF |
|  | ✘ Surface quality and porosity sensitive to wire feeding orientation |
|  | ✘ Requires continuous inert-gas shielding to prevent oxidation |

Table 2.1: Comparison between Laser Powder Bed Fusion (L-PBF) and Wire Laser Additive Manufacturing (WLAM). The advantages and limitations summarized here were organized based on the data and definitions provided by the following sources: ASTM (2012); Yin et al. (2022); Shaikh et al. (2020); Ghidini et al. (2023); DebRoy et al. (2018); Gomez-Lendinez et al. (2025); Ghanadi and Pasebani (2024); Pratheesh Kumar S et al. (2022); Abuabiah et al. (2023).

The WLAM process – in broad terms – consists of melting a wire material using a focused laser and continuously feeding it into a melt pool. A nozzle is responsible for focusing the laser and providing the inert atmosphere (most usually an argon gas flow) to prevent oxidation, and the material is commonly added diagonally (or vice versa). The system originally operated similar to an FDM printer, where the material was added layer upon layer on top of a moving substrate, and planar motion happened in the three cartesian directions (Yin et al., 2022).

Recently, however, manufacturers have gone through another route by employing a robotic arm that usually feeds the material coaxially with the laser focus – which allows for a wider flexibility in terms of deposition patterns since it employs more degrees of freedom. The axial feeding also permits an omnidirectional deposition, since side feeding requires the wire to always be fed at the leading edge of the deposition to achieve optimal surface quality and porosity (Pratheesh Kumar S et al., 2022). Figure 2.14 shows how a robotic arm (Meltio$^{TM}$) builds a component by taking advantage of its multiple degrees of freedom.

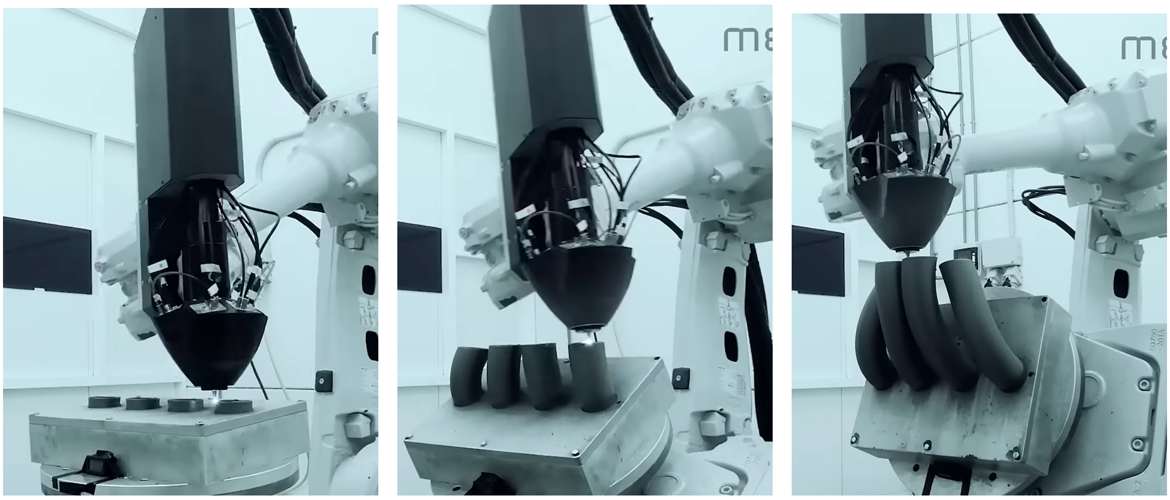

(a) (b) (c)

Figure 2.14: Sequential frames showing a robotic coaxial wire-feeding system (Meltio$^{TM}$) during Directed Energy Deposition (DED). The system employs multiple degrees of freedom, allowing omnidirectional deposition and complex tool paths (Meltio, 2021).

Broadly speaking, there are four main kinds of parameters which can be adjusted in every DED process, related to: energy source, feedstock material, deposition strategy and feeding strategy (Ghanadi and Pasebani, 2024). In the case of WLAM, these translate into the options highlighted in Figure 2.15.

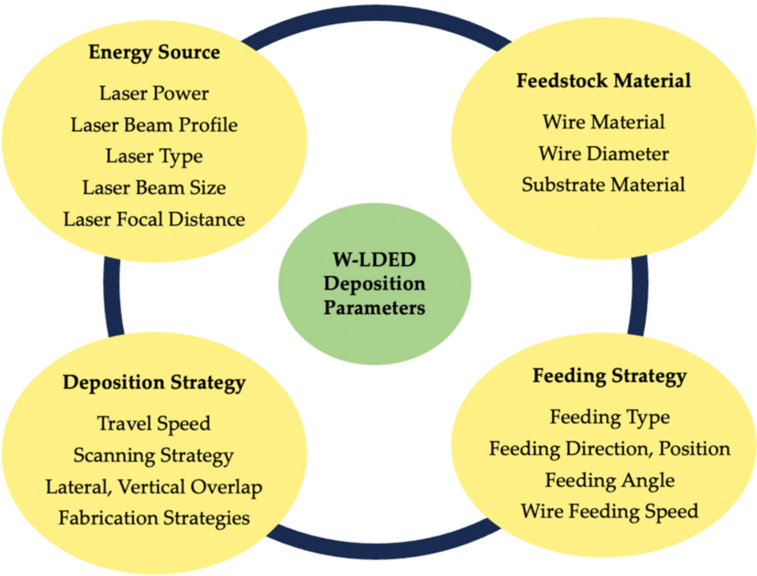

Figure 2.15: Main categories of deposition parameters in Wire Laser Directed Energy Deposition (W-LDED). Adapted from Ghanadi and Pasebani (2024).

Ghanadi and Pasebani (2024)'s monumental review on the subject matter highlights some of the ways each of these parameters influence the characteristics and integrity of the manufactured parts. To name a few examples, the Travel Speed (TS), Wire Feeding Speed (WFS) and Laser Power (LP) will significantly affect the final parts properties since they are directly related to the specific energy per second at the melt pool. The correlation between specific energy and laser power is straightforward, but not as obvious for the other parameters. A higher travel speed, for instance, will allow the same amount of energy to be distributed across a larger region, resulting in a lower specific energy. The same happens by increasing the WFS, since more volume will be added while keeping the same amount of absolute power.

Yin et al. (2022) highlighted how the power affects the melt pool, especially when it comes to its depth. The depth monotonically increases along with the power, and since DED often employs 2–3× the power – or more – used in PBF, the melt pool will stretch across a much higher portion of the geometry. Figure 2.16 shows how the LP affects the melt pool's depth.

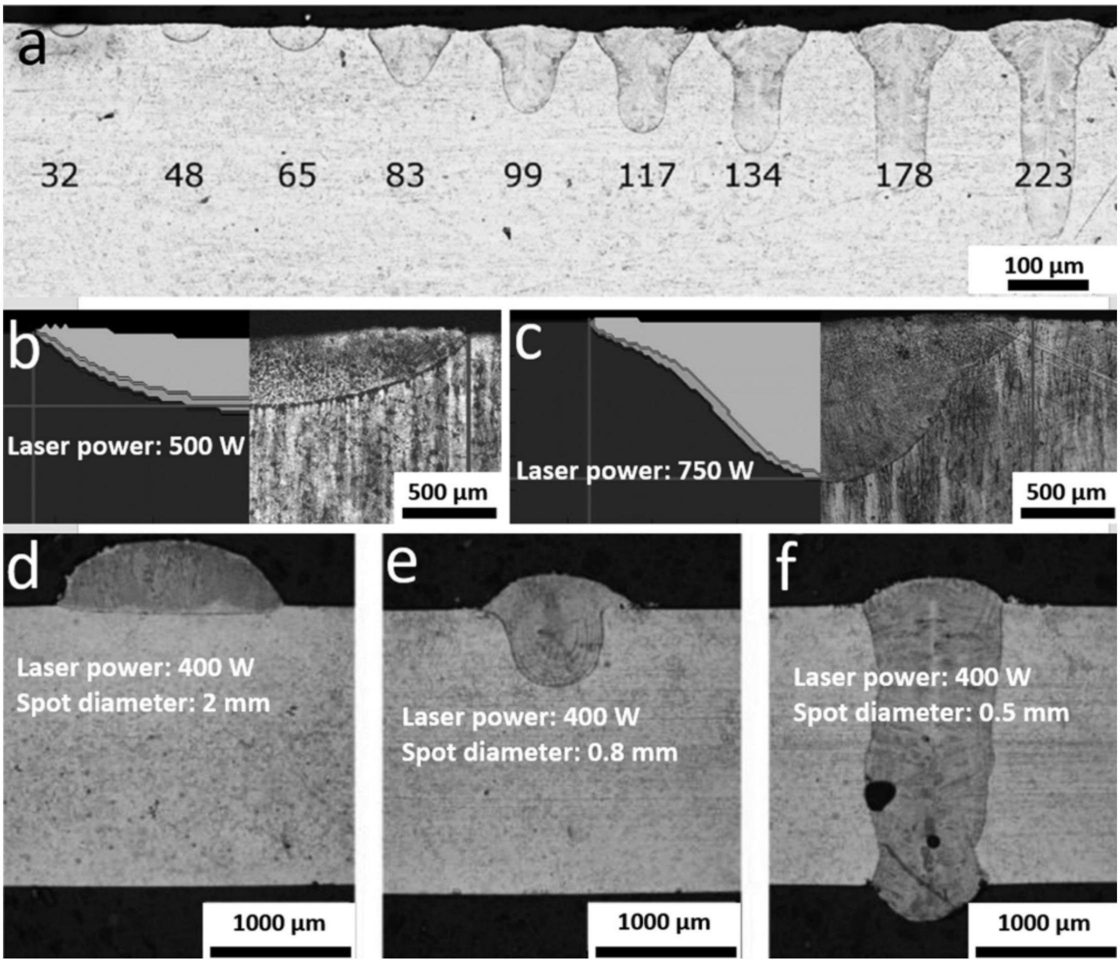

Figure 2.16: Variations of melt pool morphologies for steels produced by different processes and parameters. (a) L-PBF-built samples under increasing laser powers (in W), (bc) L-DED under 500 W and 750 W, and (df) laser welding at constant 400 W with varying spot diameters. Adapted from Yin et al. (2022).

One of the key benefits of WLAM is how easily the process parameters can be changed, resulting in a notable upside in terms of part quality and strength. As an example, by simply changing the laser type from continuous to pulsating, an enhanced cooling performance can be achieved in the process (diminishing thermal gradients in the parts), and varying the laser spot diameter (which changes the specific energy applied at the melt pool) is an easy way of tuning the level of power applied locally to the system and has proven to alter different characteristics ranging from the melt pool shape and temperature to the surface roughness to the overall stability of the process (Ghanadi and Pasebani, 2024; Abuabiah et al., 2023).

Therefore, since DED – and more specifically WLAM – is a high energy process, especially in comparison to PBF, controlling the amount of energy input is crucial for tuning the properties of the melt pool and manufactured part. A more helpful way of expressing this idea is by using the expression “thermal cycle” instead of simply “energy input”, since not only heating but also how cooling happens as the process develops will impact the parts.

Bottom layers, for instance, will show a high temperature at first, but their temperature will progressively decrease as the part is built layer by layer, especially since they are closer to the substrate and lose more heat due to conduction – which means that the cooling at the bottom will be more effective than at the top, producing a thermal gradient. Gomez-Lendinez et al. (2025) present simulation results for the thermal gradients in DED manufactured specimens, as shown in Figure 2.17. At the same time, the lower layers are also “reheated” as the part is being built, in the sense that they are constantly receiving heat from upper layers. Its also worth noting that PBF also generates a thermal gradient in the parts, but to a lesser degree especially due to the lower energy input.

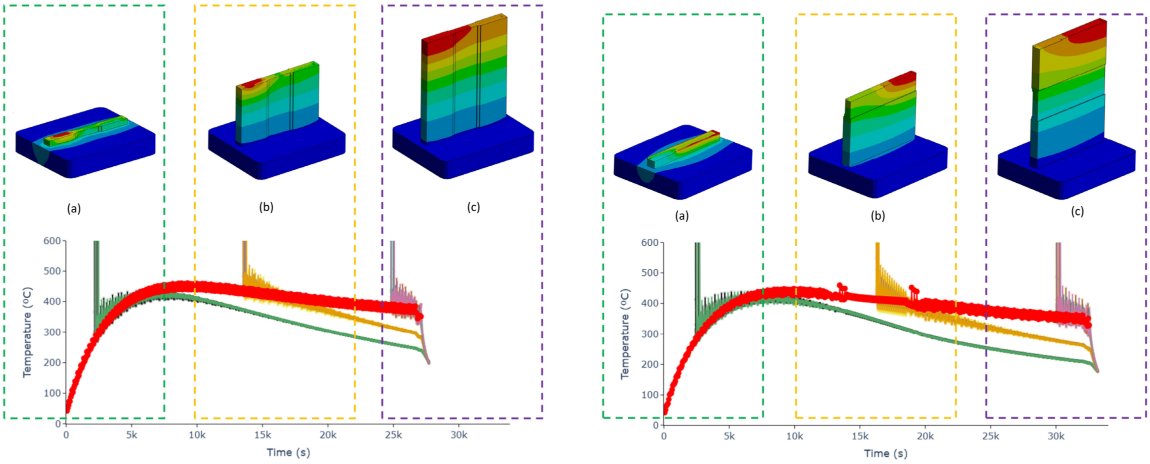

(**a**) XY-oriented specimen (**b**) XZ-oriented specimen

Figure 2.17: Comparison of the simulated thermal histories for specimens printed in the XY and XZ orientations, adapted from Gomez-Lendinez et al. (2025).

While studying AM of steels, Bajaj et al. (2020) noted that this behavior creates a kind of “Intrinsic Heat Treatment” – as opposed to the extrinsic one commonly performed in parts manufactured through conventional processes – in the sense that lower layers will receive different heat inputs as well as experience different cooling rates, affecting their microstructure and mechanical properties. For stainless steels produced by DED, for instance, it has been observed that the yield and tensile strengths are higher at the bottom layers in comparison to the top layers (Bajaj et al., 2020). Gomez-Lendinez et al. (2025) reported similar results for ER70S-6 steel fabricated parts, where the bottom ones presented consistently higher values for yield and tensile strengths.

On the other hand, if the energy input is lowered – which can be done if using a fine wire as feedstock – in a process termed Fine Wire Laser Metal Deposition (FW-LMD) – the part quality increases. Shaikh et al. (2020), by using a 100 µm wire and pulsed laser beams, demonstrated that a right tuning of WLAM parameters can lead to a surface finish and layer height comparable to PBF processes (Figure 2.18). The tensile strength of the FW-LMD fabricated specimens also showed a value on the higher end of the spectrum for bulk specimens of the same material.

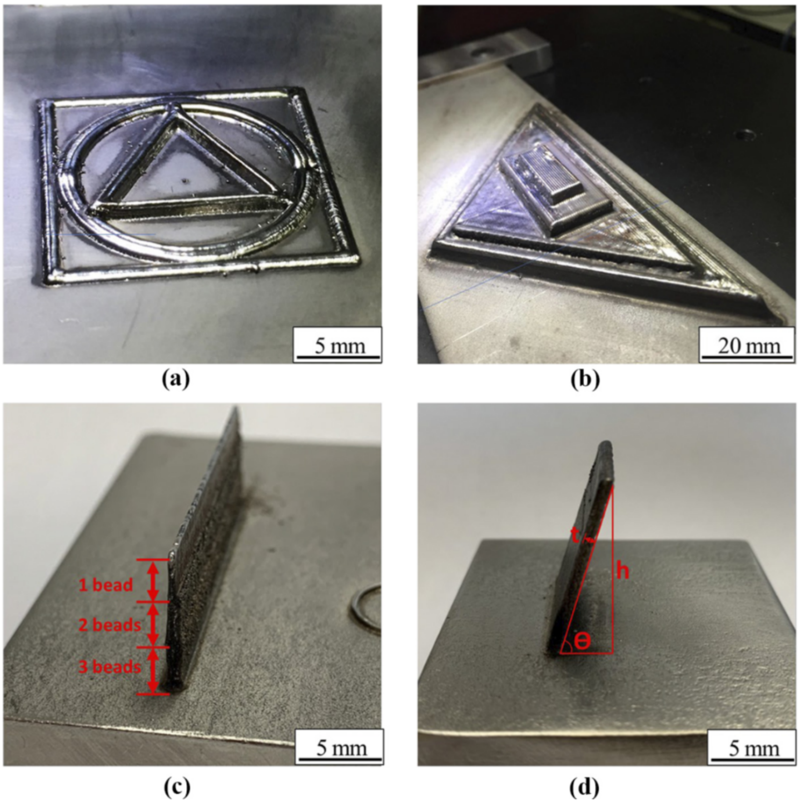

(a) (b)

(c) (d)

Figure 2.18: Examples of complex geometries fabricated using Fine Wire Laser Metal Deposition (FW-LMD), demonstrating the high precision and surface quality. Adapted from Shaikh et al. (2020).

The print direction also impacts the resistance of WLAM-fabricated parts, and stack direction plays a crucial role in determining the mechanical strength of the final components. In ER70S-6 steel, Gomez-Lendinez et al. (2025) reported a strong directional dependence of tensile properties: horizontally built specimens (XY) all exhibit yield strengths above 400 MPa – with the bottom sample reaching 472 MPa – whereas vertically oriented (XZ) samples average around 355 MPa and are all below 400 MPa. The superior strength of horizontal builds can be attributed to the more uniform cooling across the plane, which leads to a more homogeneous microstructure. The specimen's XY–XZ orientations are presented in Figure 2.17.

Another factor which plays a role in determining the base mechanical properties of WLAM-manufactured parts is – naturally – the wire material. Although there are not many studies specifically focusing on the low-carbon ER70S-6 wire, it is commonly employed because of its good processability and wide application in welding (Gomez-Lendinez et al., 2025), and the similarity between laser welding and WLAM is clear from the way the process takes place, i.e., primarily by generating a melt pool (Yin et al., 2022) to which the material is fed.

Given the complex interplay between the WLAM process parameters, part geometry and the resulting material properties – relying solely on experimental data for design optimization becomes very expensive and time-consuming. This complexity makes it relevant to develop predictive tools capable of modeling both the geometry and the material behavior under load. The Finite Element Method (FEM) serves as this essential bridge, offering a framework to predict mechanical response without extensive physical testing. The next section reviews the state-of-the-art in numerical simulation of lattice structures, highlighting strategies to address these modeling challenges.

## 2.3 Review of Finite Element Simulation of Lattices

### 2.3.1 Numerical results for mechanical behavior using the FEM

Within the context of mechanical studies, the force–displacement relationship is key in understanding how a component behaves under tension/compression. The reason is that, unlike stress and strain (which are local quantities), force and displacement are global parameters that can be easily obtained experimentally. It essentially measures the stiffness of the system at every point, i.e., how it responds under loading.

As mentioned in Section 2.1.2 and highlighted by Zeng et al. (2021), the force–displacement curves for LS follow a – generally speaking – regular pattern of elastic deformation, plateau, and densification. Fluctuations can of course occur along the way, especially because the usual deformation mechanism of LS involves a layer-by-layer failure (Ghaemi Khiavi et al., 2022), where the cell walls eventually touch (leading to densification).

The force–displacement correlation is also the key concept behind the Finite Element Method (FEM), where the displacement is calculated at every node in a mesh by solving the $\mathrm{F} = [\mathrm{K}]u$ relationship. Therefore, the modeling of LS behavior using the FEM has become a cornerstone of studies in the field, since a numerical–experimental correlation could potentially alleviate the need for extensive experimentation. Figure 2.19 shows a comparison between the experimental vs. simulated shape of a lattice structure under side-compression.

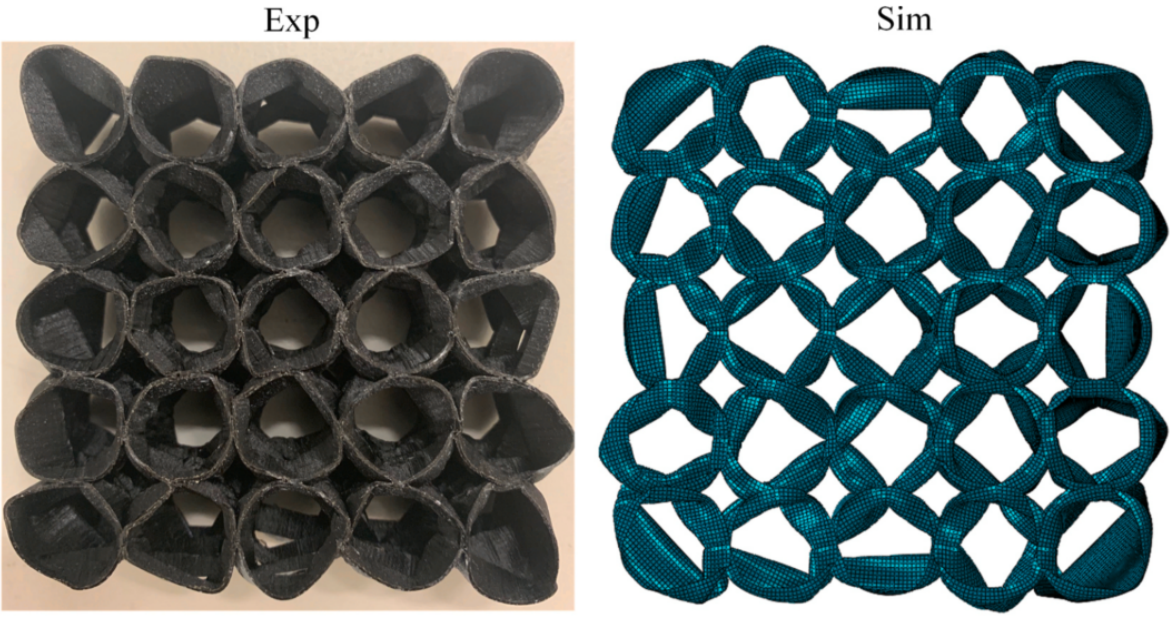

Figure 2.19: Experimental and numerical deformation of the non-hierarchical and hierarchical circular 2D lattices from Ha et al. (2022), showing the model's ability to predict the deformation modes.

In the beginnings of CS studies, researchers heavily relied on analytical models, especially to determine CS stiffness by using the base material as a starting point – as the already discussed Gibson–Ashby relationships describe. However, as early as the 1990s, researchers were already turning their attention towards the FEM for predicting their behavior, especially since their arrangement was becoming quite intricate for analytical models to handle.

Theocaris et al. (1997), for instance, used a simple bi-dimensional beam model to study the mechanical response of an auxetic star-shaped structure, and how the beam's angles affected parameters such as the Poisson's ratio – by noting that a similar model had been previously used to successfully predict such behavior. Zhang and Lu (2023) employed the FEM to study re-entrant auxetic 2D lattices and compared against analytical equations – showing a good match between the force–displacement curves predicted by each method (Figure 2.20). Saxena et al. (2016) note that, especially in the case of auxetic structures, researchers have come to find analytical modeling only useful as a "crude" or first approach, and that the FEM revolutionized the field by making a proper geometric representation of the mechanical behavior possible.

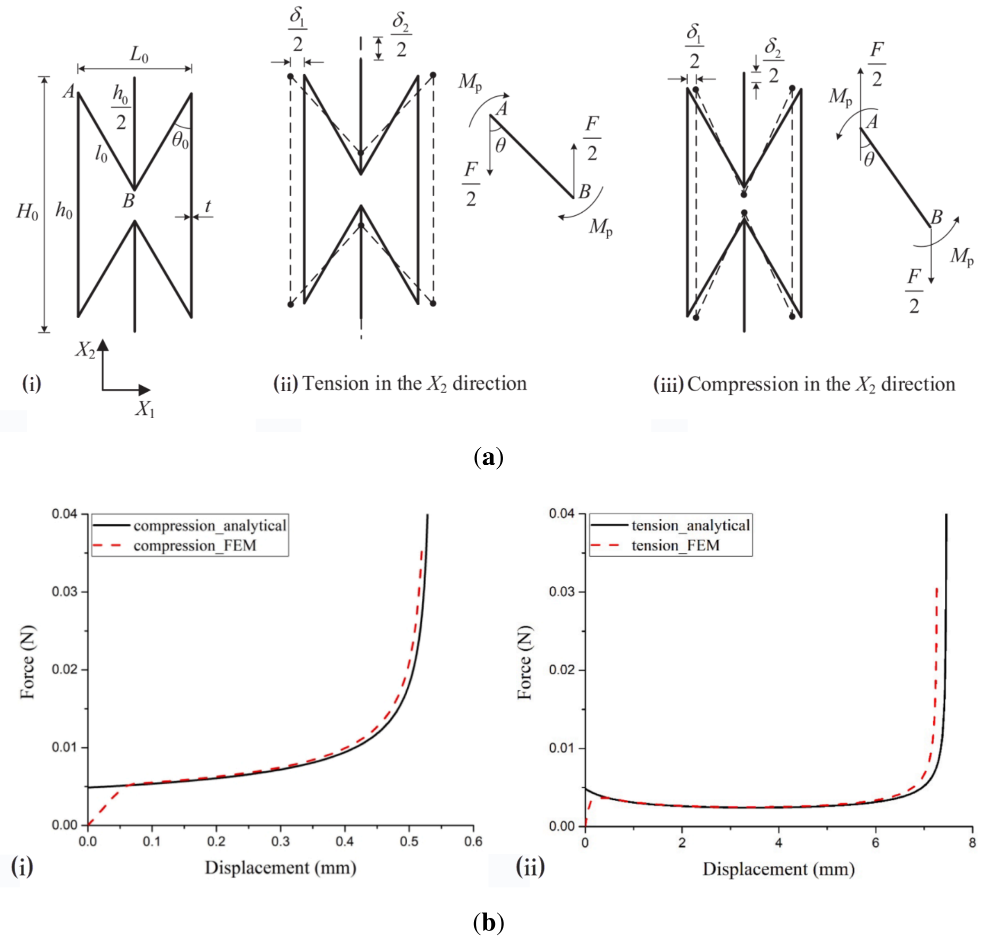

Figure 2.20: Comparison between the analytical and numerical behaviour of a re-entrant auxetic unit. (a) Unit cell geometry (i) deformation mechanisms under tension (ii) and compression (iii), following the formulation used by Zhang and Lu (2023). (b) Force–displacement response of the same unit under compression (i) and tension (ii).

If this is the case for auxetic LS, which can often be modeled as simple bending or stretching beams, the FEM becomes much more relevant when it comes to more advanced LS. The advancements in computational technology also allowed for a paradigm shift in terms of 3D modeling in general and more elaborate FEM simulation specifically, which enabled the prediction of intricate behavior and interactions such as complex contacts (e.g., when the LS reaches the densification stage).

There has also been wide agreement among authors that FEM simulations can accurately predict mechanical behavior. Zhou et al. (2023), for instance, studied the energy absorption capabilities of 2D lattices using different unit cell geometries – honeycomb, re-entrant, and double arrow-headed – and found a good correlation between FEM results and experimental ones, with the energy absorption staying within a 10% difference for most samples. The force–displacement curves also presented good matching, and they attributed the differences to the tolerance of the machine utilized to fabricate the samples. Furthermore, geometric patterns observed in compressed real-life samples were also observed in the FEM simulations, highlighting the ability of the numerical representation to predict the mechanical response of the system. Li et al. (2023) found an almost 1-1 matching between the stress–strain curves of simulated vs. experimental 2D lattices, and the simulation also accurately predicted the observed deformation patterns, including a side-shift (Figure 2.21).

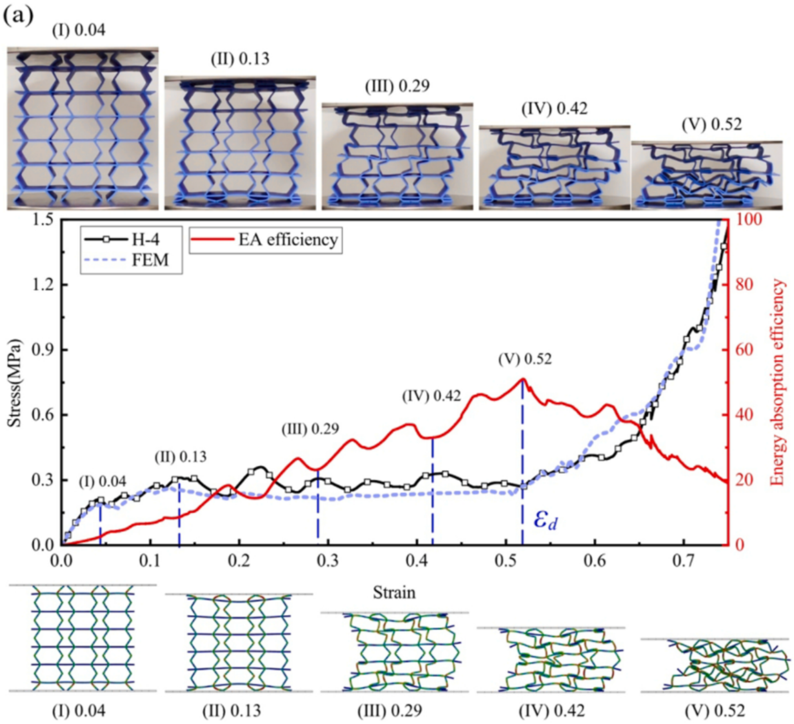

Figure 2.21: Compressive deformation behavior of a hexagon 2D lattice and consistency between experimental results and finite element simulation (FEM). Adapted from Li et al. (2023).

On a similar note, Ha et al. (2022) developed 2D lattices with a circular unit cell and compared a non-hierarchical structure with a hierarchical one. They reported a close matching between the experimental and numerical force–displacement curves, with a small shift at the peak point, which they attributed to the FEM model not considering fracture damage, as shown by Figure 2.22. However, the final shapes and compressive behavior were tightly matched, and the results for mean crushing stress presented almost perfect agreement, for instance less than 4% difference at 0.7 strain.

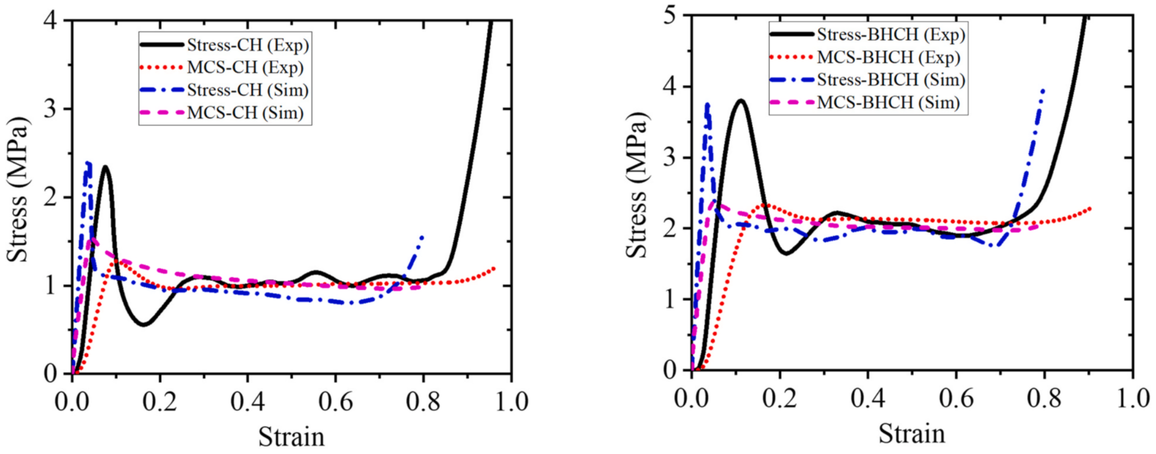

(**a**) Non-hierarchical circular 2D lattice

(**b**) Hierarchical circular 2D lattice

Figure 2.22: Stress–strain curves reported by Ha et al. (2022) for (a) a non-hierarchical circular 2D lattice and (b) a hierarchical circular 2D lattice.

Ingrole et al. (2017) also studied 2D lattices by comparing a hexagonal unit cell with a re-entrant auxetic and a combination of both patterns. They examined the nominal stress–strain curve for all samples and noticed that the FEM model was able to capture the experimental curves' formats, as well as the deformed shape of the structure. Similar to Zhou et al. (2023), the authors attributed the difference in the curves to the inconsistent thickness of the printed parts, as well as to small defects resulting from the fabrication process.

Sharma and Hiremath (2023) studied the experimental and FEM analysis of bio-inspired lattice structures derived from a sea sponge, and noted how well the FEM simulation predicted the deformation mechanism of the samples, even reproducing the shear band formation. Feng et al. (2022) investigated lattice-walled tubes and compared the force curve obtained experimentally with the FEM. While noting a good match between the curves, they stressed the difficulty in proceeding with the simulation after a certain point and truncated the curve, since the contact interactions start to become more complex and the real structure presents fracture behavior, undercutting the simulation stability.

In Chen et al. (2021)'s review of the AM of metallic lattice structures, it is evident how widespread the FEM has become in LS modelling and design, where they highlight the FEM being used for identifying peak stress regions, observing the stress/strain contours, and even performing topology optimization to achieve lower material consumption. The application fit of the FEM to LS has become crucial to the point that a study almost seems lacking if no FEM result is presented, and most studies gathered to form this literature review present this kind of result – e.g., (Feng et al., 2022; Ghaemi Khiavi et al., 2022; Sharma and Hiremath, 2023; Ha et al., 2022; Zhang and Lu, 2023; Alomar and Concli, 2021; Zhou et al., 2023).

### 2.3.2 Common Strategies for FEM modeling of Lattice Structures

There are three main crucial factors for achieving good results in FEM simulation: CAD preparation, meshing and simulation setup. They are all interconnected, since CAD preparation will influence meshing, and the simulation settings will determine specific requirements for both CAD preparation and meshing. Therefore, its of high importance to understand how researchers have modeled the problem to achieve reliable results.

Before turning to the commonly chosen parameters, however, its key to highlight how exactly the comparison is made to determine whether FEM simulations are in good agreement with experimental data. While analyzing AM multi-material studies – commonly used to fabricate LS –, Nazir et al. (2023) lament that, although there are many employing the FEM, only a minority compared against experimental results.

A very common way to achieve the desired result of an accurate behavior prediction using the FEM is to start with a simple calibration model, and once the results are matching, proceed with the simulation of the LS. The calibration is performed especially to get the material information, since its the fundamental building block of the mechanical response. While there are sources in the literature which provide the data for many materials, its especially crucial to work with a specimen made under the same conditions as the final parts in the case of AM components, since they often present anisotropy as highlighted in Section 2.2.

Förster et al. (2022), for instance, while studying cylindrical LS with different filling patterns under compression, started off with a fully solid specimen manufactured in the same manner as the LS and performed a destructive compression test to compare against simulation data. Similarly, Sharma and Hiremath (2023) performed a tensile test on a specimen and employed the hyperelastic Arruda–Boyce model to compare against true stressstrain data for the specimen, and found an almost 1–1 match between the curves (Figure 2.23).

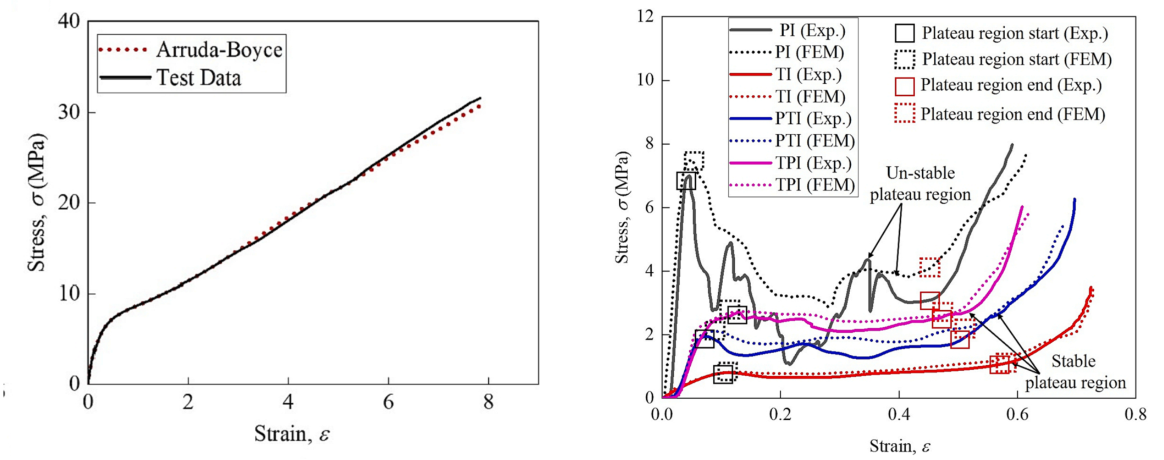

(**a**) Calibration model

(**b**) Experimental and numerical compressive stress–strain responses of in-plane 2D lattices

Figure 2.23: Calibration of FEM simulations: (a) Arruda–Boyce model fitted to tensile test data for the TPU material; (b) resulting correspondence between experimental and FEM responses. Adapted from Sharma and Hiremath (2023).

After material properties are set, the next step is to prepare the geometries for the simulation, which begins by determining the dimension of the study, i.e., if the problem can be approximated by beams or shells – or if its crucial to have a fully tri-dimensional approach. While the tri-dimensional approach tends to be more accurate, its also more computationally expensive and will require a larger number of nodes to potentially capture the same behavior – and it cant be considered the default go-to approach for every application, as noted by Ai and Gao (2017). If one or two dimensions are too small in comparison to the others, this generates issues in the meshing step, since elements will either need to be very small to keep a good aspect ratio or become highly distorted (especially if the part is not sweepable). For strut-based 3D lattices, its a common practice to use 3D or even 2D beam elements for modeling, as already discussed in Section 2.3.1.

However, while this might be the case if the walls are slender, in many applications – such as extruded 2D lattices – this assumption falls short and a more robust approach becomes necessary. The next modeling alternative is to implement shell elements, which are two-dimensional elements used to approximate thin wall behavior, i.e., when the thickness is small in comparison to the other two dimensions (see Figure 2.24 for a 2D CAD example). An advantage of using shell elements is that the thickness direction is not resolved by the simulation, only modeled, which dramatically reduces the node count for a high-quality mesh. Another interesting upside to shell-element simulations is that its possible to alter the thickness for specific walls without the need of changing the CAD model, and this approach was used by Zhou et al. (2023) to account for variations in wall thickness coming from the manufacturing process.

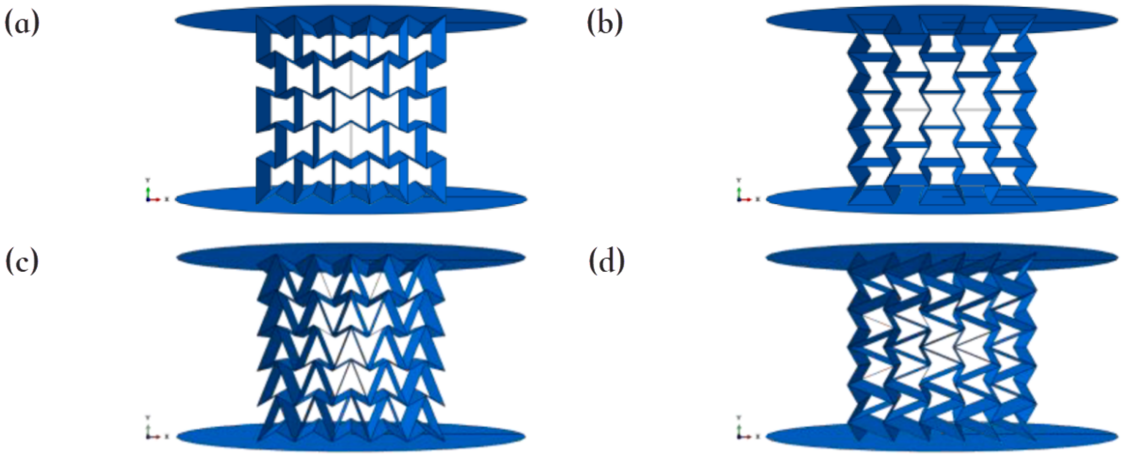

Figure 2.24: Representative CAD models and loading configurations used by Zhou et al. (2023) to simulate thin-walled 2D lattices.

Ha et al. (2022) also used thin wall elements in their study, which was particularly beneficial due to the highly complex contact interactions in the structure, because of a successive folding of the geometry as it was compressed. In the case of thin-walled TPMS LS, modeling them as tri-dimensional would also require a much higher computational effort, while their mechanical response can be accurately predicted by using shell elements, and this approach was used by studies such as those from Wang et al. (2020) and Sun et al. (2022). Regarding the element type, all studies previously mentioned used 4-noded (first order) quadrilateral elements.

In cases where the walls cant be considered thin, tri-dimensional modeling needs to be employed to accurately capture the mechanical behavior. One example where this is the case is illustrated by Al-Saedi et al. (2018) and Xiao et al. (2017), where some of the LS present larger diameter struts and the models were meshed with 3D elements (Al-Saedi et al. (2018)'s example is shown in Figure 2.25). The element type for 3D studies is not as uniform as for 2D or 1D studies, and there doesnt seem to be a consensus on whats the best choice upfront. To name a few examples, Al-Saedi et al. (2018) used first-order tetrahedral elements, Alhembar et al. (2023) also employed tetrahedral elements but didnt specify the order, and Förster et al. (2022) employed second-order tetrahedral elements, with the exception of one specimen for which the contact interactions became too complex and it was switched back to first-order. On the other hand, Xiao et al. (2017) employed first-order hexahedrons, which illustrates the variety existent in the choice of element type for this kind of study.

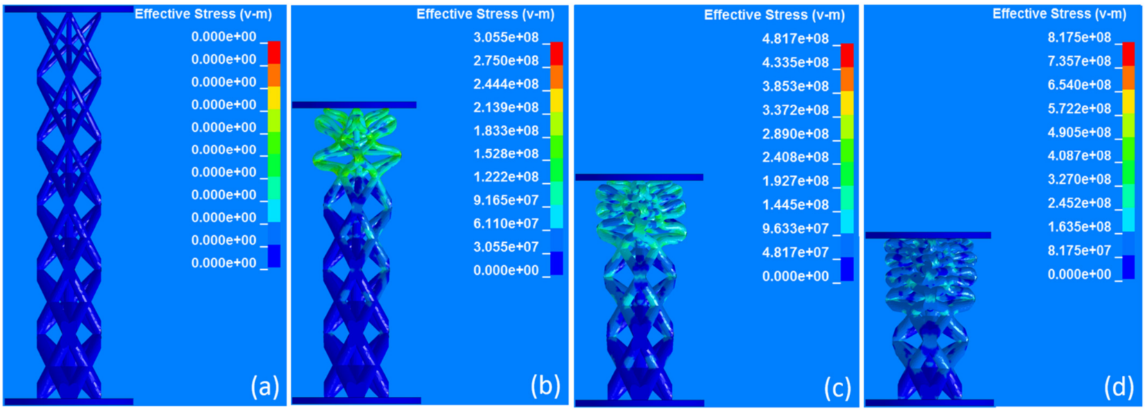

Figure 2.25: Deformation sequence of a graded lattice structure under compression as predicted by Al-Saedi et al. (2018).

In terms of boundary conditions, LS compression simulations tend to be constraint-driven rather than force-driven; usually displacement is controlled – e.g. Du et al. (2020); Alhembar et al. (2023) – and applied to a rigid body or plate at the top, while the bottom is constrained by a fixed plate or body (Figure 2.26) – e.g. Sharma and Hiremath (2023); Ha et al. (2022); Wang et al. (2020).

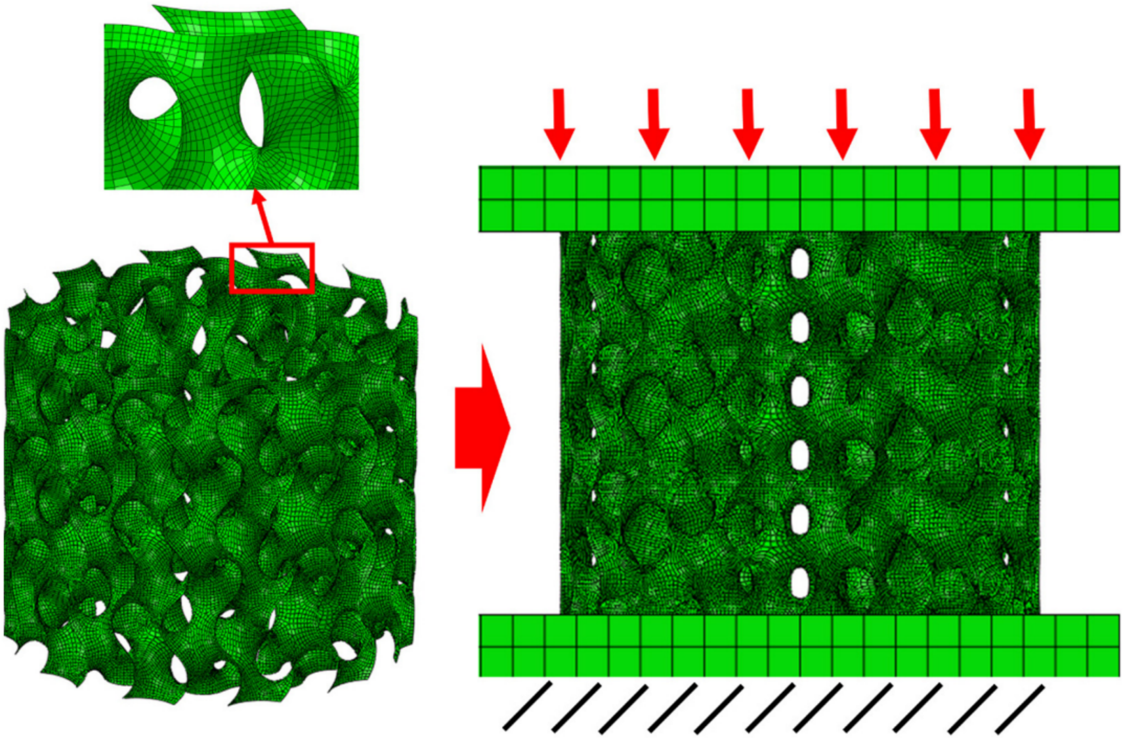

Figure 2.26: Boundary conditions used by Wang et al. (2020) for simulating the compressive response of lattice structures. A rigid plate at the top is displaced downward to drive the deformation, while the bottom plate is fully constrained.

Most of the studies evaluated used a dynamic explicit rather than a static implicit solver, likely due to the robustness of the former in dealing with complex contact interactions. However, since simple LS compression is indeed quasi-static in nature – in the sense that inertia effects dont play a major role and the displacement is applied slowly – the problem can be solved using an implicit solver, which might be preferred since studies using the explicit dynamic one tend to reccur to numerical artifices, such as mass scaling – employed for instance by Feng et al. (2022) and Ha et al. (2022) – to forcibly increase the timestep length.

As a final note, some studies are already looking into future trends in engineering simulation, and how this might impact LS specifically. As an example, Garg et al. (2025)s review on data-driven artificial intelligence (AI) applications for 3D printed auxetic structures specifically highlights opportunities to advance the understanding and application of auxetic metamaterials using machine learning techniques. The review emphasizes that a significant research gap exists in applying machine learning for predicting their mechanical properties, despite recent advancements in the field.

AI is driven by the data it's trained on, so that FEM simulations present a key component of the future of engineering – since parametrization studies can be performed to tighten the AIs knowledge gap. Within this context, companies such as SimScale GmbH are working tirelessly to bridge the gap between engineering and AI and provide a rightful place for the new technology in engineering workflows.

# Chapter 3

# METHODOLOGY

The overall workflow adopted in this dissertation followed three main steps. First, the material model was calibrated using experimental data obtained from a WLAM-fabricated ER70S–6 tensile specimen. Second, the resulting multilinear elastoplastic behavior was implemented within the finite element method (FEM) environment. Third, the calibrated model was validated through a comparative analysis between numerical simulations and experimental results, using WLAM-fabricated lattice specimens. The following sections describe each of these steps in detail. The experimental data was provided by INEGI, whose researchers conducted the manufacturing and experimental procedures using the specimens.

## 3.1 Calibration Case: WLAM Tensile Specimen

### 3.1.1 Specimen Geometry

The test specimen was designed in accordance with the ASTM E8 (ASTM, 2024) standard, with 25 mm gauge length, 6mm width and 3mm thickness. Its dimensions are outlined in Figure 3.1.

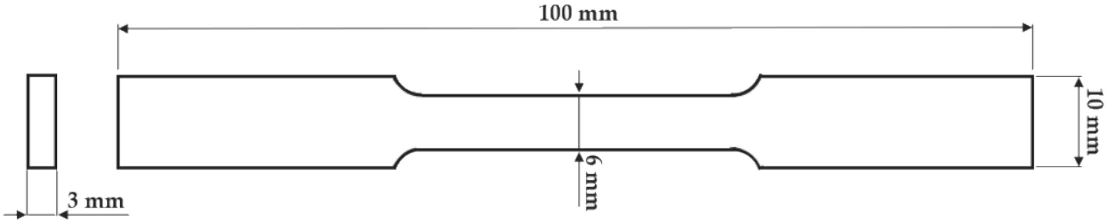

Figure 3.1: Tensile test specimen drawing with dimensions, designed in accordance to ASTM E8 (ASTM, 2024). Provided by INEGI.

### 3.1.2 Experimental Setup and Manufacturing Process

An initial specimen block was manufactured using the WLAM process, then the specimen was obtained via a Wire EDM cutting process. The specific equipment used was the Meltio Engine V3 Robot Integration (Figure 3.2), and its specifications are highlighted in Table 3.1.

Figure 3.2: Meltio Engine V3 Robot Integration. Provided by INEGI.

| Specification | Value |
|---|---|
| Dimensions [mm] | 390x700x1025 |
| Print Envelope | Depending on the integration |
| System Weight [kg] | 142 |
| Laser Type | 6 x 200 W direct diode lasers |
| Laser Wavelength [nm] | 976 |
| Total Laser Power [W] | 1200 |
| Power Input | 208/230 V – 400 V compatible (3-phase) |
| Power Consumption [kW] | 2–5 (peak) |
| Cooling | Active water-cooled chiller included |
| Wire Feedstock Diameter [mm] | 0.8–1.2 |

Table 3.1: Technical specifications of the Meltio Engine V3 Robot Integration, compiled from the manufacturer-provided data.

As mentioned in Section 2.2.1, the process characteristics are key in determining the mechanical behavior of WLAM manufactured components. In that sense, the global parameters used are highlighted in Table 3.2.

| **Parameter** | **Value** |
|---|---|
| Layer Height [mm] | 1.0 |
| Deposition Width [mm] | 1.2 |
| Overlap [%] | 0% |
| Seam | Aligned |
| Print Speed [mm/s] | 6.5 |

Table 3.2: Processing parameters (defined in slicer).

However, due to the already mentioned directional dependency of mechanical properties in terms of energy input, the power, feed rate and energy density were adjusted layer by layer. 15 layers were produced in total, with the already mentioned 1mm layer height, and the parameters for each layer were adjusted according to Table 3.3 as follows:

- Layer 1-3: Option 1;
- Layer 4-6: Option 2;
- Layer 7-12: Option 3;
- Layer 13-15: Option 2.

| | **Option 1** | **Option 2** | **Option 3** |
|---|---|---|---|
| Power [W] | 1060 | 1000 | 1020 |
| Feed Rate [mm/s] | 10.56 | 10.56 | 10.56 |
| Energy Density [J/mm$^3$] | 135.83 | 128.15 | 130.71 |

Table 3.3: Processing parameters (defined in Meltio's dashboard).

The specimen was manufactured using a vertical layer-by-layer deposition strategy. In this setup, the characteristic planar geometry of the specimen is defined in the horizontal (XY) plane, while the structure is built upwards along the vertical (Z) axis. Figure 3.3 presents a schematic of this process: while a circular toolpath is shown for illustrative purposes, the actual deposition followed the specific contour of the specimen. Furthermore, the figure details the stacking sequence in the thickness direction and explicitly indicates the orientation of the applied load relative to the build layers.

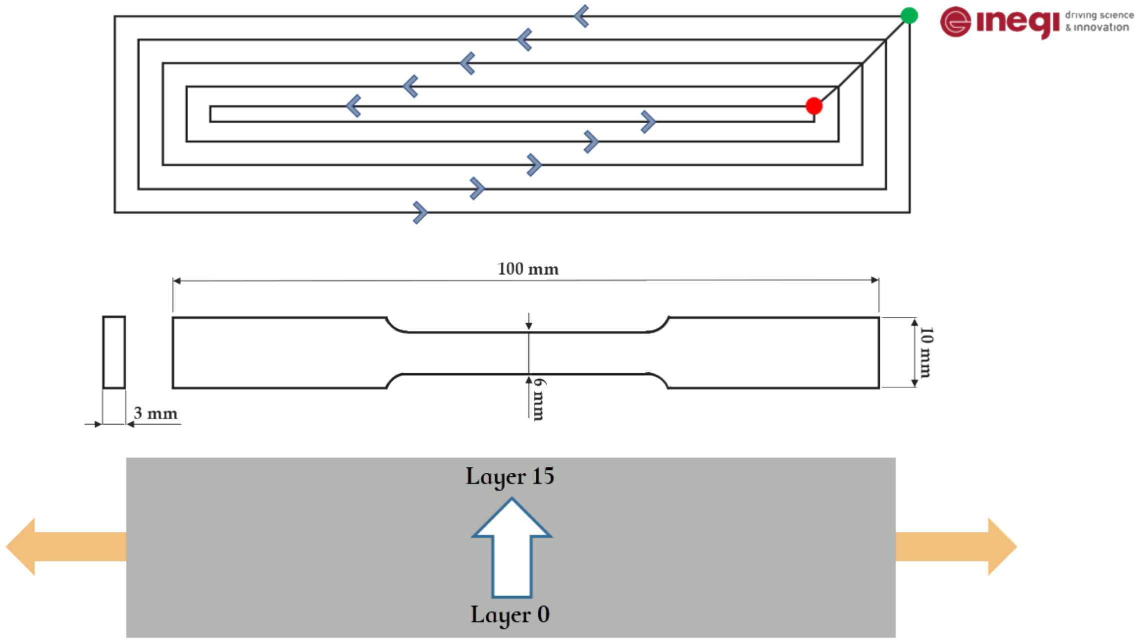

Figure 3.3: Image illustration of the utilized toolpath (top) and how the specimen block was built layer by layer. Yellow side arrows show applied load direction. Provided by INEGI.

Finally, the specimen was extracted from the final block for submission to a tensile destructive test. The test was performed using an Instron 1000HDX-1,000 kN machine (Figure 3.4) up to failure, with a 1mm/min displacement speed. The force data was obtained directly from the machine's load cell, with the displacement being measured by a strain gauge (gauge length = 25mm) for enhanced accuracy.

Figure 3.4: Instron 1000HDX universal testing machine used for the tensile destructive test. Provided by INEGI.

### 3.1.3 Data Processing and Material Model Extraction

As mentioned in the previous section, the output from the tensile test was the force–displacement curve for the specimen. The data was then curve-fitted using the optimization algorithm developed by Silva (2024), which uses simulation results to find the best parameter combination which fits the experimental data according to the Kleinermann–Ponthot (Kleinermann and Ponthot, 2003) hardening law (described by Equation 3.1).

$$\sigma_y = \sigma_{y0} + \xi\bar{\varepsilon}^p + (\sigma_\infty - \sigma_{y0})(1 - e^{-\delta\bar{\varepsilon}^p}) \tag{3.1}$$

Where $\sigma_y$ is the updated yield limit, $\sigma_{y0}$ is the initial yield limit, $\bar{\varepsilon}^p$ is the equivalent plastic strain, $\xi$ is the isotropic hardening modulus, $\sigma_\infty$ is the maximum stress and $\delta$ is the hardening exponent. A useful summary of the characterization method is provided by Da Silva et al. (2024).The obtained parameters are summarized in Table 3.4.

| **Parameter** | **Value** |
|---|---|
| $\sigma_{y0}$ [MPa] | 564.57 |
| $\xi$ [MPa] | 62.04 |
| $\sigma_\infty$ [MPa] | 770.62 |
| $\delta$ [-] | 9.12 |

Table 3.4: Obtained parameters considering the Kleinermann–Ponthot isotropic hardening law (Equation 3.1).

Since the FEM software employed (Abaqus/CAE) didn't include a dedicated model implementation for Kleinermann-Ponthot, Equation 3.1 was utilized to obtain a multilinear elastoplastic material curve from the fitted parameters (Figure 3.5). This approach simply takes a group of data points for stress and equivalent plastic strain, which in turn are fed into the material model in Abaqus, with values in-between being linearly interpolated.

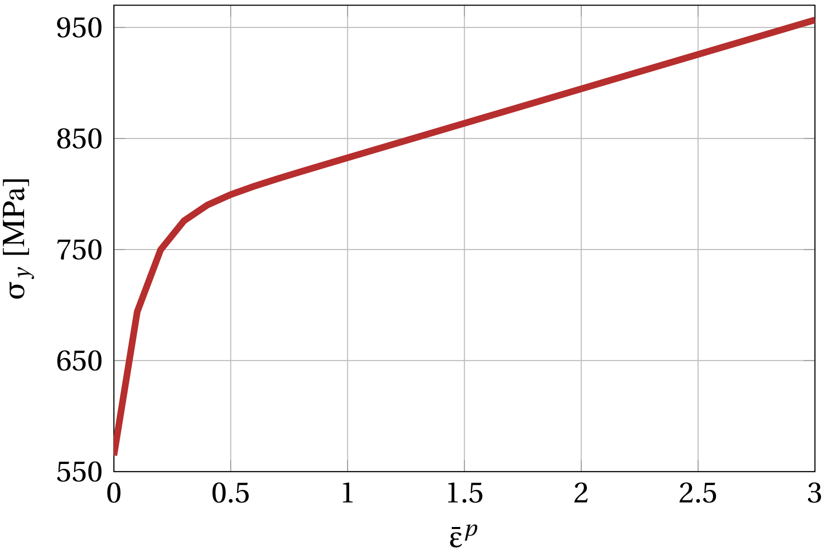

Figure 3.5: Evolution of $\sigma_y$ as a function of the equivalent plastic strain according to the Kleinermann–Ponthot isotropic hardening law and the fitted parameters.

### 3.1.4 Numerical Simulation Setup (Calibration Model)

The next step in numerically validating the material curve is to set up a simulation that models the tensile test, then compare the numerical and experimental results for the force–displacement relationship. For that purpose, a simple CAD model of the specimen's region of interest was created within the Abaqus/CAE environment as a bi-dimensional shell (Figure 3.6). The specimen was assumed to behave under a plane strain approximation, so that a three-dimensional model wouldn't be necessary – which was considered a fair approximation for the model calibration. Another assumed approximation was the symmetry one at the mid-section of the test specimen, which will be described in more detail in the boundary conditions section.

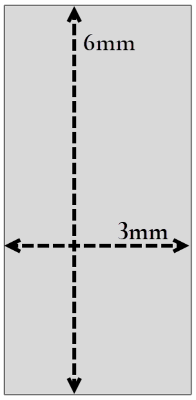

Figure 3.6: Bi-dimensional CAD representation of the region of interest used for the calibration tensile simulation.

The material was assigned following the data obtained by the optimization algorithm mentioned in the previous section. The key material properties are outlined in Table 3.5.

| **Parameter** | **Value** |
|---|---|
| E [GPa] | 240 |
| ν [-] | 0.33 |
| Elastoplastic Model | Multilinear |

Table 3.5: Material properties used in the simulations. Here, E denotes the Young's modulus (elastic modulus) and ν is the Poisson's ratio.

In terms of meshing strategy, second order, plane strain, quadrilateral elements (Quad-8) with full integration were employed. The choice was related to the high deformation of the elements, especially after the necking stage, so that the higher accuracy of the second order elements was key in achieving good numerical results. A bias was applied to the side edges in the direction of the specimen's mid section (specimen's end in the simulation, because of the symmetric approach), to achieve a greater accuracy at the higher deformation region. Figure 3.7 shows the resulting mesh.

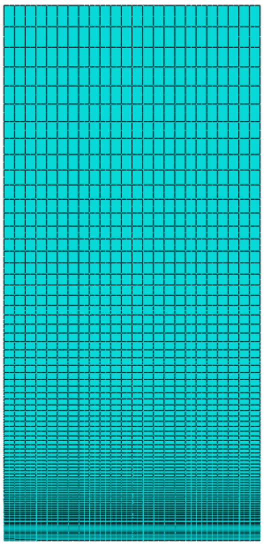

Figure 3.7: Finite element mesh used for the tensile simulation, composed of second-order, plane-strain quadrilateral (Quad-8) elements with full integration.

The analysis type was static with geometric non-linearity enabled, since the displacement rate is low enough that the problem can be considered quasi-static. Two boundary conditions were applied: a fixed displacement at a control point in the upwards direction – coupled with rigid kinematic connections to the top surface – whereas the other degrees of freedom were fixed at 0; and a planar symmetry at the bottom edge, which allows for planar motion while restricting normal displacement and the in-plane rotations.

The output of the simulation were the default field variables, i.e., Von Mises stress, Cauchy Stress, Displacement, PEEQ, etc. and an extra history output was requested at the control point to retrieve the force–displacement response of the system. A summary of the simulation setup is shown in Table 3.6.

| Parameter | Value |
|---|---|
| Analysis Type | Nonlinear Static (Implicit) |
| Analysis Dimension | 2D Shell (Plane Strain) |
| Element Type | Quad-8 (Plane Strain) |
| Number of Nodes | 7375 |
| Material | ER70S-6 |
| Elastoplastic model | Multilinear |
| Boundary Conditions | Displacement (top); symmetry (bottom mid-section) |
| History Output | Force at the control point |

Table 3.6: Summary of the calibration numerical simulation setup.

### 3.1.5 Summary of Calibration Results

After the simulation was performed, a qualitative analysis of the solution fields showed a good agreement between the expected behavior and numerical results. At first, in the elastic region, the stress gradually grows until a concentration starts to appear at the mid-section of the specimen (Figure 3.8**b**). After necking occurs, the deformation at this point grows and the expected near-fracture shrinkage takes place (Figure 3.8**c**).

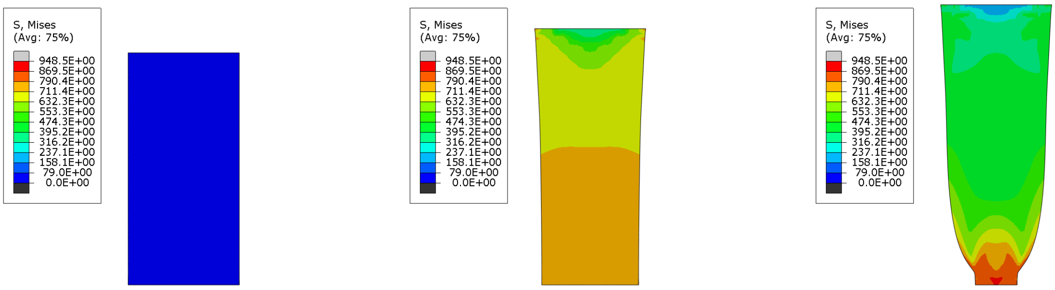

(**a**) Initial configuration (elastic regime).

(**b**) Onset of necking and stress localisation.

(**c**) Postnecking deformation approaching fracture.

Figure 3.8: Evolution of the von Mises stress field along the tensile test simulation.

After this initial sanity check, the force–displacement curve was extracted and compared against the test data for the test specimen. Figure 3.9 displays a comparison between experiment and simulation results for force–displacement. The results show an almost 1-1 matching between the experimental and numerical curves, which provides good confidence that the material behavior was accurately captured and could be added to the LS simulations. The specific details of the experimental-numerical procedure adopted for the LS is outlined in the following section.

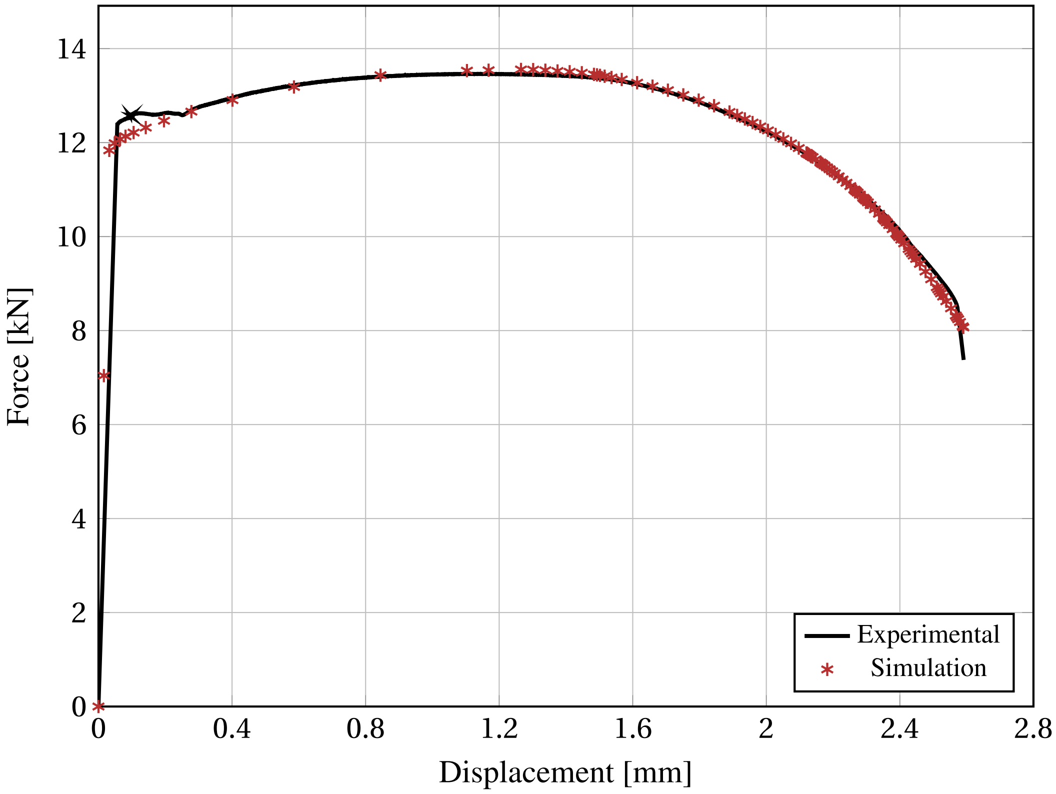

Figure 3.9: Comparison between experimental and simulated forcedisplacement curves.

## 3.2 Validation Case: WLAM Lattice Specimens

### 3.2.1 Lattice Geometries

A total of six different LS patterns were developed for manufacturing using the WLAM process, namely: Circle, Diamond, Hexagon, Square, Triangle and Wavy. Their design consisted in choosing a base pattern, placing it into a rectangular grid using a CAD software, then extruding across the thickness. The strut thickness was kept constant for all samples at 2.4mm, and the resulting geometries and volume fractions are presented in Figure 3.10.

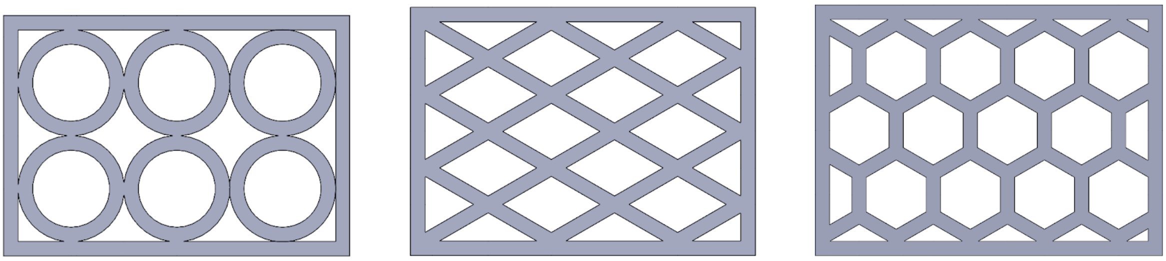

(**a**) Circle pattern
57×40×10 mm, VF = 50%

(**b**) Diamond pattern
57×43×10 mm, VF = 51%

(**c**) Hexagon pattern
59×42×10 mm, VF = 49%

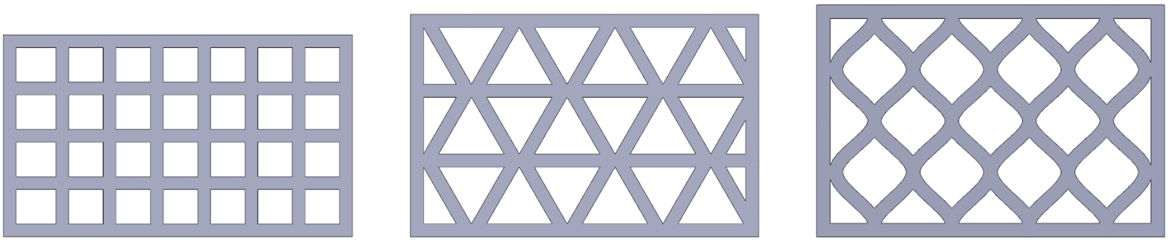

(**d**) Square pattern
55×38×10 mm, VF = 45%

(**e**) Triangle pattern
57×41×10 mm, VF = 52%

(**f**) Wavy pattern
61×41×10 mm, VF = 49%

Figure 3.10: Geometries of the six lattice structure patterns manufactured using the WLAM process. Provided by INEGI.

### 3.2.2 Manufacturing and Compression Testing Procedure

The lattice structures were manufactured using the same vertical deposition strategy described in Section 3.1.2. The geometries were constructed layer-by-layer along the Z-axis, with a circular path being produced in the XY plane, consisting of 15 superimposed layers of approximately 1 mm in height each. The processing parameters remained identical to those used for the tensile specimen block. To obtain the final dimensions, the 15 mm as-built blocks were subjected to Wire EDM, which removed the top and bottom layers to extract a central 10 mm thick section. This process ensured uniform surface quality and parallelism. A total of 18 specimens were fabricatedthree replicates for each geometryas displayed in Figure 3.11.

(**a**) Circle pattern (**b**) Diamond pattern (**c**) Hexagon pattern

(**d**) Square pattern (**e**) Triangle pattern (**f**) Wavy pattern

Figure 3.11: Manufactured WLAM lattice structure specimens for the six patterns developed. Provided by INEGI.

After the specimens were manufactured, each was submitted to a compression test using the same Instron machine described in Section 3.1.2. The experimental setup consisted in the LS being sandwiched by two rigid guides, and the top guide was placed under a steel cylinder with a 60mm diameter and 94mm length, for a best adjustment with the actuator (since the samples were small in length). The load was then applied at the top face of the cylinder, as presented in Figure 3.12.

A displacement rate of 0.5mm/min was applied to each specimen, with a total displacement of 25mm, and the force–displacement data was measured by the machine's load cell. The mean curve for each geometry was computed by taking the average of the three resulting curves.

Since the measuring technique was highly sensitive to the actuator's stiffness, it's lone force–displacement curve was obtained by performing a compressive test on the actuator. A polynomial fit was made to calculate a displacement from the applied load, which was then subtracted from the mean curves.

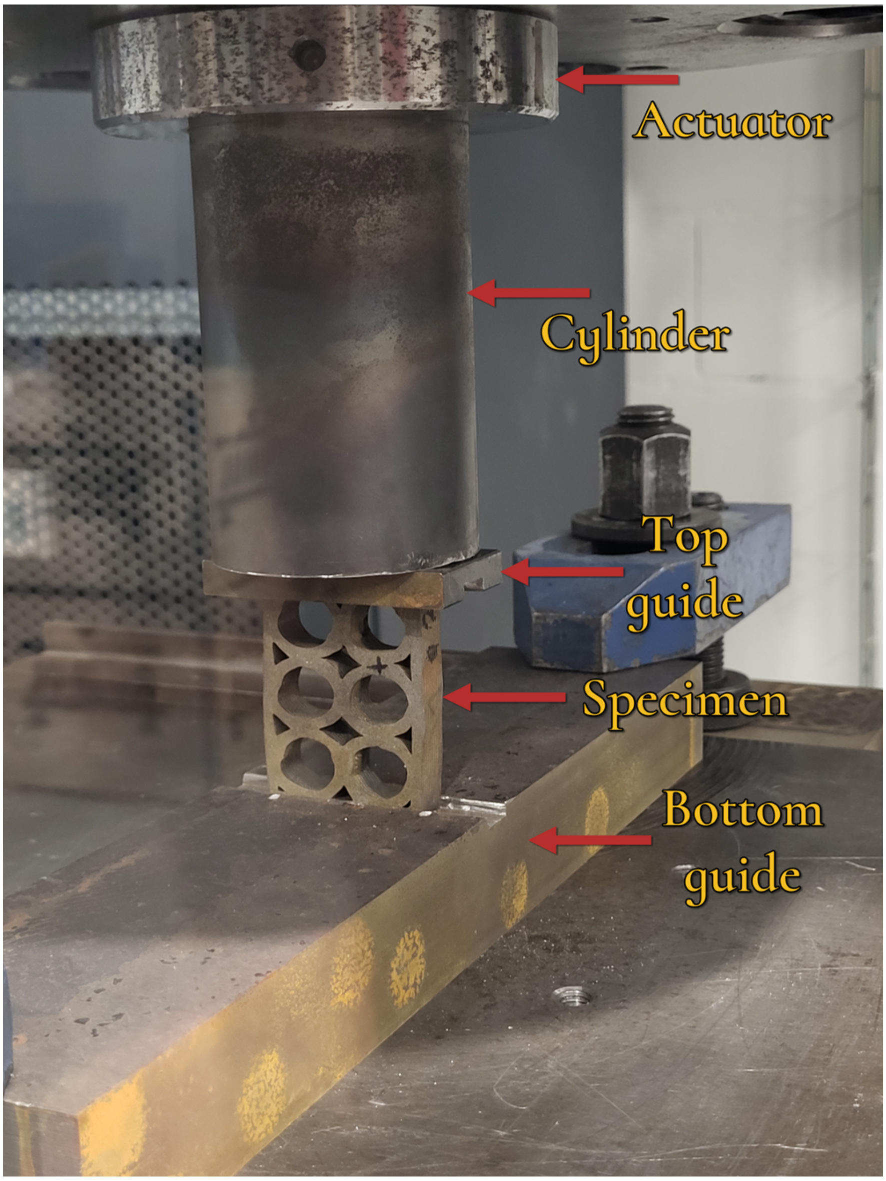

Figure 3.12: Experimental compression test setup used for the manufactured lattice structures. Adapted from INEGI.

### 3.2.3 Numerical Simulation Methodology for Lattices

The first step in setting up the LS simulations was to ensure a proper CAD preparation step. To achieve that goal, the cloud-native CAD software *OnShape* was used to clean the CAM geometries and get them ready for simulation, especially by eliminating small faces and gaps intentionally inserted for manufacturing purposes. Another key step in the cleanup process was to eliminate from the CAD unrealistic geometric features such as infinitely sharp corners since, in reality, the machine's tolerance will produce a small radius instead of a sharp corner. The radii were measured to ensure dimensional accuracy: the external ones measured 2 mm and the internal ones 1mm, with the exception of a few which measured 0.5mm due to the robot's path.

A final adjustment of the geometries was to create the guides in contact with the top and bottom faces (Figure 3.13). The choice of modeling them instead of applying the boundary conditions directly to the top and bottom faces was that boundary conditions – especially constraints – tend to add unrealistic stiffness to the system, which would be problematic in this case since the region of interest is close to where they would be applied.

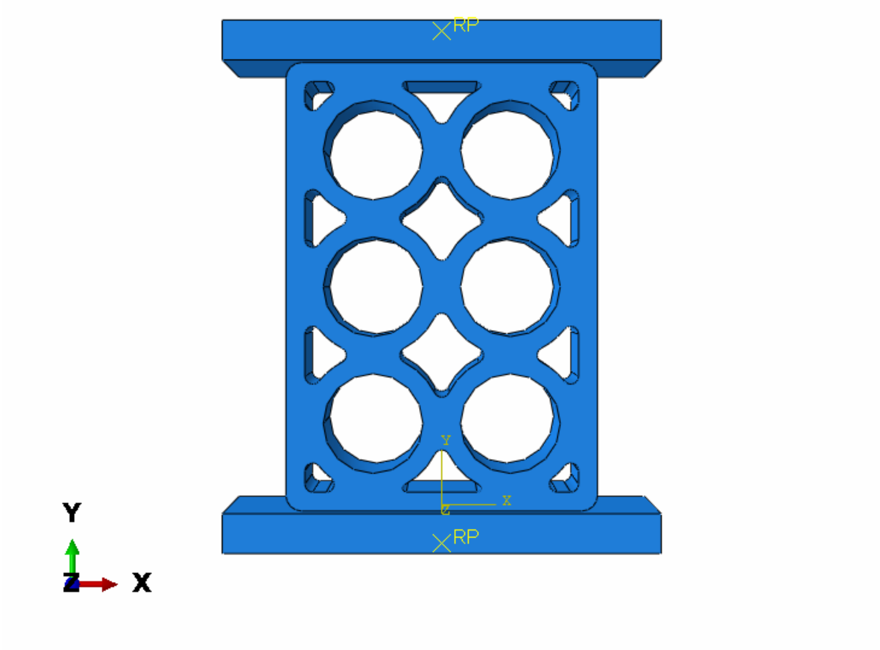

Figure 3.13: Final CAD model used for the numerical simulations, including the rigid guides at the top and bottom faces of the lattice structure.

With the geometries ready for simulation, they were imported into Abaqus/CAE, and the modeling began by assigning the material settings. The guides were converted to rigid surfaces, excluding the need to assign a material section. The material for the LS was assigned using the previously mentioned multi-linear elastoplastic model, with the data obtained from the calibration study.

Then, the mesh was generated for both the LS and the guides (Figure 3.14). As the guides were rigid surfaces, there wasn't a need for a very fine mesh and rigid Quad-4 elements with reduced integration were chosen, and the global mesh size was set to 0.5mm. For the LS, a mesh with no refinements was generated using hexahedral, second order elements (Hex-20) as element type, with a 0.8mm global size.

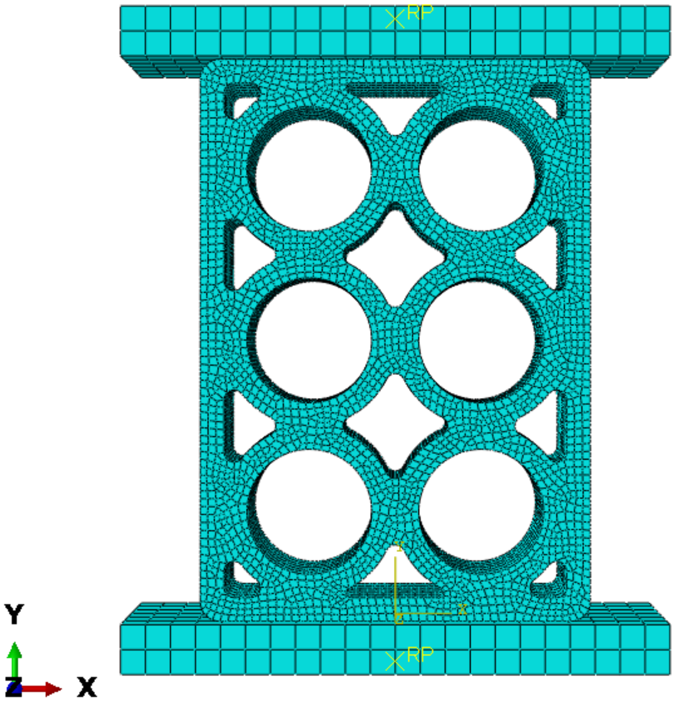

Figure 3.14: Finite element mesh generated in Abaqus/CAE for the lattice structure and the rigid guides. The guides were meshed with rigid Quad-4 elements and the lattice structure used second-order Hex-20 elements (Hex-20).

The hexahedral element was chosen because of it's well-known robustness in comparison to the tetrahedral one, and the extruded nature of the geometries allowed for it's simple implementation. In terms of mesh order, the second order elements are especially suited for bending problems, since they dispose of a quadratic interpolation of the displacement field. Therefore, since the geometries of the unit cells were bending dominated (as per Ashby (2006)'s classification), the problem points in the direction of using second order elements.

To verify this initial assumption, a mesh convergence study was performed by picking the Hexagon pattern geometry and submitting it to a simple compression study, where a 1000N load was applied at the top face as the bottom was fixed, with the displacement at the top face being measured. The parametric variable was the global size at the surface, with the number of layers across the thickness being kept constant at 8 to avoid an overly large mesh.

The global size values of 1mm, 0.7mm, 0.5mm and 0.3mm were evaluated for both geometries, in addition to a 0.1mm value for the linear elements to achieve a higher node count and compare against the quadratic counterpart. As a result, the linear Hex-8 elements still presented a climbing displacement even after the high refinement level, whereas the quadratic Hex-20 elements presented a hardly varying displacement for every mesh fineness, highlighting their fittingness for this particular case. A comparison between the Hex-8 and Hex-20 displacement values for each mesh size is presented in Figure 3.15.

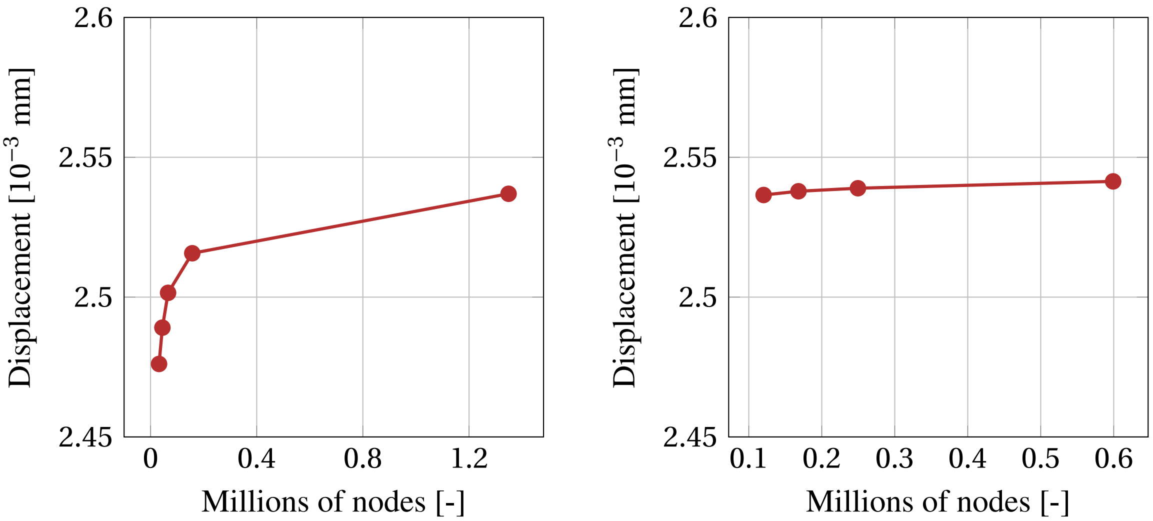

(**a**) Hex-8 (linear elements)

(**b**) Hex-20 (quadratic elements)

Figure 3.15: Mesh convergence study comparing Hex-8 and Hex-20 elements under a 1000 N compressive load.

Due to the complexity of the contact interactions (especially in the densification stage), however, the linear case might be relevant to achieve a higher displacement level without the simulation diverging. The linear case was performed and indeed shows a higher contact stability due to it lacking the mid-edge nodes, and might be quite useful especially for a qualitative assessment of the simulation's success, since the final geometric shape still presented a high resemblance with the real-life result.

That said, the Hex-20 element type was determined as the best choice for this kind of analysis. Since the mesh convergence study presented a low variance even with a low element count, a global size of 0.8mm was deemed appropriate, especially since it would provide roughly three elements across the struts' thickness. Across the geometries thickness, a size of about 1.6mm was enforced by using an edge seed, to enhance the node count and still keep an aspect ratio of 2 for the cells. The final number of nodes used in each LS simulation is presented in Table 3.7

| **Pattern** | **Number of Nodes** |
|---|---|
| Circle | 70750 |
| Diamond | 92996 |
| Hexagon | 96325 |
| Square | 76988 |
| Triangle | 89748 |
| Wavy | 81837 |

Table 3.7: Number of nodes for Hex-20 elements in each LS simulation.

After the meshing step was done, the next step was to establish the analysis type, then the boundary conditions and interactions. As demonstrated by Section 2.3.1, most studies start from a quasi-static assumption and develop a dynamic-explicit simulation to model the compressive behavior for LS. However, for this particular study an explicit simulation was deemed unnecessary, since the timestep easily gets too small, leading to the need of using numeric strategies to artificially increase it. Since the problem starts from a quasi-static assumption, the inertia effects clearly don't play a major role and an implicit, static step with nonlinear geometric behavior was chosen.

Regarding the boundary conditions, they were applied to the rigid guides' reference points, with a fully fixed displacement/rotation being applied to the point at the bottom (at the initial step) and a ramped displacement being applied to the point at the top (at the static step). Even if the experiment was conducted up to 25 mm displacement, a displacement ramp up to 17 mm was applied to the simulations – corresponding to the onset of densification for most geometries – since densification would exponentially increase the simulation complexity and likely lead to divergence (which will be discussed in more detail in Section 4.2.1). The timestep was defined as variable, starting with a 5e-4s value to better represent the linear portion of the force–displacement curves, then ramping up to the maximum value of 0.025s. Note that the total applied displacement was smaller in comparison to the displacement applied to the LS in reality, which is related to the simulation becoming unstable due to the increasingly complex contact interactions that happen at densification, a problem intensified by the use of second order elements. Figure 3.16 gives an overview of the boundary conditions.

In terms of interactions between the parts in the assembly, initially a surface-to-surface contact was initially created for that goal. To stabilize the simulation in the horizontal direction, a tangential behavior with a 0.2 penalty friction coefficient was assigned, as well as a normal behavior with the default “Hard Contact" setting. A self contact was also necessary since the struts eventually touch each other as the structure collapses, and a self contact with the same “Hard Contact" normal behavior and a frictionless tangential behavior was added to the geometries' surfaces.

The final step before running the simulations was to establish the outputs. Besides the default field and history outputs, an additional history output was requested to report the reaction force at the top guide's reference point, in order to obtain the force–displacement response of the system as quantitative XY Data.

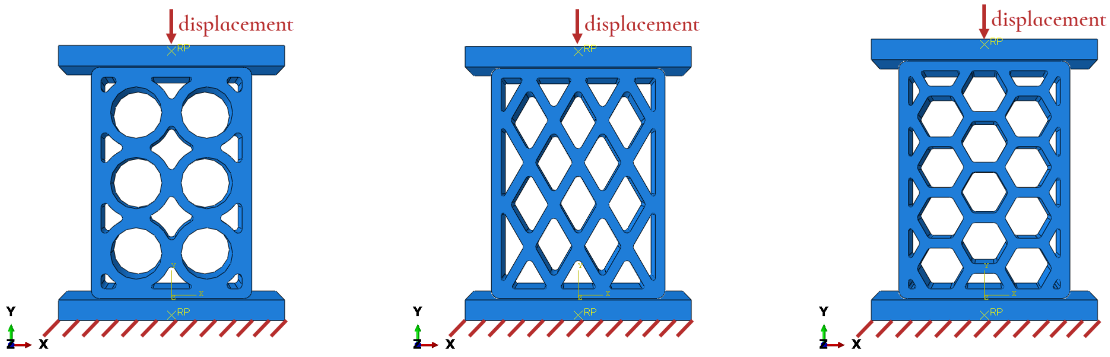

(**a**) Circle pattern (**b**) Diamond pattern (**c**) Hexagon pattern

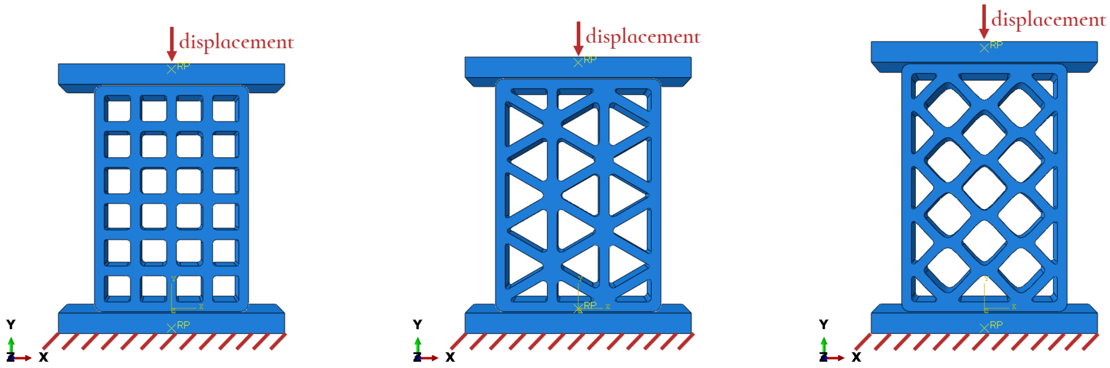

(**d**) Square pattern (**e**) Triangle pattern (**f**) Wavy pattern

Figure 3.16: Boundary conditions applied to the lattice structure simulations.

### 3.2.4 Summary of Validation Setup

Table 3.8, presented below, succinctly summarizes the simulation setup parameters.

| **Parameter** | **Value** |
|---|---|
| Analysis Type | Nonlinear Static (Implicit) |
| Analysis Dimension | 3D |
| Element Type | Hex-20 |
| Edge Length | 0.8mm (global) |
| Material | ER70S-6 |
| Boundary Conditions | Displacement (top guide); encastre (bottom guide) |
| Contact Interactions | Surface-to-surface: normal (hard contact); tangential (0.2 penalty)<br>Self-contact: normal (hard contact); tangential (frictionless) |
| Time-stepping | Automatic, starting at 5e-4s, maximum at 2.5e-2 |
| History Output | Force at the control point |

Table 3.8: Summary of the validation numerical simulation setup.

## 3.3 Energy absorption calculation

As extensively discussed in Chapter 2, one of the key metrics to evaluate the performance of LS is its energy absorption capability. In that sense, the Energy Absorption (EA) can be drawn from the force–displacement curve by simply integrating it from an initial displacement ($x_0$) – which equals 0 – to a final displacement – e.g. 17mm, the final simulated displacement, or simply the common displacement value (smallest final displacement between experiment and simulation). For that purpose, the function `np.trapz("...")` from the *Numpy* library was used in a *Python* script, by also interpolating the curves using `np.` ↪ `interp("...")`.

$$\mathrm{EA} = \int_{x_0}^{x} \mathrm{F}dx \tag{3.2}$$

Then, by using the volume fractions (VF), the lattice bounding box volume ($\mathrm{V}_{block}$) and the solid material density ($\rho_s$), the specific energy absorption (SEA) can be calculated according to Equation 3.3. It's worthy to stress that the VF was used to normalize the energy absorption results (SEA), ensuring a fair comparison between geometries with different relative densities. Table 3.9 shows the relevant geometric data for each manufactured specimen type.

$$\mathrm{SEA} = \frac{\mathrm{EA}}{\mathrm{V}_{\mathrm{block}} \times \mathrm{VF} \times \rho_s} \tag{3.3}$$

| **Pattern** | Dimensions (L × W × t) [mm] | VF [-] | $\mathrm{V}_{\mathrm{block}}$ [$\mathrm{m}^3$] | V [$\mathrm{m}^3$] |
|---|---|---|---|---|
| Circle | 57 × 40 × 10 | 0.50 | $2.28 \times 10^{-5}$ | $1.14 \times 10^{-5}$ |
| Diamond | 57 × 43 × 10 | 0.51 | $2.45 \times 10^{-5}$ | $1.25 \times 10^{-5}$ |
| Hexagon | 59 × 42 × 10 | 0.49 | $2.48 \times 10^{-5}$ | $1.21 \times 10^{-5}$ |
| Square | 55 × 38 × 10 | 0.45 | $2.09 \times 10^{-5}$ | $9.41 \times 10^{-6}$ |
| Triangle | 57 × 41 × 10 | 0.52 | $2.34 \times 10^{-5}$ | $1.22 \times 10^{-5}$ |
| Wavy | 61 × 41 × 10 | 0.49 | $2.50 \times 10^{-5}$ | $1.23 \times 10^{-5}$ |

Table 3.9: Geometric data for each specimen type. Columns show Bounding box dimensions ((Length (L) × Width (W) × Thickness (t))), Volume Fraction (VF), Bounding box volume ($\mathrm{V}_{\mathrm{block}}$) and part volume (V).

To perform a comparative analysis between each specimen, a reference Parameter ($P_{ref}$) can be defined and compared against the parameter (P) at hand. To compare one geometry with another, for instance, one of the geometries can be established as the reference, then a deviation can be calculated for the others. The same can be done to compare experimental and simulated EA/SEA, by setting the experimental data as the $P_{ref}$. The percent deviation ($D_{\%}$) is then calculated according to Equation 3.4.

$$D_{\%} = \frac{P - P_{\text{ref}}}{P_{\text{ref}}} \times 100\% \tag{3.4}$$

# Chapter 4

# RESULTS AND DISCUSSION

## 4.1 Experimental Findings

### 4.1.1 Experimental Force–Displacement Curves

As mentioned in Section 3.2.2, a mean curve was obtained from the three resulting force–displacement curves for each geometry, and the mean results for each pattern are shown in Figure 4.1. From the aggregated plot of all curves, it's visible that the LS present a bending-dominated dominated behavior, with the three distinguishable characteristic stages: elastic, near-plateau and densification (Figure 4.2). This is the expected result from the data available in the literature (Ashby, 2006; Zeng et al., 2021; Li et al., 2023) and presented in Chapter 2.

A notable characteristic observed in the plateau region is the deviation from an ideal constant stress state. Instead of an absolute plateau, several geometries – such as the Circle (Figure 4.1a), Hexagon (Figure 4.1c), Triangle (Figure 4.1e), and Wavy (Figure 4.1f) patterns – exhibit a gradual, linear increase in force after the initial linear stage. A similar response was reported by Zhou et al. (2023) in the study of polymeric lattice structures, where the authors attributed this rising stress to the bending of struts under compression. Following this stage, the onset of densification is distinguishable by a rapid increase in stiffness near the end of the curves, occurring at approximately 17 mm for most cases.

Analyzing the patterns individually reveals distinct behaviors governed by topology. Most notably, the Circle, Hexagon, and Wavy patterns display remarkably similar f–d curves (Figures 4.1a, 4.1c, and 4.1f). In these cases, the linear elastic stage is followed by progressive hardening until a peak load is reached. Subsequently, a softening behavior is observed – likely attributable to high plastic strain accumulation in the inner struts – before transitioning into the steep force increase characteristic of densification.

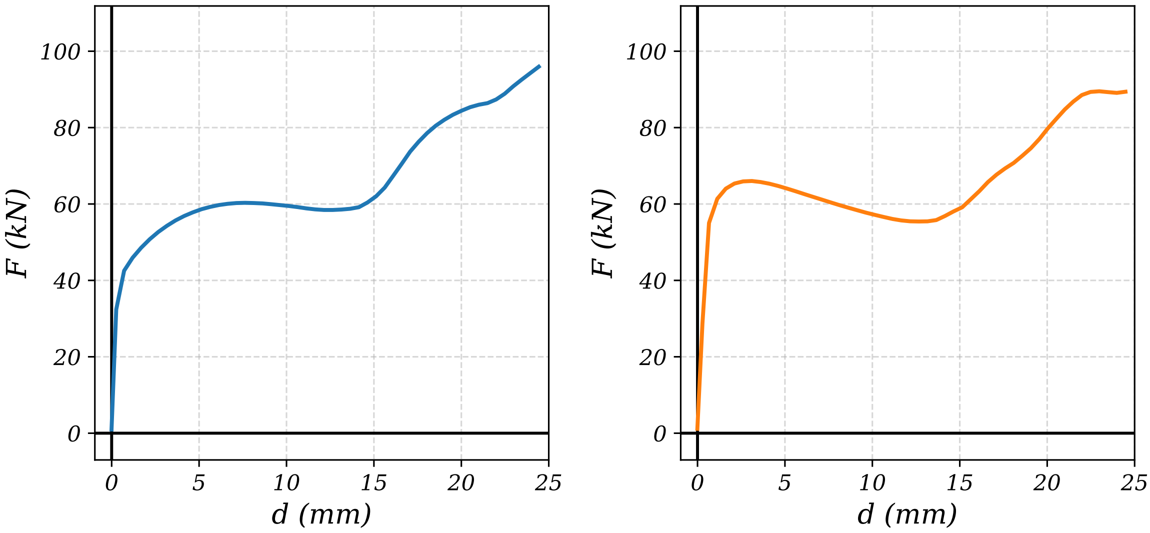

(**a**) **Pattern:** Circle

(**b**) **Pattern:** Diamond

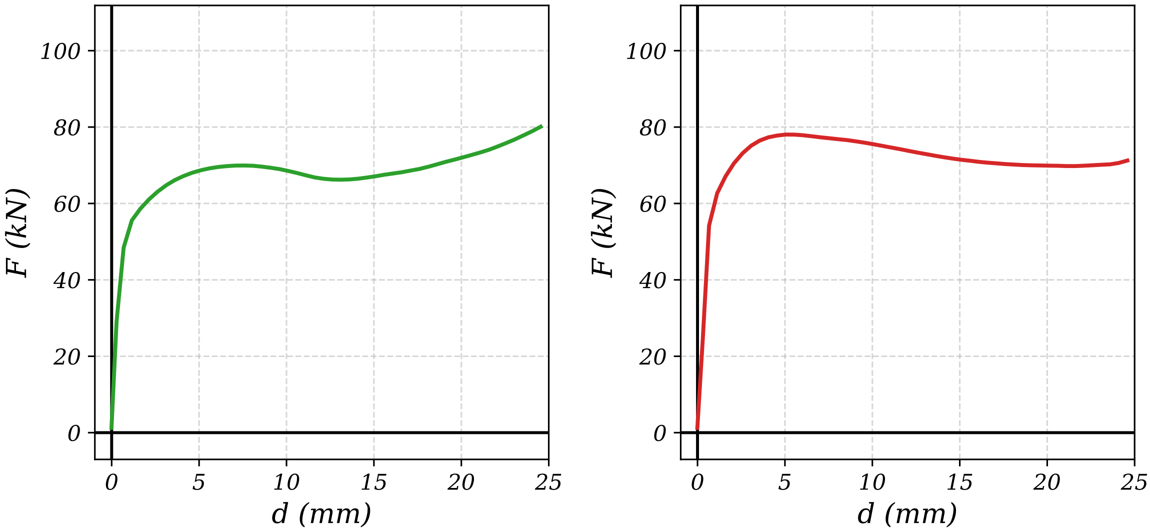

(**c**) **Pattern:** Hexagon

(**d**) **Pattern:** Square

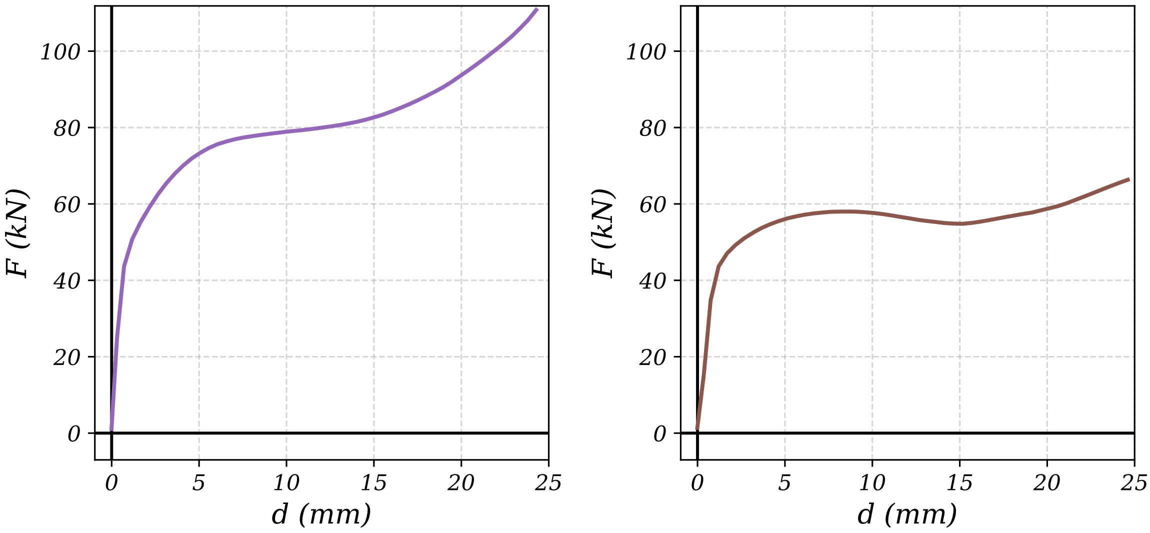

(**e**) **Pattern:** Triangle

(**f**) **Pattern:** Wavy

Figure 4.1: All experimental force–displacement curves for the six lattice patterns.

The Diamond (Figure 4.1b) and Triangle (Figure 4.1e) patterns presented unique responses. The Diamond curve shows a brief force increase after the elastic limit, followed by pronounced softening. This behavior, more accentuated than in other geometries, suggests intense plastic deformation of the inner struts facilitated by the absence of global buckling. Conversely, the Triangle pattern exhibited the most stable behavior: a linear stage followed by a monotonic force increase and a quasi-plateau region between 5 mm and 15 mm, prior to densification.

Finally, the Square pattern (Figure 4.1d) presented the most dissimilar shape, characterized by a linear stage, a gradual force increase, and subsequent softening. This distinct profile is likely a consequence of the structure's premature global buckling, which prevented the stable, layer-by-layer collapse observed in other topologies.

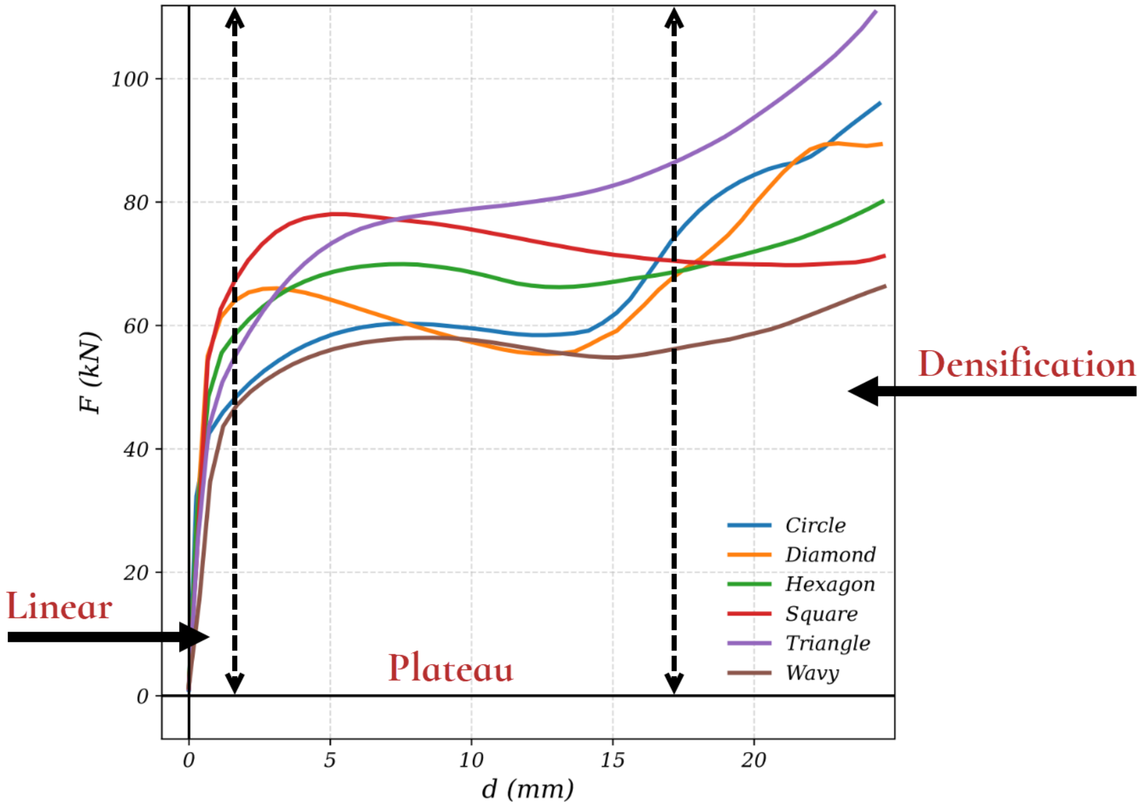

Figure 4.2: Three stage behavior (linear; plateau; densification) highlighted in the aggregated plot for all experimental force–displacement results.

### 4.1.2 Experimental energy absorption

According to the methodology presented in Section 3.3, the experimental Energy Absorption and Specific Energy Absorption values were calculated for each specimen. The results are presented in Table 4.1, where the displacement was truncated to the corresponding value for each pattern simulation. Additionally, a deviation is also presented by arbitrarily establishing the Circle pattern as a baseline, then computing each geometry's shift in comparison for the Energy Absorption (EA) and Specific Energy Absorption (SEA).

| **Pattern** | *d*<br>[mm] | EA<br>[J] | SEA<br>[kJ/kg] | $D_{\%}$–C<br>[%] |
|---|---|---|---|---|
| Circle | 17.00 | 974 | 10.89 | 0.00 / 0.00 |
| Diamond | 17.00 | 1010 | 10.29 | +3.69 / -5.51 |
| Hexagon | 13.25 | 855 | 8.97 | -12.23 / -17.67 |
| Square | 16.73 | 1205 | 16.32 | +23.68 / +49.83 |
| Triangle | 17.00 | 1240 | 13.00 | +27.41 / +19.37 |
| Wavy | 17.00 | 905 | 9.41 | -7.09 / -13.60 |

Table 4.1: Experimental energy and specific energy absorbed for each pattern, including deviation from the Circle baseline. Values in the deviation column are reported as (total / specific).

For the EA, the highest value was obtained by the Triangle pattern – but it remained so close to the Square pattern (about 3% higher) that the two can be considered equivalent in this respect, especially since the Square data was truncated at 16.73 mm to match the simulation's end time. The Square–Triangle are then followed by the Diamond–Circle, wavy and Hexagon patterns (Figure 4.3**a**). However, the Hexagon pattern was truncated very early – at 13.25 mm – due to the simulation diverging at the onset of densification.

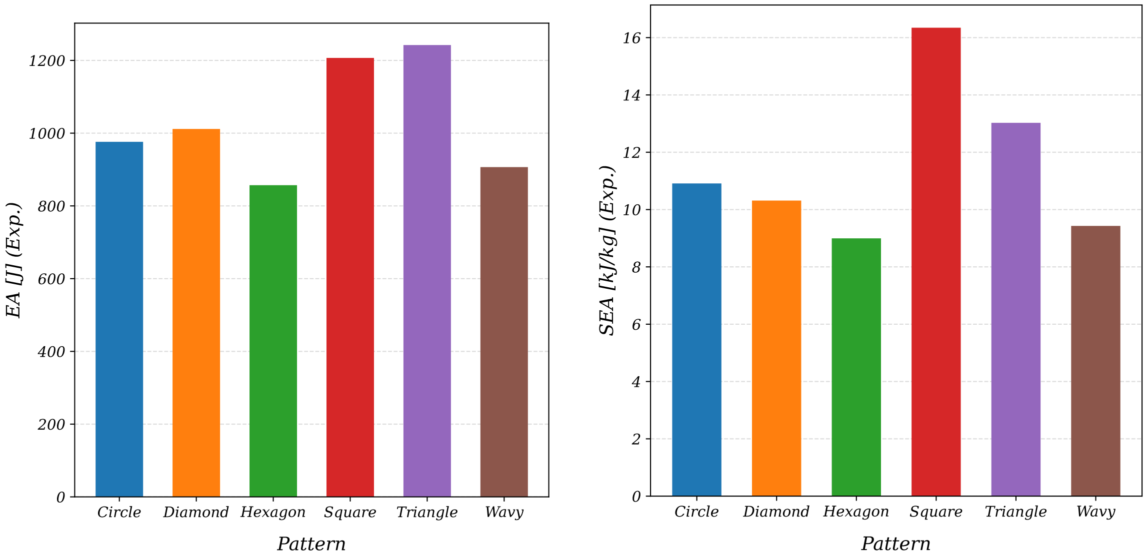

(**a**) Energy Absorption (EA).

(**b**) Specific Energy Absorption (SEA).

Figure 4.3: Comparison between the experimental Energy Absorption (EA) and Specific Energy Absorption (SEA) for all lattice patterns.

In terms of SEA, the Square pattern showed itself as the most resilient one, with a 49.83% specific energy absorption increase in comparison to the Circle pattern (Figure 4.3**b**). It's followed by the Triangle, Circle–Diamond, Wavy and Hexagon. The two key differences when looking at energy absorption then are: that the Square pattern outperformed the other patterns by a much larger margin in comparison to total energy; and that the Circle seems to outperform the Diamond pattern when looking at specific energy, whereas the opposite happens for total energy (although the values are also too close – within a ≈ 5% margin – for a certain evaluation). The specific reasons of each pattern's performance will be explored in more detail in Section 4.3.3.

### 4.1.3 Observed Deformation and Failure Modes

After each experiment was concluded, a registry was made of the post-compression state of the specimens. Figure 4.4 shows the post-mortem specimens are presented, where the specific deformation modes are visible.

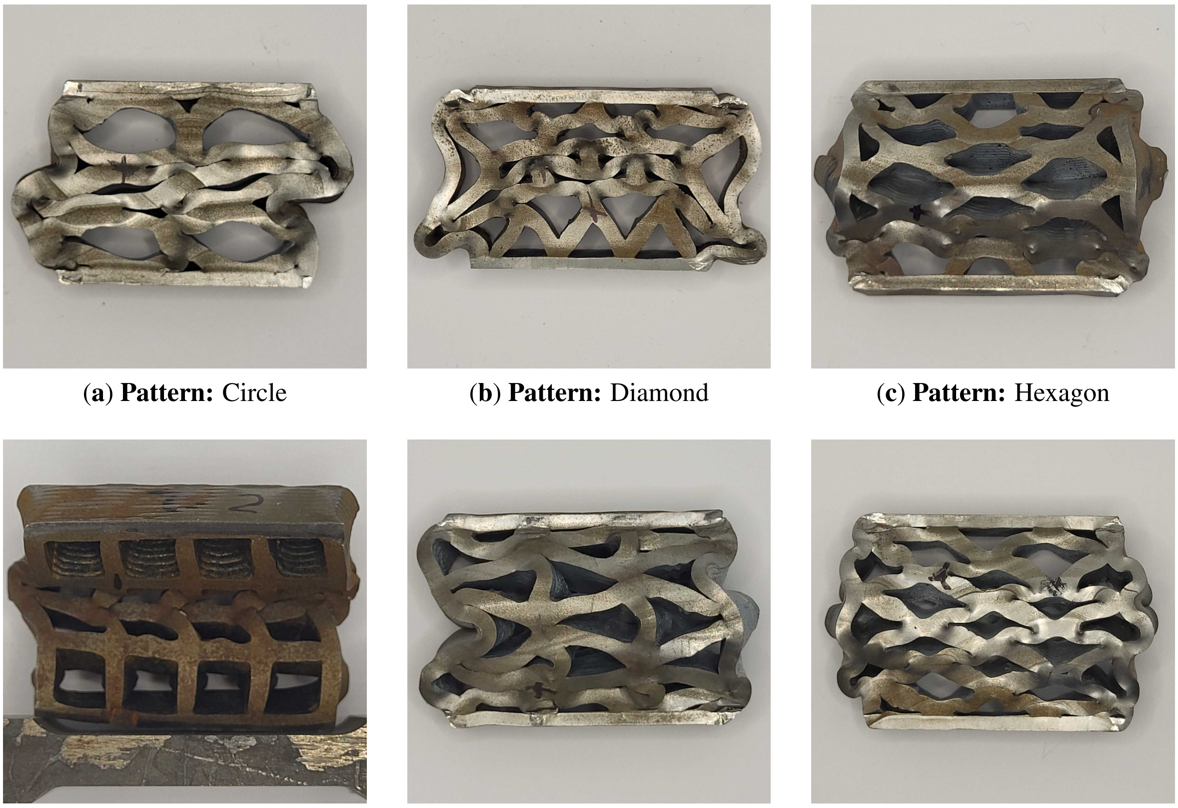

(**a**) **Pattern:** Circle (**b**) **Pattern:** Diamond (**c**) **Pattern:** Hexagon

(**d**) **Pattern:** Square (**e**) **Pattern:** Triangle (**f**) **Pattern:** Wavy

Figure 4.4: Post-mortem view of the lattice structure specimens after compression for each pattern. Provided by INEGI.

The first notable characteristic present in almost all geometries except for all the specimens fabricated using the Diamond pattern, and two of the specimens using the Circle pattern – is that the specimens presented a high tendency to buckling in the out-of-plane direction. This might be attributed to the slender shape of the samples – which make them prone to buckling – as well as the possibility of the guides being misaligned.

However, even if such behavior is clearly present during the test, most geometries only started showing a high tendency to buckle after the densification stage – where the loading distribution becomes uneven due to the high local buckling and bending of the individual struts. One exception was the Square pattern, which started to globally buckle very early into the experiment, as illustrated by Figure 4.5. This in turn might be attributed to the Square's inner struts tendency to bend instead of buckle, which produces a steep increase in the plastic deformation and – consequently – on the local stress values, which causes structural instability and facilitates the geometry to globally buckle.

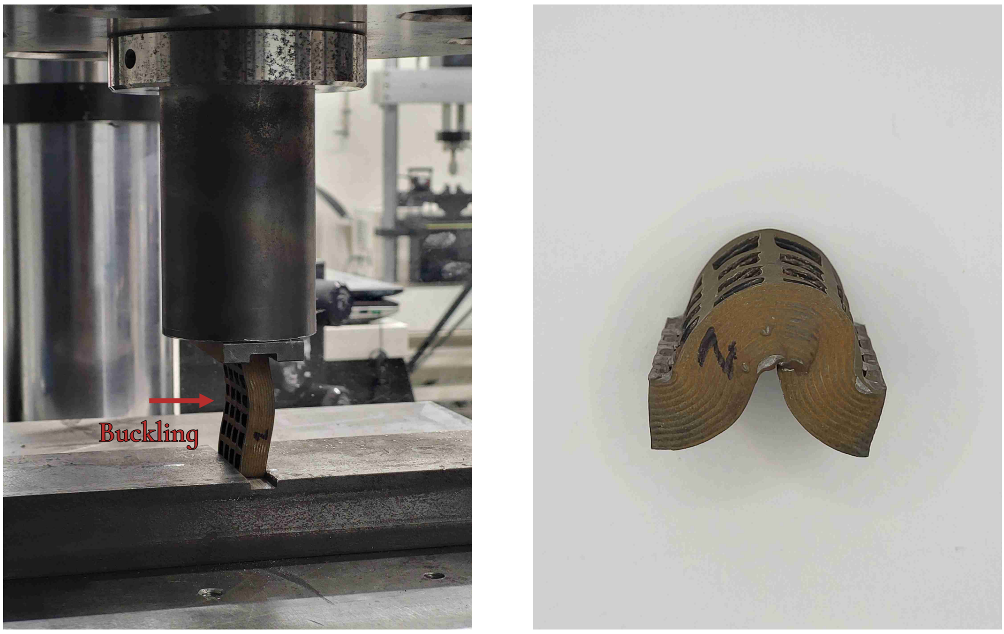

(**a**) Square pattern – global buckling.

(**b**) Square pattern – post-mortem curvature.

Figure 4.5: Global buckling behavior of the Square lattice. The figure presents the in-test deformation (a) and the post-mortem shape (b). Adapted from INEGI.

In terms of local strut behavior, most geometries showed a combination of buckling and bending. However, some geometries seem more prone to bending – e.g. the Square geometry's deformation seems to be mostly governed by strut bending and global buckling – and some to buckling – such as the Triangle and Diamond ones, which presented a high buckling of the some individual struts (Figure 4.6).

(**a**) Diamond pattern local buckling in several struts.

(**b**) Square pattern deformation mainly governed by strut bending.

(**c**) Triangle pattern pronounced local buckling, especially near boundaries.

Figure 4.6: Experimental strut buckling and bending observed in selected lattice geometries. Adapted from INEGI.

Two geometries also showed the commonly observed shear bands highlighted in Section 2.1.2 and extensively reported in literature – e.g. (Wu et al., 2023; Sharma and Hiremath, 2023; Zhou et al., 2023) – where a diagonal line is clearly observable in the post-failure deformed specimens (Figure 4.7). This observed behavior is then aligned with previous studies and highlights the need to accurately manufacture components to show the desirable layer-by-layer progressive structure collapse instead of having a preferential and diagonal load path.

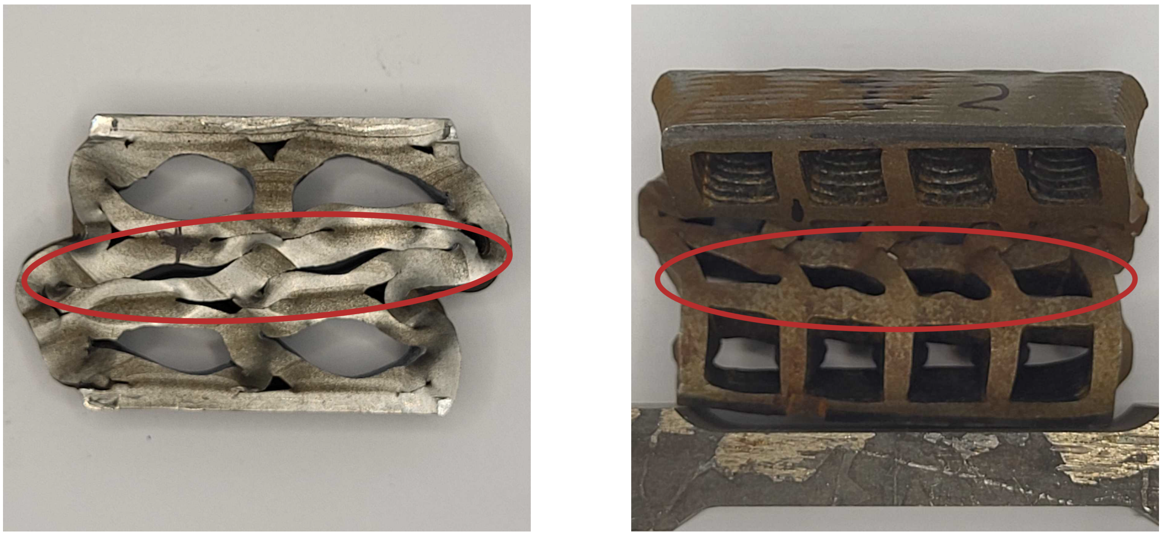

(**a**) Circle pattern visible diagonal shear band.

(**b**) Square pattern shear band crossing several cell rows.

Figure 4.7: Shear bands observed in the post-failure specimens. Adapted from INEGI.

## 4.2 Numerical Simulation Results

### 4.2.1 Simulated Force–Displacement Curves

The force–displacement curves provided by the history output using Abaqus/CAE were plotted together and are presented in Figure 4.8. The figure shows the force values for each displacement point in the simulation, and the choice of using the asterisk marker highlights the difference in timestep throughout the studies. The decrease in timestep can be spotted by noting a denser cloud of points as opposed to a sparse and regular one, which gives a hint to which simulations were more stable – e.g., the Triangle simulation was especially stable and the timestep was fairly constant, as opposed to the Square simulation, which required a drastic reduction in the timestep after the peak force value (likely due to the high plastic deformation of the inner struts).

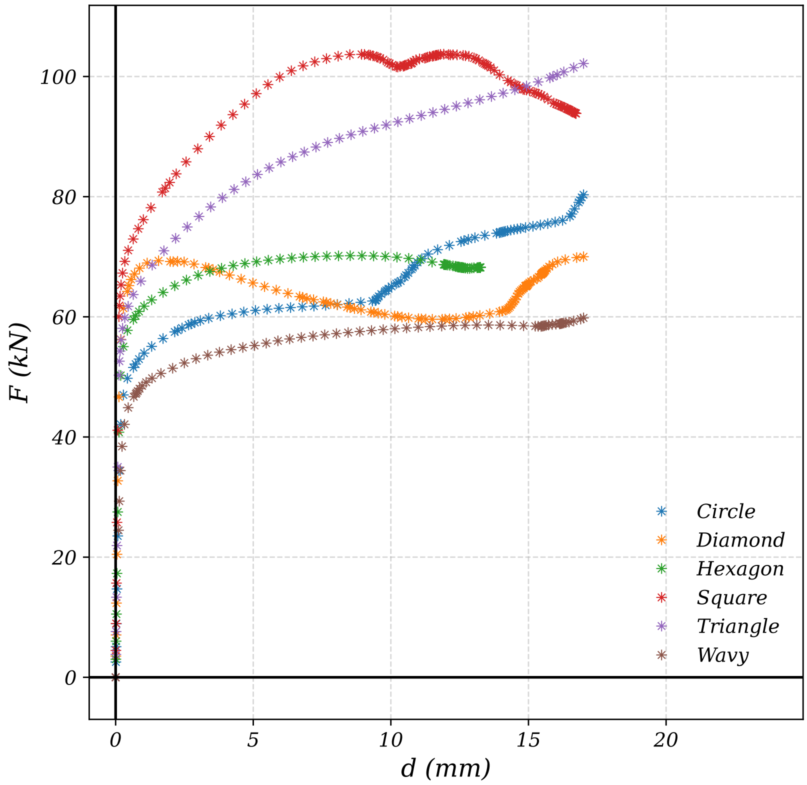

Figure 4.8: All simulated force–displacement curves for the six lattice patterns.

Similarly to the experimental results, they've presented the three stage behavior, visible when plotting the curves. They also agreed with experimental data on the gradual force increase in the plateau stage, before reaching densification. As previously mentioned, the simulations were truncated at 17mm – where densification started to become more apparent – because of the increasing complexity of the contact interactions. The complexity involved can be further noticed by looking at the number of subsequent timesteps for the same displacement variation before and after the self-contacts start taking place (indicating densification). By looking at Figure 4.8, the point clouds start becoming denser at the onset of densification, indicating a struggle of the solver to achieve convergence and the need to subsequently reduce the time increments (up to the minimum allowed value).

Two geometries didn't complete until the total displacement, the Square and the Hexagon. While the Square diverged at 16.73 mm – which didn't influence the analysis since it was too close to the end time for all simulations (17 mm) – the Hexagon lattice only ran until about 13mm, as can be observed by looking at its particular force–displacement simulated response, where the increment get's smaller near the end and leads to a value smaller than the allowable threshold. It's not trivial to pinpoint what was the exact issue that lead to the simulation diverging so early for the Hexagon pattern specifically, but a few hypothesis might be raised. The first one is that the Hexagonal pattern showed a very high stiffness, which prematurely lead to a stress increase and made the simulation unstable. On the other hand, densification starts suddenly for this structure, and the contact area between the collapsing struts becomes very large even for the first interaction, which increases the contact complexity, as demonstrated by Figure 4.9. Finally, the middle node of the cells, produced by using a second order mesh, also increases the number of contact interactions and makes the solving of the equations unstable.

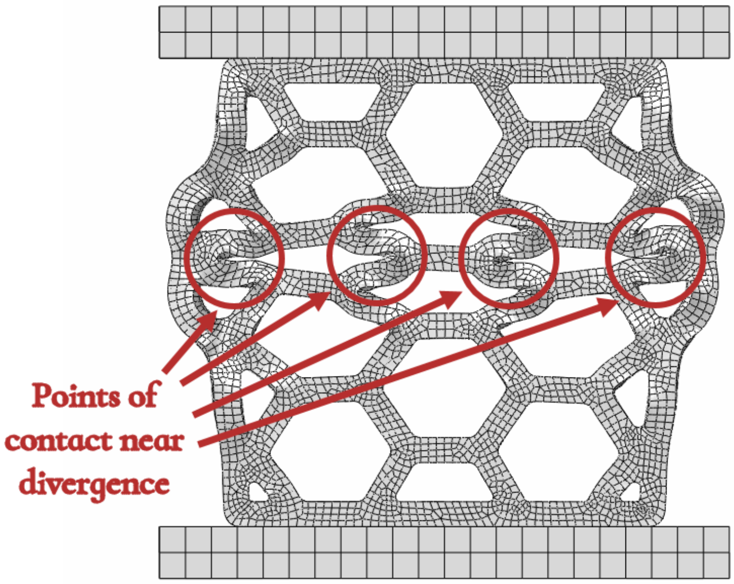

Figure 4.9: Hexagonal lattice during the numerical compression test, highlighting the regions where contact between opposite struts becomes dominant near the end of the simulation.

### 4.2.2 Simulated energy absorption

Table 4.2 shows the obtained simulated data in terms of EA and SEA. Looking at the EA, the highest value was obtained for the Square pattern by a very large margin of 10.9% in comparison to next best performer (the Triangle pattern – see Figure 4.10**a**). This difference from the experimental data might be attributable (as in the curve comparative analysis) to the global buckling behavior not appearing in the simulation, as well as the struts locally bending, since bending is well-known for it's energy absorption capabilities.

| **Pattern** | $d$ [mm] | EA [J] | SEA [kJ/kg] | $D_{\%}$–Circle [%] |
|---|---|---|---|---|
| Circle | 17.00 | 1101 | 12.31 | 0.00 / 0.00 |
| Diamond | 17.00 | 1085 | 11.06 | -1.45 / -10.16 |
| Hexagon | 13.25 | 893 | 9.36 | -18.92 / -23.94 |
| Square | 16.73 | 1600 | 21.68 | +45.32 / +76.14 |
| Triangle | 17.00 | 1480 | 15.52 | +34.42 / +26.10 |
| Wavy | 17.00 | 946 | 9.83 | -14.08 / -20.17 |

Table 4.2: Simulated energy and specific energy absorbed for each pattern, including deviation from the Circle baseline. Values in the deviation column are reported as (total / specific).

In terms of SEA, the Square pattern once again outperformed the others by an even larger margin, with a 76.14% specific energy absorption increase in comparison to the Circle pattern (Figure 4.10**b**), which indicates a high volumetric efficiency in terms of energy absorption. It's followed by the Triangle, Circle, Diamond, Wavy and Hexagon. The simulation specific energy showed a highly stepped behavior between the samples, i.e., most patterns presented very different performance levels and could be placed on a 1–6 list from best to worst performer (excluding of course the Hexagon pattern due to the data truncation mentioned earlier).

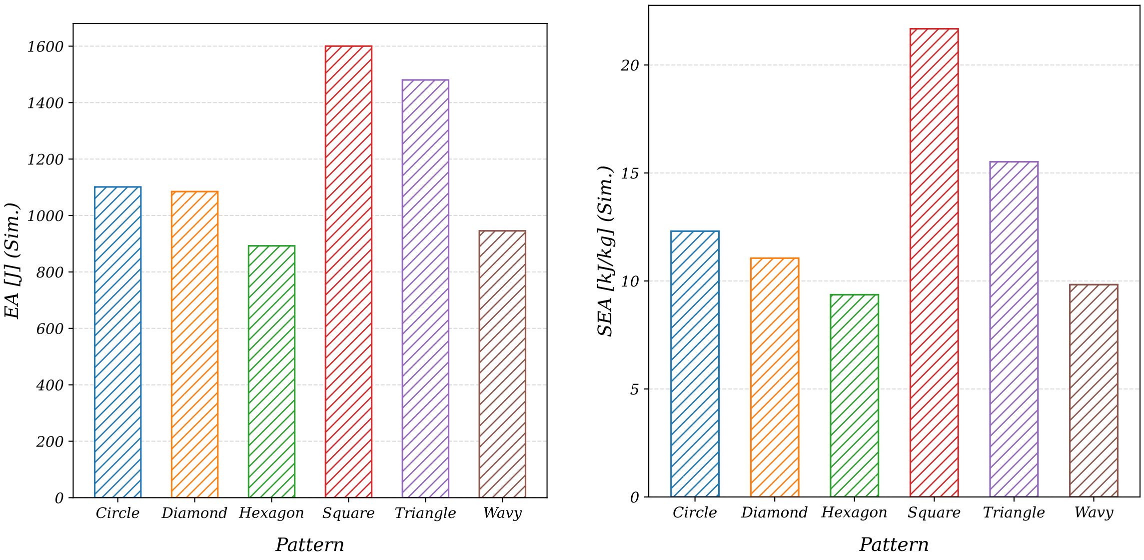

(**a**) Energy Absorption (EA).

(**b**) Specific Energy Absorption (SEA).

Figure 4.10: Simulated Energy Absorption (EA) and Specific Energy Absorption (SEA) for all lattice patterns.

### 4.2.3 Von Mises Stress, PEEQ and deformed shapes

Figures 4.11–4.12 show the Von Mises Stress and PEEQ contour plots for each structure, plotted against the deformed geometries. In an initial overall assessment, it's notable that the deformed shapes resemble the real-life samples somewhat closely, especially when it comes to strut buckling and bending. On the other hand, no simulation predicted the global buckling of the structures, which is in line with the mesh being symmetric across the thickness and the simulation operating under idealized conditions in terms of material isotropy and specimen alignment.

By looking at them individually, some noteworthy patterns also begin to emerge. The Circle and Diamond patterns (Figures 4.11a–4.11b) were especially stable and showed the desired layer-by-layer collapse, as opposed to a shear band, which can be noticed by the highly symmetric stress distribution. Looking at the PEEQ for these structures, the distribution is also symmetric, with a high deformation level appearing at the struts roots and mid sections.

Even if the Hexagon LS didn't complete until the end, it also showed a visually symmetric behavior for both fields (Figures 4.11c–4.12c). This can be further noticed by comparing it to the conceptually similar Wavy pattern (Figures 4.11f–4.12f), where the stress distribution was not symmetric and clearly showed a preferential and diagonal path.

The Triangle and Square patterns both showed an unsymmetrical behavior. For the Triangle, this was expected since the geometry itself is not symmetric in-plane. Most of the loading seems to be supported by the vertical struts instead of the diagonal ones, and the external struts showed a buckling behavior, where PEEQ was higher at the strut's middle. The internal ones showed bending, with the higher PEEQ appearing at the connections (Figure 4.11e). The Square lattice also presented a behavior where the load was being carried by the vertical as opposed to the horizontal struts (Figures 4.11d–4.12d), and the response showed a high tendency to the formation of two shear bands: one at the second layer from top to bottom and one at the second layer from bottom to top.

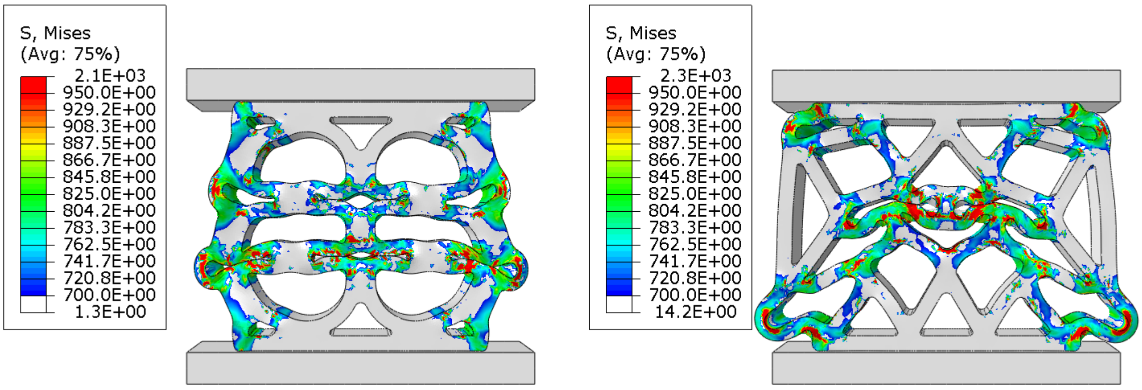

(**a**) **Pattern:** Circle (**b**) **Pattern:** Diamond

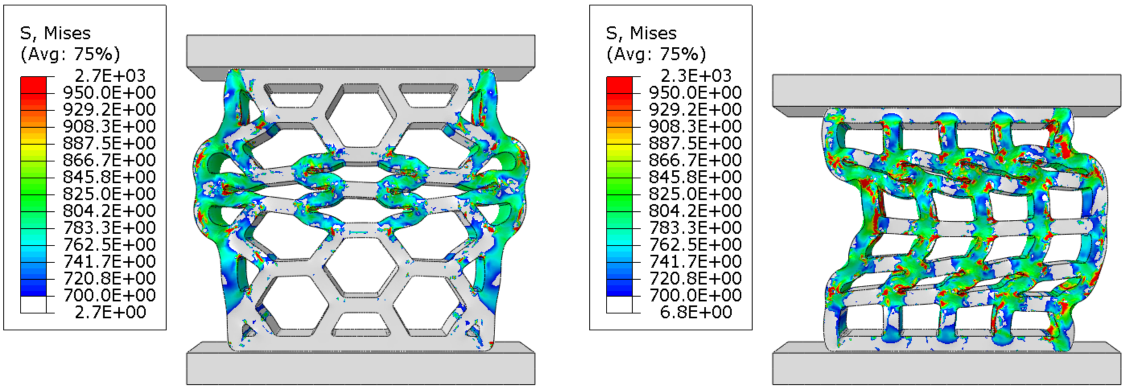

(**c**) **Pattern:** Hexagon (**d**) **Pattern:** Square

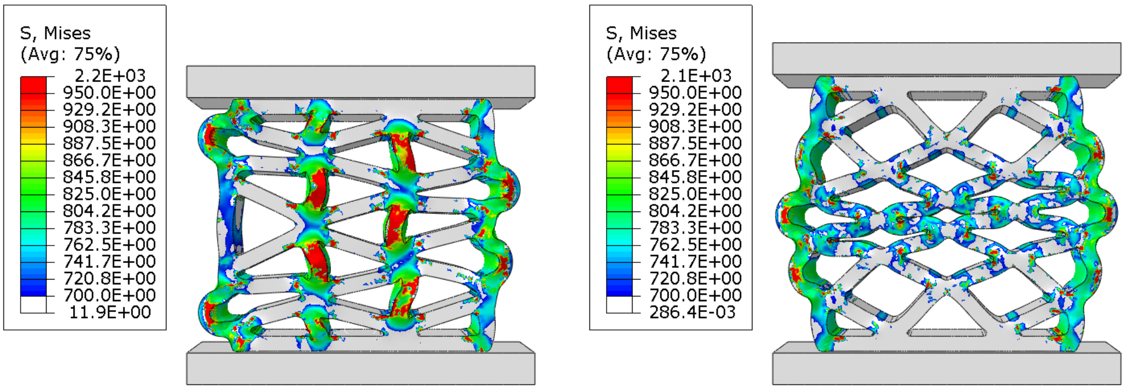

(**e**) **Pattern:** Triangle (**f**) **Pattern:** Wavy

Figure 4.11: Von Mises stress distribution for each lattice pattern at the end of compression. Values below 700 MPa are plotted in white and values above 950 MPa are saturated in red.

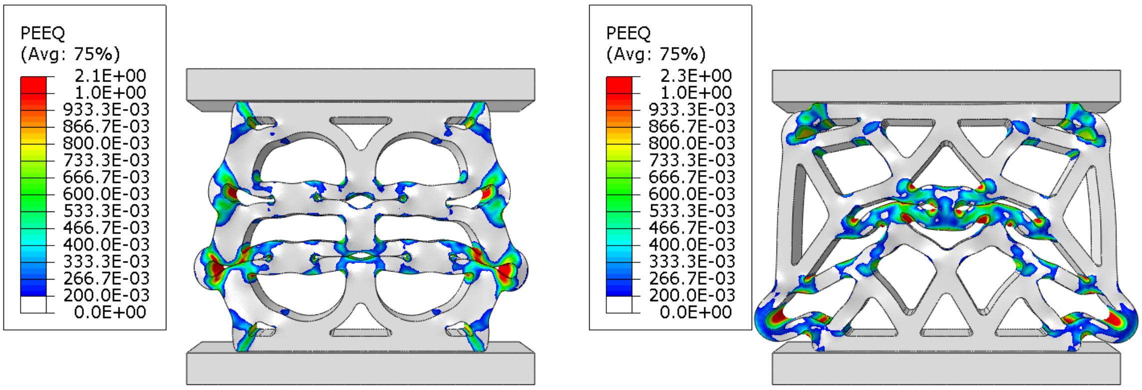

(**a**) **Pattern:** Circle

(**b**) **Pattern:** Diamond

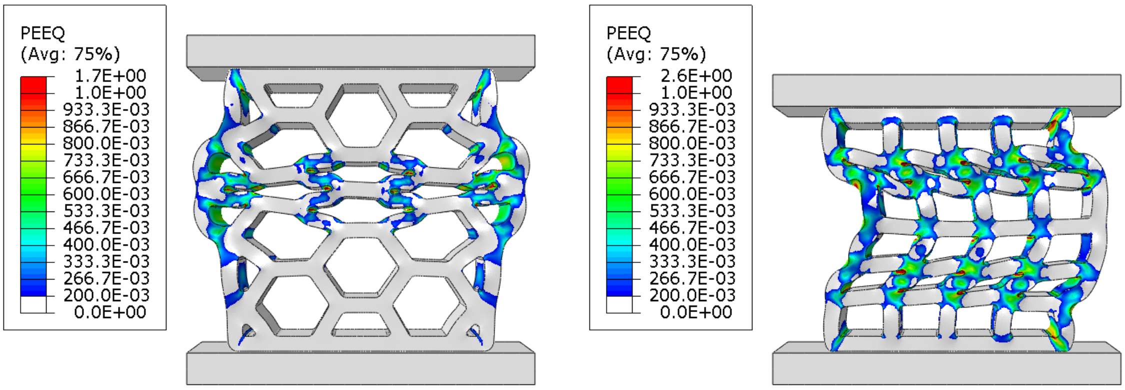

(**c**) **Pattern:** Hexagon

(**d**) **Pattern:** Square

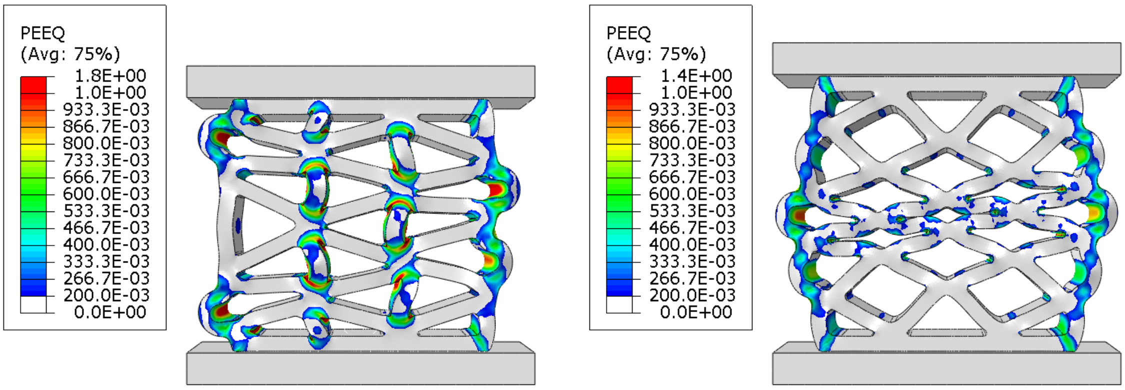

(**e**) **Pattern:** Triangle

(**f**) **Pattern:** Wavy

Figure 4.12: Equivalent plastic strain (PEEQ) distribution for all lattice patterns. A post-processing filter was applied to show values between **0.2** and **1.0**. Values below **0.2** were rendered in white, and values above **1.0** were rendered in red.

### 4.2.4 Computational Cost

Upon completion of the numerical simulations, a comparative analysis of the computational cost was performed by retrieving the Wall Clock Time for each geometry, as detailed in Table 4.3. It is worth noting that the simulation time is inversely proportional to the model's stability: severe instabilities or excessive mesh distortions force the solver to reduce the time increment to try and achieve a successful iteration. This behavior can be visualized in Figure 4.8, where an increase in the density of plotted points indicates a reduction in the time step.

| **Pattern** | **Wall Clock Time** [s] |
|---|---|
| Circle | 5016 |
| Diamond | 9146 |
| Hexagon | 6664 |
| Square | 15444 |
| Triangle | 2990 |
| Wavy | 3661 |

Table 4.3: Computational cost for each pattern simulation.

From this perspective, the Triangle topology exhibited the lowest computational cost (2990 s), which is corroborated by the uniformity of the time increments observed in the plots. Next are the Wavy (3661 s) and Circle (5016 s) patterns, which demonstrated good structural and numerical stability throughout the compression process. The Hexagon pattern (6664 s) remained stable for most of the regime; however, the numerical divergence occurring near 13.25 mm required successive reductions in the time step, increasing the total cost despite the shorter displacement achieved.

Higher costs were observed in geometries with more complex contact interactions or unstable failure modes. The Diamond pattern (9146 s), despite its progressive and stable collapse, suffered a strong computational penalty near 15 mm, at which point densification intensifies the contact between struts. Finally, the Square topology demanded the highest computational effort (15444 s). The formation of a shear band after the stress peak caused large geometric distortions in the mesh, compromising numerical stability. Notably, even though it failed prematurely ($d \approx 16.73$ mm), the Square pattern simulation consumed considerably more resources than the others due to the need to process the simulation with extremely reduced time increments.

## 4.3 Validation of the Numerical Model Against Experimental Data

### 4.3.1 Force–displacement curves for the Lattice Geometries

Once the numerical studies are completed, the next step is to plot the experimental results against the numerical ones for a full comparison. This is presented for each pattern individually in Figure 4.13, and for all curves plotted together in Figure 4.14.

The curves for some patterns showed good agreement, while others remained lacking. The first notable difference between the the experimental and numerical results is related to LS stiffness, since the experimental curves were considerably softer in comparison to the simulated ones. While studying 2D circular lattices, Ha et al. (2022) noted a similar pattern where a shift occurred at the peak point of each curve (at the end of the linear region) by comparing simulation and experimental data, and the authors attributed it to them not adding a damage formulation to the model (since it would soften the components). The numerical setup developed in this dissertation then suffers from the same sort of inaccuracy.

However, beyond the yield limit for each LS, the curves for the Diamond, Hexagon and Wavy patterns showed a good agreement between experiment and simulation – with them almost overlapping for the entirety of the evaluated displacement (Figures 4.13b, 4.13c and 4.13f). The observed behavior was also similar in terms of the increase/decrease tendencies, with the Diamond curve, for instance, both experimentally and numerically starting with the linear increase in force, followed by a monotonic and short increase until a peak force and by a subsequent softening. The force presents a steep increase again when densification starts. The Hexagon pattern shows a similar pattern up to the densification stage (where the simulation diverges) and the Wavy pattern simulation presents a linearly increasing force up to densification, while the experiment shows an increase/decrease behavior instead. The difference might be attributable to the global buckling tendency in the experiment for the Wavy pattern.

The curve for the Circle pattern also showed some agreement – although the difference became more pronounced after 10mm. This change in behavior is likely attributable to the real specimen showing both a global buckling behavior, as well as a preferential shear band where deformation occurred, which was not captured by the simulation. The simulated Triangle pattern curve also showed a similar shape to its experimental counterpart, although shifted upwards. One notable difference between the simulation and the experiment was the not-capturing of a the buckling tendency from the large mid-left strut (see Figure 4.12e), which was likely the driver of the higher softening showed by the experimental curve.

The pattern which presented the higher difference in Simulation–Experimental (S–E) shape was the Square, which gives insights on the potential difference observed in the other curves. Since the Square pattern specimen globally buckle at the very beginning of the experiment, it’s obtained real-life curve was much softer in comparison to the simulation one. In the simulation, buckling didn’t happen neither globally nor locally (at the strut level), indicating a higher energy absorption capability in the form of strut bending.

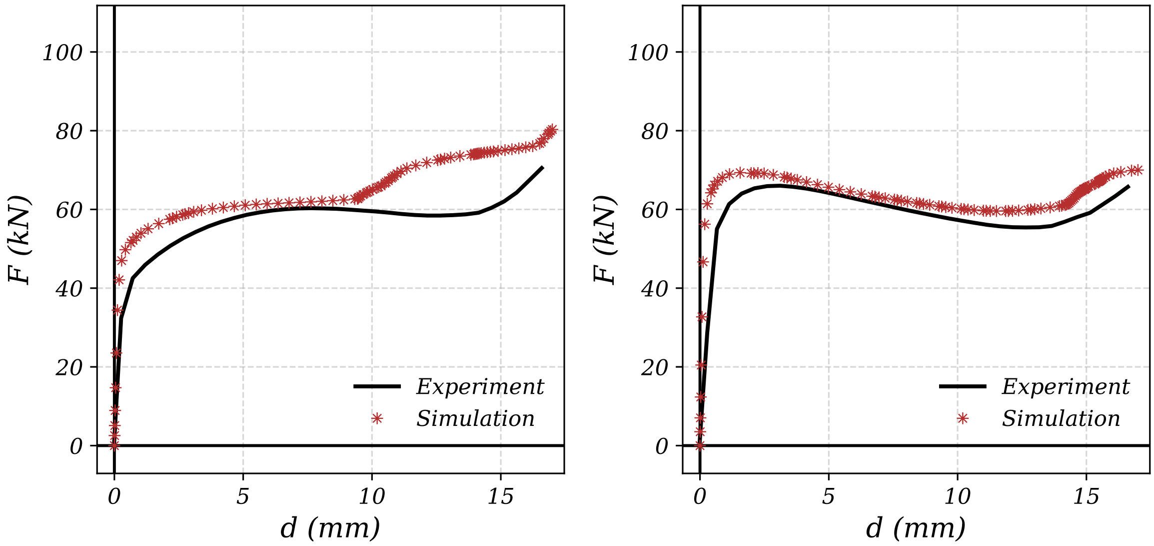

(**a**) **Pattern:** Circle (**b**) **Pattern:** Diamond

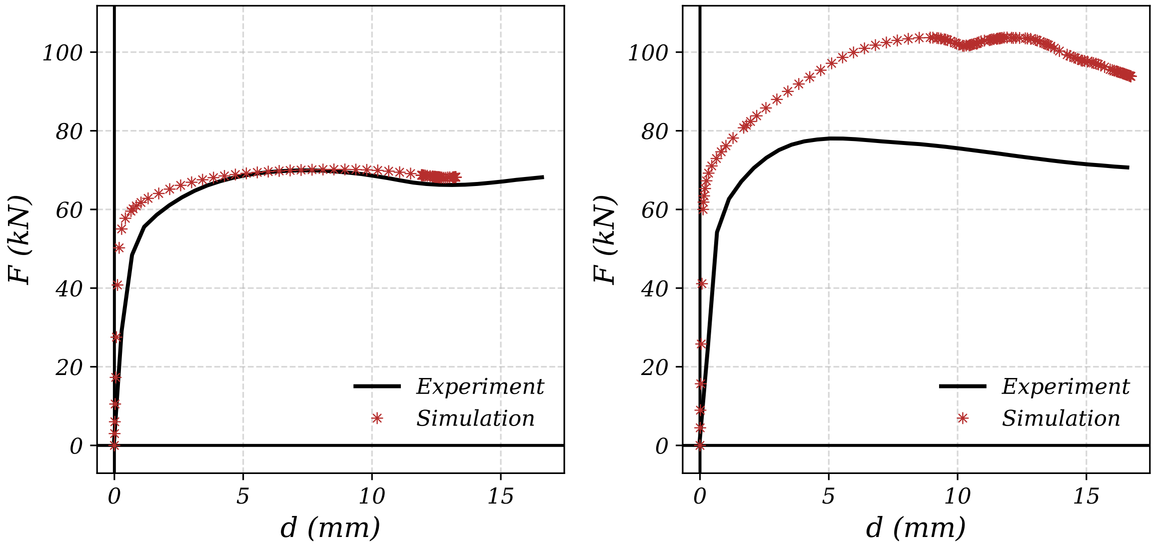

(**c**) **Pattern:** Hexagon (**d**) **Pattern:** Square

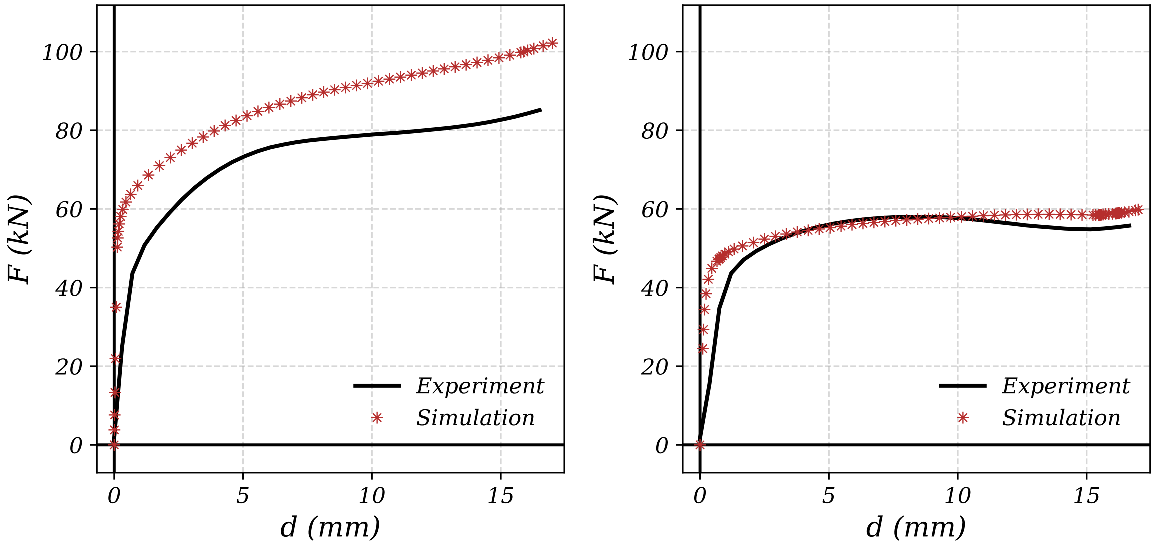

(**e**) **Pattern:** Triangle (**f**) **Pattern:** Wavy

Figure 4.13: Comparison between experimental and simulated force–displacement curves for each lattice pattern.

When looking at all curves plotted together (Figure 4.14), it's possible to compare each pattern's strength by observing the curves y-shift , i.e., the force value at the beginning of the plateau region. Experimentally, the curve most downwards shifted was the one from the Wavy pattern, followed by Circle, Triangle–Hexagon, Diamond and Square. For the simulated curves, a the following pattern appears: Wavy, Circle, Hexagon, Diamond–Triangle, Square. The two patterns are then in agreement for most structures, with only the Triangle shaped LS being placed higher in terms of y-shift because of the already mentioned higher force response predicted by the simulation.

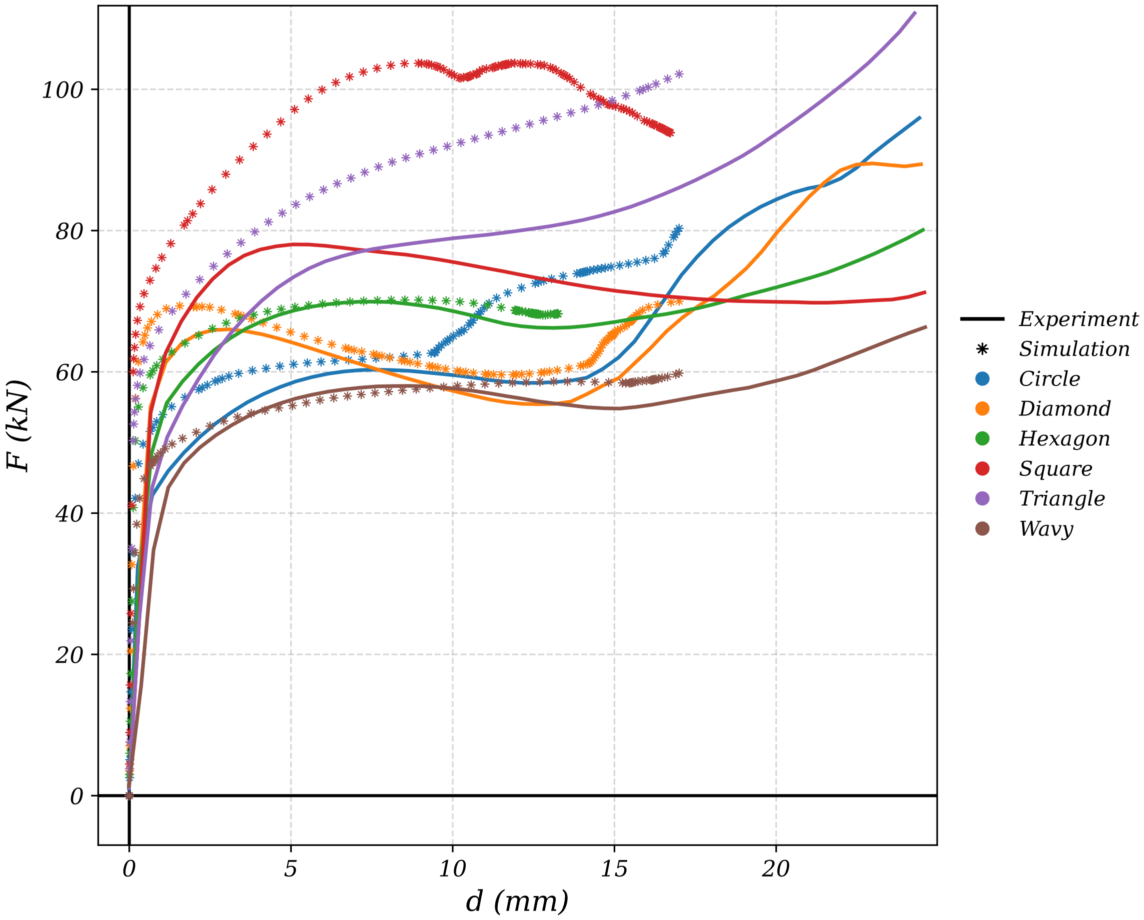

Figure 4.14: All (experimental/simulated) force–displacement curves for the six lattice patterns.

## 4.3.2 Quantitative comparison of energy absorption

From the data exposed in Sections 4.1.2–4.2.2, a comparison can be performed by joining the experimental and simulation data in terms of EA and SEA, then observing the deviation between the real and numeric values. Table 4.4 displays the quantities obtained for each pattern, as well as the deviation of the simulations from the experimental ($D_{\%}$ (S–E)) data for each in terms of EA, and Table 4.5 does the same for SEA.

| **Pattern** | $d$ [mm] | $EA_{exp}$ [J] | $EA_{sim}$ [J] | $D_{\%exp}$–C [%] | $D_{\%sim}$–C [%] | $D_{\%}$ (S–E) [%] |
|---|---|---|---|---|---|---|
| Circle | 17.00 | 974 | 1101 | 0.00 | 0.00 | +13.06 |
| Diamond | 17.00 | 1010 | 1085 | +3.69 | -1.45 | +7.43 |
| Hexagon | 13.25 | 855 | 893 | -12.23 | -18.92 | +4.44 |
| Square | 16.73 | 1205 | 1600 | +23.68 | +45.32 | +32.81 |
| Triangle | 17.00 | 1240 | 1480 | +27.41 | +34.42 | +19.35 |
| Wavy | 17.00 | 905 | 946 | -7.09 | -14.08 | +4.53 |

Table 4.4: Comparison between experimental and simulated **Energy Absorption (EA)**. Columns include: experimental EA ($EA_{exp}$), simulated EA ($EA_{sim}$), experimental deviation from Circle ($D_{\%exp}$–C), simulated deviation from Circle ($D_{\%sim}$–C), and the simulation error relative to experiment ($D_{\%}$ (S–E)).

| **Pattern** | $d$ [mm] | $SEA_{exp}$ [kJ/kg] | $SEA_{sim}$ [kJ/kg] | $D_{\%exp}$–C [%] | $D_{\%sim}$–C [%] | $D_{\%}$ (S–E) [%] |
|---|---|---|---|---|---|---|
| Circle | 17.00 | 10.89 | 12.31 | 0.00 | 0.00 | +13.08 |
| Diamond | 17.00 | 10.29 | 11.06 | -5.51 | -10.16 | +7.48 |
| Hexagon | 13.25 | 8.97 | 9.36 | -17.67 | -23.94 | +4.35 |
| Square | 16.73 | 16.32 | 21.68 | +49.83 | +76.14 | +32.93 |
| Triangle | 17.00 | 13.00 | 15.52 | +19.37 | +26.10 | +19.38 |
| Wavy | 17.00 | 9.41 | 9.83 | -13.60 | -20.17 | +4.46 |

Table 4.5: Comparison between experimental and simulated **Specific Energy Absorption (SEA)**. Columns include: experimental SEA ($SEA_{exp}$), simulated SEA ($SEA_{sim}$), experimental deviation from Circle ($D_{\%exp}$–C), simulated deviation from Circle ($D_{\%sim}$–C), and the relative simulation error ($D_{\%}$ (S–E)).

The first insight to be drawn from Tables 4.4–4.5 is that all simulations over predicted the energy absorption for each pattern, which means that all curves presented an upwards force shift. As explained in the previous section, this might be attributable to the non-inclusion of a damage parameter – which would soften the specimens as they approach the fracture limit – as well as to the highly idealized nature of the simulation – e.g. material behavior was considered isotropic, the mesh was highly symmetric etc. However, an overall assessment shows a good experimental-numerical agreement – especially excluding the Square and Triangle patterns, with all other geometries deviating from the simulation by an average of $\approx 7.3\%$. By including the Square and Triangle patterns, the average rises to $\approx 13.6\%$, which can still be considered an acceptable deviation.

From the comparison, it’s also clear that a correlation can be established between the accuracy in representing the deformation modes of the specimens faithfully and the resulting curve with it’s energy absorption capabilities. The Square lattice simulation, for instance, was the most deviant in terms of global behavior since the global buckling wasn’t numerically captured, and it consistently presented the highest deviation from the experimental data.

The same can be said for the Triangle lattice, since a crucial buckling wasn't captured by the simulation. The next specimen with a somewhat high deviation (although well below the other two) was the Circle lattice, which in real life showed a tendency to form a preferential load path which was absent from the simulation. Figure 4.15 shows a comparison between each lattice and their correspondent EA/SEA, while at the same time presenting the results for the respective simulations.

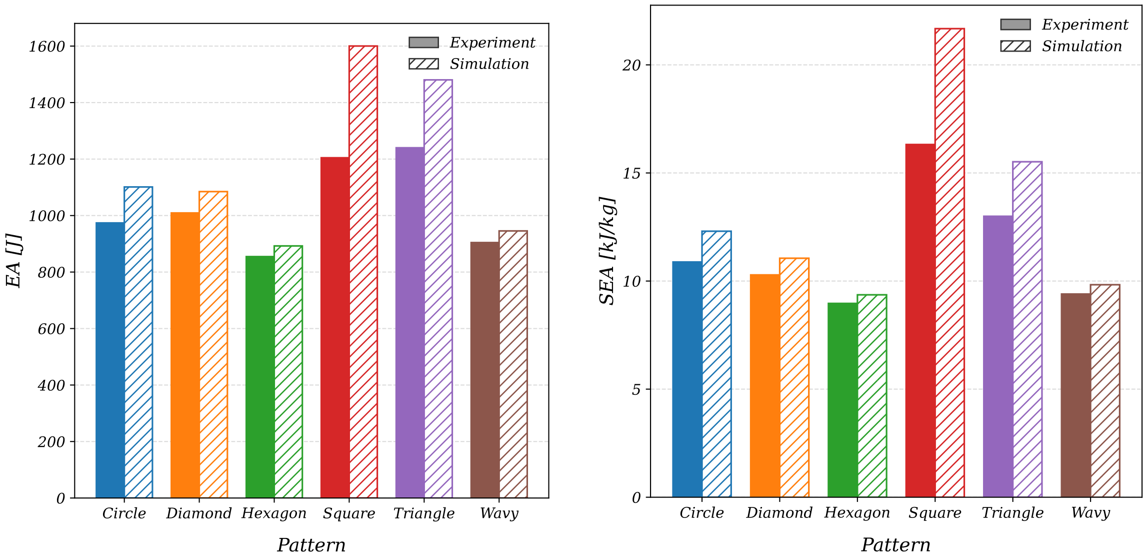

(**a**) Energy Absorption (EA)

(**b**) Specific Energy Absorption (SEA)

Figure 4.15: Comparison between experimental and simulated Energy Absorption (EA) and Specific Energy Absorption (SEA) for all lattice patterns.

After all the experimental and simulated EA / SEA data is outlined for each specimen, a comparative performance study between each pattern can be achieved. While such comparison was already made both for the experiment and the simulation data in previous sections, the limitation of having different displacement values for each pattern made it difficult to establish a definitive performance ordering of the lattices (especially because of the early failure of the Hexagon LS simulation). To achieve that goal, all the data was then truncated at 13.25 mm displacement (to match the Hexagon lattice displacement) and Tables 4.6–4.7 show all the values up to this threshold.

| **Pattern** | $d$ [mm] | $\mathrm{EA_{exp}}$ [J] | $\mathrm{EA_{sim}}$ [J] | $\mathrm{D_{\%exp}}$–C [%] | $\mathrm{D_{\%sim}}$–C [%] | $\mathrm{D_{\%}}$ (S–E) [%] |
|---|---|---|---|---|---|---|
| Circle | 13.25 | 736 | 819 | 0.00 | 0.00 | +11.20 |
| Diamond | 13.25 | 784 | 840 | +6.53 | +2.55 | +7.05 |
| Hexagon | 13.25 | 855 | 892 | +16.15 | +9.01 | +4.37 |
| Square | 13.25 | 956 | 1260 | +29.91 | +53.92 | +31.77 |
| Triangle | 13.25 | 929 | 1110 | +26.18 | +35.54 | +19.44 |
| Wavy | 13.25 | 698 | 725 | -5.22 | -11.38 | +3.93 |

Table 4.6: Comparison between experimental and simulated **Energy Absorption (EA)**, truncated at $d$ = 13.25 mm. Columns include experimental EA ($\mathrm{EA_{exp}}$), simulated EA ($\mathrm{EA_{sim}}$), experimental deviation from Circle ($\mathrm{D_{\%exp}}$–C), simulated deviation from Circle ($\mathrm{D_{\%sim}}$–C), and the simulation relative error ($\mathrm{D_{\%}}$ (S–E)).

| **Pattern** | $d$ [mm] | $\mathrm{SEA_{exp}}$ [kJ/kg] | $\mathrm{SEA_{sim}}$ [kJ/kg] | $\mathrm{D_{\%exp}}$–C [%] | $\mathrm{D_{\%sim}}$–C [%] | $\mathrm{D_{\%}}$ (S–E) [%] |
|---|---|---|---|---|---|---|
| Circle | 13.25 | 8.23 | 9.15 | 0.00 | 0.00 | +11.20 |
| Diamond | 13.25 | 7.99 | 8.56 | -2.92 | -6.44 | +7.16 |
| Hexagon | 13.25 | 8.97 | 9.36 | +8.95 | +2.32 | +4.35 |
| Square | 13.25 | 12.95 | 17.07 | +57.33 | +86.67 | +31.87 |
| Triangle | 13.25 | 9.74 | 11.63 | +18.29 | +27.16 | +19.48 |
| Wavy | 13.25 | 7.26 | 7.54 | -11.80 | -17.55 | +3.85 |

Table 4.7: Comparison between experimental and simulated **Specific Energy Absorption (SEA)**, truncated at $d$ = 13.25 mm. Columns include experimental SEA ($\mathrm{SEA_{exp}}$), simulated SEA ($\mathrm{SEA_{sim}}$), experimental deviation from Circle ($\mathrm{D_{\%exp}}$–C), simulated deviation from Circle ($\mathrm{D_{\%sim}}$–C), and the simulation relative error ($\mathrm{D_{\%}}$ (S–E)).

From Tables 4.6–4.7, it’s possible to make a fair assessment of the LS performance, especially in terms of the placement of the Hexagon LS. In considering EA, the order was Square, Triangle, Hexagon, Diamond, Circle, Wavy for the experimental data and Square, Triangle, Hexagon, Diamond–Circle, Wavy for the simulated data. By comparing the two lists, it’s clear then that the simulation accurately predicted the comparative analysis in terms of energy absorption between the samples, even if it overpredicted the EA for the Square and Triangle lattices by a considerable margin. one difference is that the Diamond and Circle patterns performed very similarly in the simulation case (hence why they were grouped together in the list), whereas the experimental data showed more of a “stepped" ranking, with every LS in its place.

In terms of SEA, the order was Square, Triangle, Hexagon, Circle–Diamond, Wavy for the experimental data – i.e., the higher density of the Diamond lattice in comparison to the Circle lattice made them switch placements – and Square, Triangle, Hexagon–Circle, Diamond, Wavy for the simulated data. In the specific energy case, then, an equivalence was found between the Diamond and Circle patterns for the experiment and between the Hexagon and Circle patterns for the simulation.

All in all, some conclusions can be drawn from the study in terms of comparative energy absorption performance. The first one has to do with the boundaries, i.e., the best and worst performers. In that regard, the Square lattice was consistently the best performer both for experimental and simulated data and for EA / SEA. For SEA specifically, the Square lattice showed an even higher difference from the other patterns and demonstrated an optimal energy absorption capacity per material kg. The second place in the list, the Triangle LS is also consistent among all the observed data and can be confidently placed where it's at. On the other hand, the lowest performer (both for EA and SEA) across all observed data was the Wavy lattice, which can be placed last in the list. For the other three patterns – i.e., Circle, Diamond and Hexagon – they presented similar performance experimentally as well as numerically for most cases, with the Hexagon pattern consistently presenting slightly higher values for EA and SEA in all analyses and the Circle presenting slightly lower values of EA and slightly higher values of SEA in comparison to the Triangle. Figure 4.16 shows a plot comparison of the EA and SEA for all the patterns, while truncating the data at $d$ = 13.25 mm.

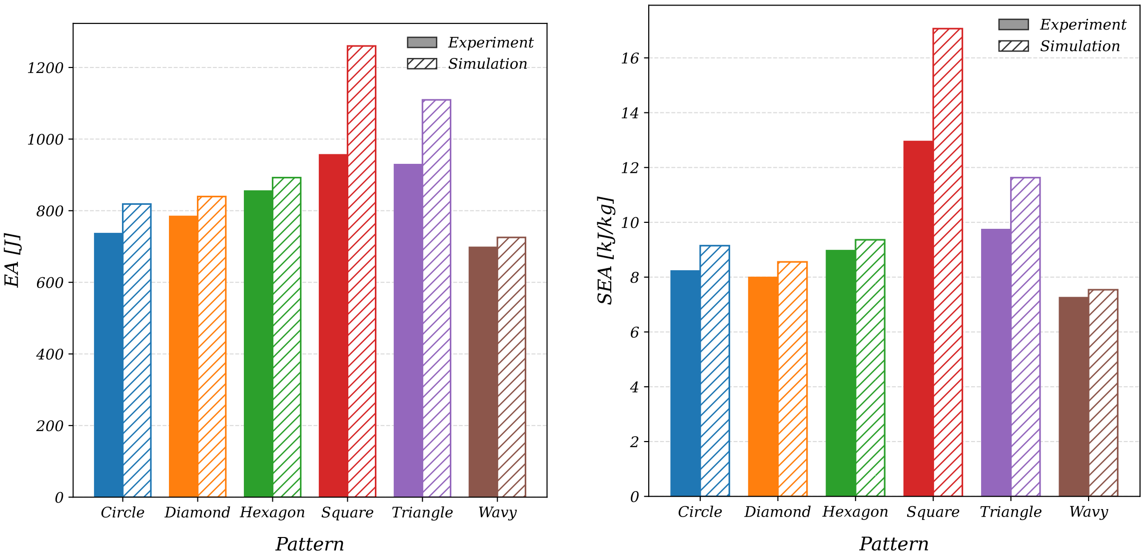

(**a**) Energy Absorption (EA)

(**b**) Specific Energy Absorption (SEA)

Figure 4.16: Comparison between experimental and simulated **Energy Absorption (EA)** and **Specific Energy Absorption (SEA)** using truncated curves ($d \leq 13.25$ mm).

### 4.3.3 Qualitative comparison of deformation modes

Another key aspect in simulating LS is to compare the FEM deformation modes with the experimental ones. Figures 4.17–4.22 show a side-by-side comparison between the FEM and real-life results for each geometry, where pictures of the in-progress experiment are presented to more closely match the simulation's end time. The FEM results display the contour plots for equivalent plastic strain (PEEQ), since it's the key metric in an elastoplastic simulation to determine the higher levels of distortions within a structure.

The Circle pattern (Figure 4.17) showed agreement for the top and bottom unit cells as the structure was crushed. The discrepancy appeared in the middle, where the side struts bent outwards in the simulation, whereas some bent inwards experimentally (producing the already discussed shear band). The simulated Diamond pattern produced the crushed geometry which most closely resembled the experimental one: the bottom struts buckling outwards, some inner struts bending, the larger side-struts not deforming much up to the point of analysis, and the mid section collapsing (see Figure 4.18). The high matching can almost certainly be attributed to the experimental specimens not presenting a global buckling tendency.

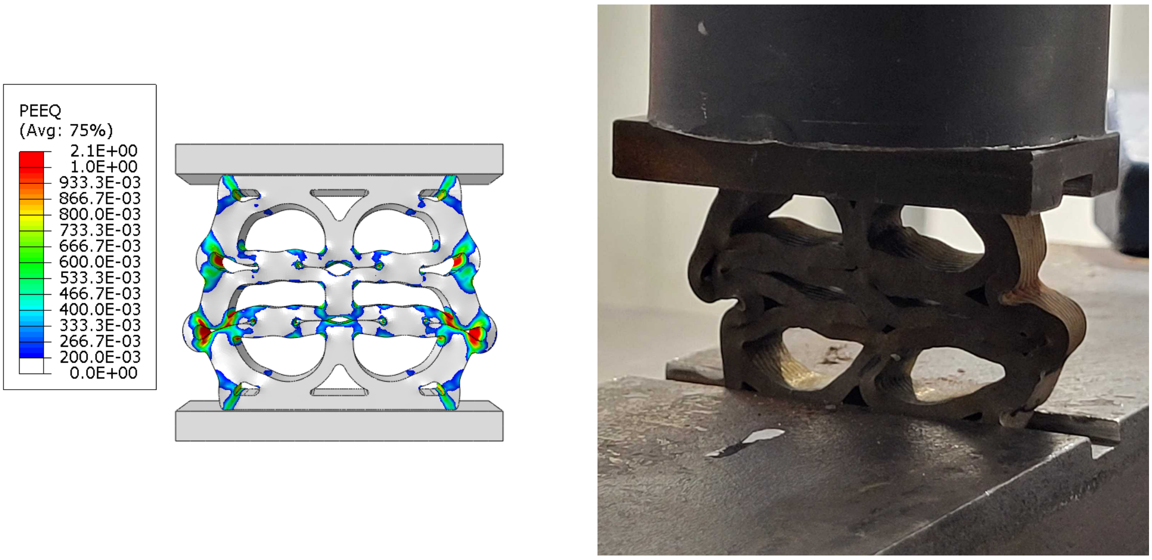

(**a**) FEM Equivalent plastic strain (PEEQ).

(**b**) Experimental deformation mode. Provided by INEGI.

Figure 4.17: Comparison between FEM and experimental results for the Circle pattern.

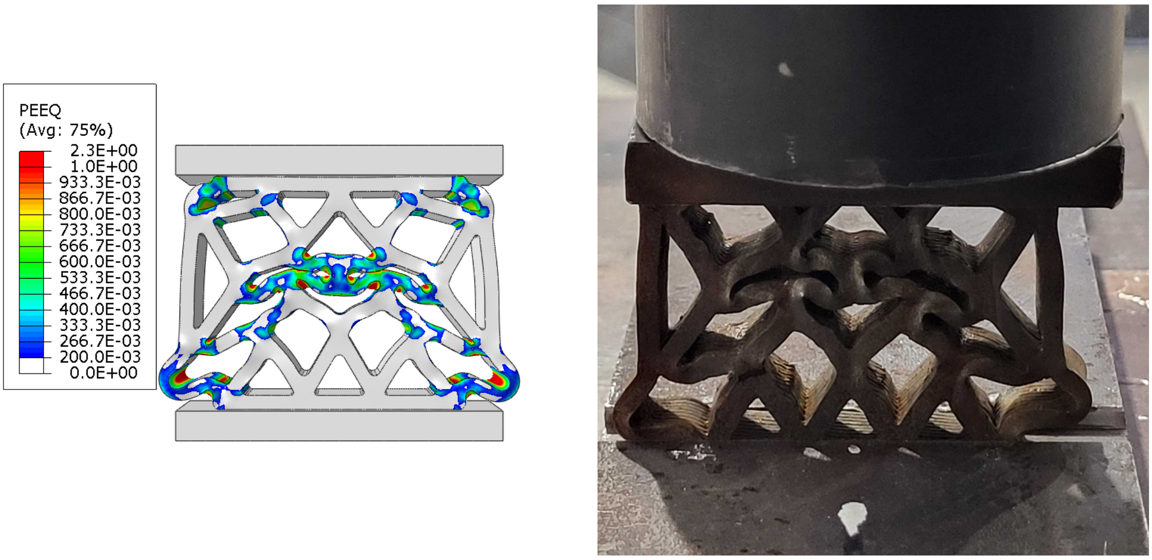

(**a**) FEM Equivalent plastic strain (PEEQ).

(**b**) Experimental deformation mode. Provided by INEGI.

Figure 4.18: Comparison between FEM and experimental results for the Diamond pattern.

The Hexagon pattern LS simulation also showed a good matching with the experimental shape (Figure 4.19), with the mid section collapsing, the outer struts buckling outwards in a symmetric shape. A similar behavior appears in the Wavy pattern (Figure 4.20), where the mid section collapses – but in this case unevenly. A shear band appears in the simulated shape, and it can be faintly seen in the experimental one. Discrepancies come once again in the struts buckling direction: in the simulated shape, all of them buckled outwards and in the experimental some show signs of buckling inwards.

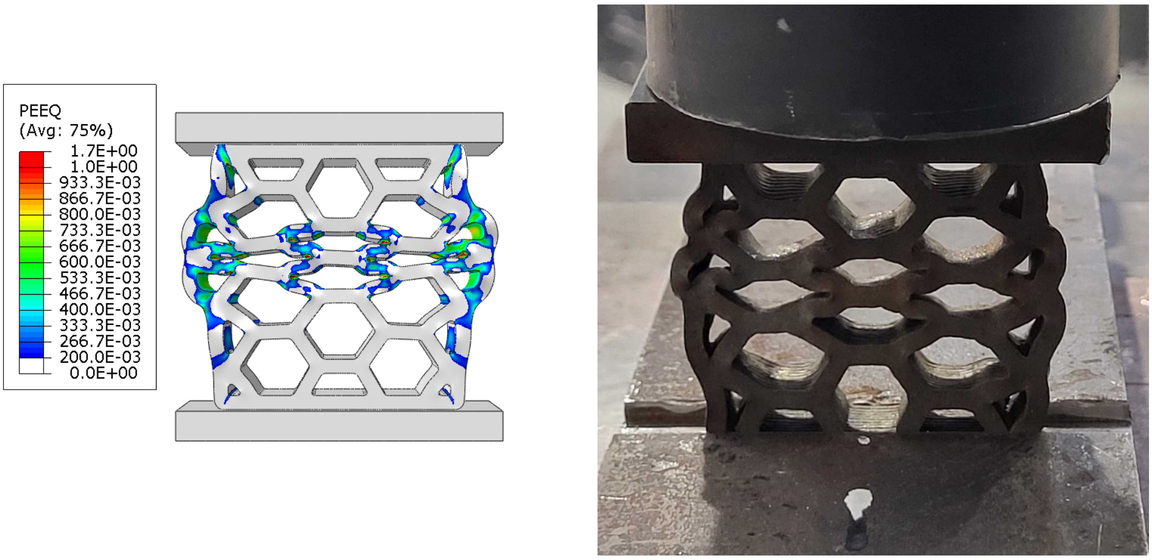

(**a**) FEM  Equivalent plastic strain (PEEQ).

(**b**) Experimental deformation mode. Provided by INEGI.

Figure 4.19: Comparison between FEM and experimental results for the Hexagon pattern.

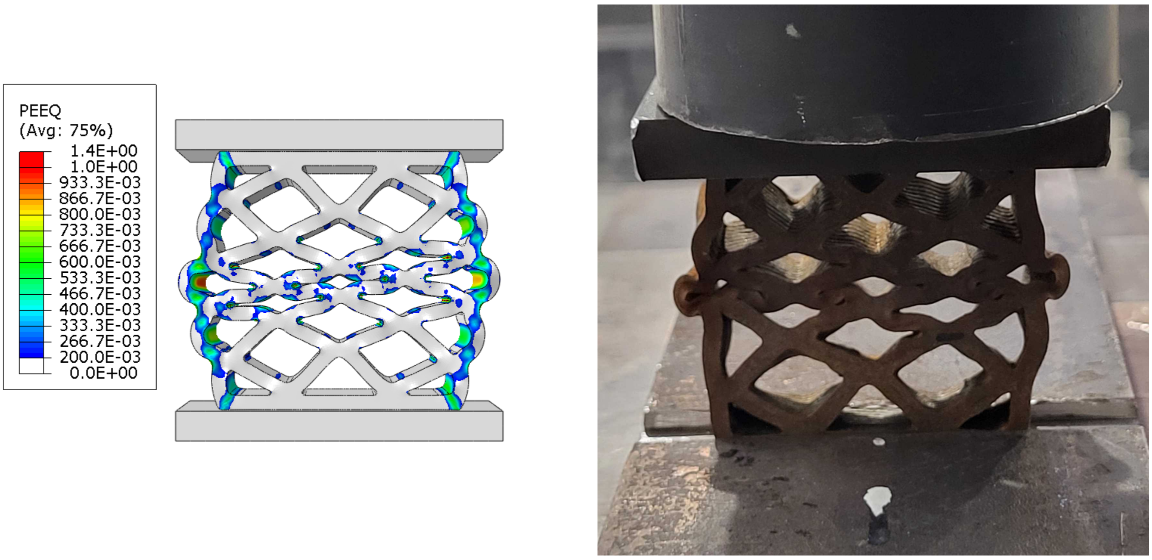

(**a**) FEM  Equivalent plastic strain (PEEQ).

(**b**) Experimental deformation mode. Provided by INEGI.

Figure 4.20: Comparison between FEM and experimental results for the Wavy pattern.

The two simulated LS which showed the least agreement were the Square and the Triangle pattern lattices. As previously mentioned, the Square lattice presented an early global buckling behavior which the simulation didn't capture – affecting both the force–displacement response and the deformed shape. However, agreement is still slightly observed since the simulation highlighted how the shear bands affect this geometry (Figure 4.21**a**), and the formation of a shear band at the same spot (second cell layer) begins to show as the structure buckles (Figure 4.21**b**). The lack of similarity for the Triangle lattice comes from the experimental deformation being concentrated at the largest left mid strut, and in the simulation the load was carried by the smallest struts buckling outwardly (Figure 4.22). Another discrepancy can be seen in terms of the inner struts behavior, where the simulated shape showed most of them bending and the experimental one shows them uniformly buckling. Agreement was obtained for the bottom-left strut, which presented outwards buckling in both the simulation and experiment.

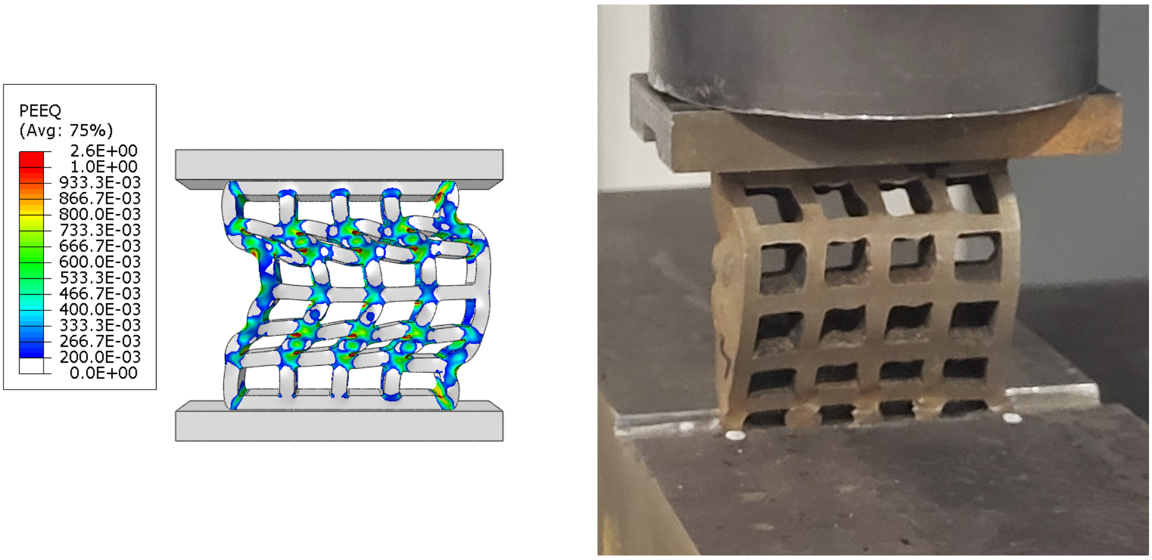

(**a**) FEM Equivalent plastic strain (PEEQ).

(**b**) Experimental deformation mode. Provided by INEGI.

Figure 4.21: Comparison between FEM and experimental results for the Square pattern.

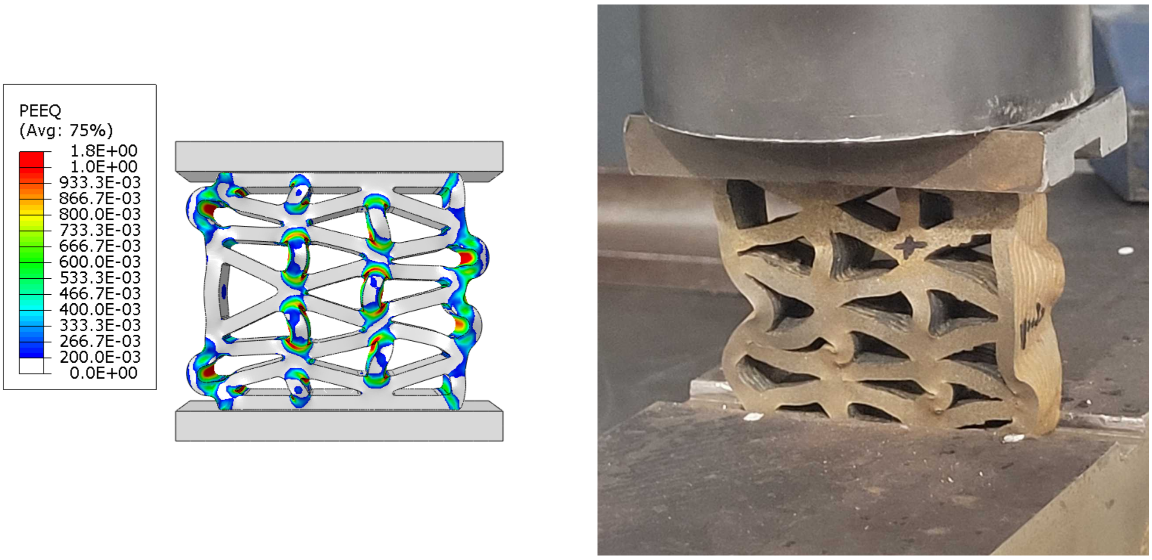

(**a**) FEM Equivalent plastic strain (PEEQ).

(**b**) Experimental deformation mode. Provided by INEGI.

Figure 4.22: Comparison between FEM and experimental results for the Triangle pattern.

# Chapter 5

# CONCLUSION

## 5.1 Summary of Main Findings

This study led to several important findings regarding the modeling and experimental behavior of WLAM-fabricated lattice structures. A calibrated material curve was obtained by applying an optimization algorithm to the Kleinnerman–Ponthot model, resulting in a parameter set that accurately described the material's behavior. When implemented in Abaqus/CAE, the model produced tensile test simulations that closely matched the experimental force–displacement response, demonstrating strong Simulation–Experiment (S–E) agreement.

The finite element modeling approachbased on 3D simulations using Hex–20 elements and 2D rigid guides–proved effective in predicting the compressive response of most lattice structures (LS). Notable exceptions included the Triangle lattice, which retained its shape but exhibited a positional offset, and the Square lattice, where global buckling effects were not captured by the model. Despite these discrepancies, the numerical results for energy absorption (EA) and specific energy absorption (SEA) reproduced experimental trends and maintained the relative performance ranking across all geometries. On average, the S–E energy deviation across all LS was approximately ≈ 13.6%, but this dropped to ≈ 7.3% when the Square and Triangle latticesresponsible for the largest errorswere excluded. These two lattices consistently achieved the highest energy absorption values, whereas the Wavy lattice showed the lowest performance.

In terms of deformation mechanisms, the simulations closely mirrored the experimental observations. The model accurately captured key behaviors such as local buckling, bending, and the early formation of shear bands. Among all configurations, the Diamond lattice showed the best match in deformation behavior, likely due to the absence of global buckling in the physical tests. Strong agreement was also observed for the Hexagon and Wavy lattices, and good agreement for the Circle. Although the Square and Triangle lattices showed greater discrepancies, the simulations were still able to reproduce critical in-test behaviors, including shear-band initiation in the Square lattice and localized strut buckling in the Triangle.

Overall, the finite element framework adopted in this work demonstrated solid predictive capability for WLAM-manufactured 2D lattices. It effectively reproduced both the mechanical response and the deformation patterns observed experimentally, making it a reliable tool for comparative performance analysis across different lattice configurations.

## 5.2 Limitations of the Study

Despite the strong agreement achieved for several lattice structure (LS) patterns and across all analyzed parameters, certain limitations prevented the study from reaching an even higher correlation between experimental and numerical results. One of the main issues was observed in the Hexagon lattice, which exhibited early numerical divergence near the onset of densification. This behavior is attributed to the increasing complexity of contact interactions during the densification phase and underscores the limitations of solving the problem using an implicit approach.

Additionally, several real-world features of the printed specimens were not included in the simulations. These include variations in strut thickness, anisotropy caused by uneven thermal distribution during manufacturing, and the absence of a damage formulation. Each of these factors likely influenced the force–displacement response and contributed to discrepancies in Simulation–Experiment (S–E) matching.

Another important limitation lies in the idealized nature of the finite element model itself. The geometry, boundary conditions, and discretization were simplified, and the 2D LS designs were highly symmetric with respect to the three main mid-planes. This led to highly symmetric deformation patterns in the simulations, which deviated from the more irregular behavior observed in the experimental tests.

As a consequence of this symmetry and the absence of imperfection modeling, the numerical simulations did not reproduce the global buckling behavior exhibited by many of the experimental samplesmost notably the early buckling observed in the Square lattice. These limitations highlight areas where the modeling framework could be refined in future work to improve predictive accuracy.

## 5.3 Suggestions for Future Work

Future research directions emerging from the present investigation include several promising avenues for improving the predictive accuracy and scope of the numerical model. One key direction is the development of a finite element analysis focused on capturing buckling behavior in the lattice structures (LS), potentially through the implementation of a buckling analysis approach, coupled with a Nonlinear study which tried to replicate the buckling tendency. Incorporating a damage formulation into the material model is also recommended, as this would allow investigation into its influence on the force–displacement response and post-yield behavior.

Another valuable extension involves accounting for material anisotropy induced by the non-uniform thermal history during the WLAM process. Introducing an anisotropic material formulation would help better reflect the physical properties of the printed structures. Adding porosity considerations might also help in achieving higher accuracy for the prediction of specimen stiffness. Additionally, mechanical specimens – including both tensile and lattice samples – could be extracted from taller printed blocks to assess how build height and extraction location influence the mechanical response.

Further experimental characterization of WLAM-fabricated components is also encouraged, particularly through compression, shear, and impact tests, in order to develop a more complete understanding of the materials behavior under diverse loading conditions. The impact of the loading speed on the mechanical behavior of the components was also not taken into consideration, so that an investigation on that front would prove both useful and relevant. Finally, a dynamic finite element analysis should be conducted to evaluate the performance of different LS geometries under impact loading, thereby extending the applicability of the model to high-strain-rate scenarios relevant to real-world engineering applications.

# Bibliography

Abuabiah, M., Mbodj, N. G., Shaqour, B., Herzallah, L., Juaidi, A., Abdallah, R., and Plapper, P. (2023). Advancements in Laser Wire-Feed Metal Additive Manufacturing: A Brief Review. *Materials*, 16(5):2030.

Ai, L. and Gao, X.-L. (2017). Metamaterials with negative Poissons ratio and non-positive thermal expansion. *Composite Structures*, 162:70–84.

Al-Saedi, D. S., Masood, S., Faizan-Ur-Rab, M., Alomarah, A., and Ponnusamy, P. (2018). Mechanical properties and energy absorption capability of functionally graded F2BCC lattice fabricated by SLM. *Materials & Design*, 144:32–44.

Alhembar, A., Sheikh-Ahmad, J., Jarrar, F., and Bojanampati, S. (2023). Optimizing the specific mechanical properties of lattice structures fabricated by material extrusion additive manufacturing. *Journal of Materials Research and Technology*, 22:1821–1838.

Alomar, Z. and Concli, F. (2021). Compressive behavior assessment of a newly developed circular cell-based lattice structure. *Materials & Design*, 205:109716.

Ashby, M. (2006). The properties of foams and lattices. *Philosophical Transactions of the Royal Society A: Mathematical, Physical and Engineering Sciences*, 364(1838):15–30.

ASTM (2012). Terminology for Additive Manufacturing Technologies,.

ASTM (2024). Standard test methods for tension testing of metallic materials.

Bajaj, P., Hariharan, A., Kini, A., Kürnsteiner, P., Raabe, D., and Jägle, E. (2020). Steels in additive manufacturing: A review of their microstructure and properties. *Materials Science and Engineering: A*, 772:138633.

Bedoya, M. C., Restrepo, J. W., Wilches, L. V., and Rodriguez, J. (2025). Cellular Structures Analysis Under Compression Test. *Polymers*, 17(11):1476.

Bhate, D. (2019). Four Questions in Cellular Material Design. *Materials*, 12(7):1060.

Chen, L.-Y., Liang, S.-X., Liu, Y., and Zhang, L.-C. (2021). Additive manufacturing of metallic lattice structures: Unconstrained design, accurate fabrication, fascinated performances, and challenges. *Materials Science and Engineering: R: Reports*, 146:100648.

Clarke, D. J., Imediegwu, C., Moat, R., and Jowers, I. (2023). A systematic numerical and experimental study into the mechanical properties of five honeycombs. *Composites Part B: Engineering*, 264:110895.

Da Silva, C. P., Silva, G. P., Santos, M. C., Ziberov, M., and Malcher, L. (2024). Hybrid search methodology for mechanical characterization of material produced via WAAM assuming Gurson porous material. *Journal of the Brazilian Society of Mechanical Sciences and Engineering*, 46(5):266.

DebRoy, T., Wei, H., Zuback, J., Mukherjee, T., Elmer, J., Milewski, J., Beese, A., Wilson-Heid, A., De, A., and Zhang, W. (2018). Additive manufacturing of metallic components Process, structure and properties. *Progress in Materials Science*, 92:112–224.

Du, Y., Gu, D., Xi, L., Dai, D., Gao, T., Zhu, J., and Ma, C. (2020). Laser additive manufacturing of bio-inspired lattice structure: Forming quality, microstructure and energy absorption behavior. *Materials Science and Engineering: A*, 773:138857.

Feng, G.-z., Wang, J., Li, X.-y., Xiao, L.-j., and Song, W.-d. (2022). Mechanical behavior of Ti6Al4V lattice-walled tubes under uniaxial compression. *Defence Technology*, 18(7):1124–1138.

Förster, W., Pucklitzsch, T., Dietrich, D., and Nickel, D. (2022). Mechanical performance of hexagonal close-packed hollow sphere infill structures with shared walls under compression load. *Additive Manufacturing*, 59:103135.

Garg, A., Sharma, A., Zheng, W., and Li, L. (2025). A review on artificial intelligence-enabled mechanical analysis of 3D printed and FEM-modelled auxetic metamaterials. *Virtual and Physical Prototyping*, 20(1):e2445712.

Ghaemi Khiavi, S., Mohammad Sadeghi, B., and Divandari, M. (2022). Effect of topology on strength and energy absorption of PA12 non-auxetic strut-based lattice structures. *Journal of Materials Research and Technology*, 21:1595–1613.

Ghanadi, N. and Pasebani, S. (2024). A Review on Wire-Laser Directed Energy Deposition: Parameter Control, Process Stability, and Future Research Paths. *Journal of Manufacturing and Materials Processing*, 8(2):84.

Ghidini, T., Grasso, M., Gumpinger, J., Makaya, A., and Colosimo, B. (2023). Additive manufacturing in the new space economy: Current achievements and future perspectives. *Progress in Aerospace Sciences*, 142:100959.

Gibson, L. J. (2003). Cellular Solids. *MRS Bulletin*, 28(4):270–274.

Gomez-Lendinez, D., Garcia-Moreno-Caraballo, J., Corbera, S., and Barea, R. (2025). Influence of Laser-Wire Metal Deposition Process Parameters on the Mechanical Properties and Microstructure of ER70S-6 Steel.

Ha, N. S., Pham, T. M., Tran, T. T., Hao, H., and Lu, G. (2022). Mechanical properties and energy absorption of bio-inspired hierarchical circular honeycomb. *Composites Part B: Engineering*, 236:109818.

Ingrole, A., Hao, A., and Liang, R. (2017). Design and modeling of auxetic and hybrid honeycomb structures for in-plane property enhancement. *Materials & Design*, 117:72–83.

Kleinermann, J.-P. and Ponthot, J.-P. (2003). Parameter identification and shape/process optimization in metal forming simulation. *Journal of Materials Processing Technology*, 139(1-3):521–526.

Lakes, R. (1987). Foam Structures with a Negative Poisson's Ratio. *Science*, 235(4792):1038–1040.

Leary, M., Mazur, M., Williams, H., Yang, E., Alghamdi, A., Lozanovski, B., Zhang, X., Shidid, D., Farahbod-Sternahl, L., Witt, G., Kelbassa, I., Choong, P., Qian, M., and Brandt, M. (2018). Inconel 625 lattice structures manufactured by selective laser melting (SLM): Mechanical properties, deformation and failure modes. *Materials & Design*, 157:179–199.

Li, T., Sun, J., Leng, J., and Liu, Y. (2023). Quasi-static compressive behavior and energy absorption of novel cellular structures with varying cross-section dimension. *Composite Structures*, 306:116582.

Maconachie, T., Leary, M., Lozanovski, B., Zhang, X., Qian, M., Faruque, O., and Brandt, M. (2019). SLM lattice structures: Properties, performance, applications and challenges. *Materials & Design*, 183:108137.

Maskery, I., Aboulkhair, N., Aremu, A., Tuck, C., Ashcroft, I., Wildman, R., and Hague, R. (2016). A mechanical property evaluation of graded density Al-Si10-Mg lattice structures manufactured by selective laser melting. *Materials Science and Engineering: A*, 670:264–274.

Meltio (2021). 3d printed metal engine manifold for motorsport - meltio engine robot integration. `https://www.youtube.com/watch?v=6BvGbGKGQhI`. YouTube video.

Mohammadi, H., Ahmad, Z., Petr, M., Mazlan, S. A., Faizal Johari, M. A., Hatami, H., and Rahimian Koloor, S. S. (2023). An insight from nature: honeycomb pattern in advanced structural design for impact energy absorption. *Journal of Materials Research and Technology*, 22:2862–2887.

Montgomery-Liljeroth, E., Schievano, S., and Burriesci, G. (2023). Elastic properties of 2D auxetic honeycomb structures- a review. *Applied Materials Today*, 30:101722.

Nazir, A., Abate, K. M., Kumar, A., and Jeng, J.-Y. (2019). A state-of-the-art review on types, design, optimization, and additive manufacturing of cellular structures. *The International Journal of Advanced Manufacturing Technology*, 104(9-12):3489–3510.

Nazir, A., Gokcekaya, O., Md Masum Billah, K., Ertugrul, O., Jiang, J., Sun, J., and Hussain, S. (2023). Multi-material additive manufacturing: A systematic review of design, properties, applications, challenges, and 3D printing of materials and cellular metamaterials. *Materials & Design*, 226:111661.

Pan, C., Han, Y., and Lu, J. (2020). Design and Optimization of Lattice Structures: A Review. *Applied Sciences*, 10(18):6374.

Pratheesh Kumar S, Anand K, Hari Chealvan S, and Karthikeya Muthu S (2022). Review on surface characteristics of components produced by direct metal deposition process. *Journal of Mechanical Engineering and Sciences*, pages 9197–9229.

Qi, C., Jiang, F., and Yang, S. (2021). Advanced honeycomb designs for improving mechanical properties: A review. *Composites Part B: Engineering*, 227:109393.

Reda, H., Karathanasopoulos, N., Elnady, K., Ganghoffer, J. F., and Lakiss, H. (2018). Mechanics of Metamaterials: An Overview of Recent Developments. In dell'Isola, F., Eremeyev, V. A., and Porubov, A., editors, *Advances in Mechanics of Microstructured Media and Structures*, volume 87, pages 273–296. Springer International Publishing, Cham. Series Title: Advanced Structured Materials.

Saxena, K. K., Das, R., and Calius, E. P. (2016). Three Decades of Auxetics Research Materials with Negative Poisson's Ratio: A Review. *Advanced Engineering Materials*, 18(11):1847–1870.

Shaikh, M. O., Chen, C.-C., Chiang, H.-C., Chen, J.-R., Chou, Y.-C., Kuo, T.-Y., Ameyama, K., and Chuang, C.-H. (2020). Additive manufacturing using fine wire-based laser metal deposition. *Rapid Prototyping Journal*, 26(3):473–483.

Sharma, D. and Hiremath, S. S. (2023). Experimental and FEM study on the in-plane and out-plane loaded reversible dual-material bio-inspired lattice structures with improved energy absorption performance. *Composite Structures*, 303:116353.

Silva, C. P. d. (2024). Implementação de método híbrido para determinação de parâmetros de encruamento.

Sun, Q., Sun, J., Guo, K., and Wang, L. (2022). Compressive mechanical properties and energy absorption characteristics of SLM fabricated Ti6Al4V triply periodic minimal surface cellular structures. *Mechanics of Materials*, 166:104241.

Sychov, M., Lebedev, L., Dyachenko, S., and Nefedova, L. (2018). Mechanical properties of energy-absorbing structures with triply periodic minimal surface topology. *Acta Astronautica*, 150:81–84.

Tao, W. and Leu, M. C. (2016). Design of lattice structure for additive manufacturing. In *2016 International Symposium on Flexible Automation (ISFA)*, pages 325–332, Cleveland, OH, USA. IEEE.

Theocaris, P. S., Stavroulakis, G. E., and Panagiotopoulos, P. D. (1997). Negative Poisson's ratios in composites with star-shaped inclusions: a numerical homogenization approach. *Archive of Applied Mechanics (Ingenieur Archiv)*, 67(4):274–286.

Wang, Y., Ren, X., Chen, Z., Jiang, Y., Cao, X., Fang, S., Zhao, T., Li, Y., and Fang, D. (2020). Numerical and experimental studies on compressive behavior of Gyroid lattice cylindrical shells. *Materials & Design*, 186:108340.

Wu, Y., Fang, J., Wu, C., Li, C., Sun, G., and Li, Q. (2023). Additively manufactured materials and structures: A state-of-the-art review on their mechanical characteristics and energy absorption. *International Journal of Mechanical Sciences*, 246:108102.

Xiao, L., Song, W., Wang, C., Tang, H., Fan, Q., Liu, N., and Wang, J. (2017). Mechanical properties of open-cell rhombic dodecahedron titanium alloy lattice structure manufactured using electron beam melting under dynamic loading. *International Journal of Impact Engineering*, 100:75–89.

Yin, H., Zhang, W., Zhu, L., Meng, F., Liu, J., and Wen, G. (2023). Review on lattice structures for energy absorption properties. *Composite Structures*, 304:116397.

Yin, Y., Tan, Q., Bermingham, M., Mo, N., Zhang, J., and Zhang, M.-X. (2022). Laser additive manufacturing of steels. *International Materials Reviews*, 67(5):487–573.

Zeng, C., Liu, L., Bian, W., Leng, J., and Liu, Y. (2021). Compression behavior and energy absorption of 3D printed continuous fiber reinforced composite honeycomb structures with shape memory effects. *Additive Manufacturing*, 38:101842.

Zhang, C., Zheng, H., Yang, L., Li, Y., Jin, J., Cao, W., Yan, C., and Shi, Y. (2022). Mechanical responses of sheet-based gyroid-type triply periodic minimal surface lattice structures fabricated using selective laser melting. *Materials & Design*, 214:110407.

Zhang, J. and Lu, G. (2023). Energy absorption of re-entrant honeycombs in tension and compression. *Engineering Structures*, 288:116237.

Zhang, X., Leary, M., Tang, H., Song, T., and Qian, M. (2018). Selective electron beam manufactured Ti-6Al-4V lattice structures for orthopedic implant applications: Current status and outstanding challenges. *Current Opinion in Solid State and Materials Science*, 22(3):75–99.

Zhou, J., Liu, H., Dear, J. P., Falzon, B. G., and Kazanc, Z. (2023). Comparison of different quasi-static loading conditions of additively manufactured composite hexagonal and auxetic cellular structures. *International Journal of Mechanical Sciences*, 244:108054.